

EBS Task-Force Modelling Report: Modelling AECL's Tests – Isothermal Test and Buffer/Container Experiment

NWMO TR-2007-13

December 2007

Ruiping Guo

Atomic Energy of Canada Limited

nwmo

NUCLEAR WASTE
MANAGEMENT
ORGANIZATION

SOCIÉTÉ DE GESTION
DES DÉCHETS
NUCLÉAIRES



Nuclear Waste Management Organization
22 St. Clair Avenue East, 6th Floor
Toronto, Ontario
M4T 2S3
Canada

Tel: 416-934-9814
Web: www.nwmo.ca

**EBS Task-Force Modelling Report: Modelling AECL's Tests – Isothermal Test and
Buffer/Container Experiment**

NWMO TR-2007-13

December 2007

R. Guo
Atomic Energy of Canada Limited

Disclaimer:

This report does not necessarily reflect the views or position of the Nuclear Waste Management Organization, its directors, officers, employees and agents (the "NWMO") and unless otherwise specifically stated, is made available to the public by the NWMO for information only. The contents of this report reflect the views of the author(s) who are solely responsible for the text and its conclusions as well as the accuracy of any data used in its creation. The NWMO does not make any warranty, express or implied, or assume any legal liability or responsibility for the accuracy, completeness, or usefulness of any information disclosed, or represent that the use of any information would not infringe privately owned rights. Any reference to a specific commercial product, process or service by trade name, trademark, manufacturer, or otherwise, does not constitute or imply its endorsement, recommendation, or preference by NWMO.

ABSTRACT

Title: EBS Task-Force Modelling Report: Modelling AECL's Tests - Isothermal Test and Buffer/Container Experiment
Report No.: NWMO TR-2007-13
Author(s): R. Guo
Company: Atomic Energy of Canada Limited
Date: December 2007

Abstract

In order to investigate how heat affects the performance of a dense bentonite-sand buffer, two full-scale in-situ experiments, the Isothermal Test (ITT) and the Buffer/Container Experiment, were conducted by Atomic Energy of Canada Limited (AECL). In the Buffer/Container Experiment, there was a full-size electric heater simulating the heat output of a disposal container of used fuel installed vertically in a 1.24-m-diameter by 5-m-deep borehole surrounded by a clay-based buffer. The borehole was drilled in the floor of a room excavated in Canadian Shield granite on the 240 Level of AECL's Underground Research Laboratory (URL). The thermal, hydraulic and mechanical response was monitored in the buffer and in the surrounding rock. Power was provided to the heater for approximately 896 days. The Isothermal Test was installed in an identical borehole also drilled in Canadian Shield granite on the 240 Level of AECL's URL to investigate the hydraulic interaction between the buffer and rock without influence of thermal gradient. The bottom two metres of the Isothermal Test borehole was filled with an in situ compacted buffer material. This material was capped by a 1.25-m-thick plug of high-performance concrete and was monitored for 6.5 years.

The Nuclear Waste Management Organization (NWMO) sponsors AECL's participation in the Engineering Barrier System Task Force (EBS TF) modelling group. The information about ITT and the Buffer/Container Experiment is shared by the EBS TF numerical modelling group for use in evaluating the effectiveness of several mathematical models in predicting the evolution of the coupled processes in unsaturated clay-based material. This report is part of NWMO's AECL's input of modelling results to the EBS TF.

Numerical simulations were conducted using CODE_BRIGHT to model the evolution of the pore pressure in the unsaturated bentonite-sand buffer and the surrounding rock as well as mechanical response of the buffer during the 6.5 years of water uptake for the ITT and the evolution of the temperature, thermally induced pore water pressure and mechanical response in the buffer and the surrounding rock for the Buffer/Container Experiment.

The influence of the excavation-induced damage zone on the evolution of the hydraulic response in the bentonite-sand material and the rock was examined. The simulated water seepage from the rock to the borehole was compared with measured results for both the ITT and the Buffer/Container Experiment. The simulated pore water pressure in the rock and the pore water suction in the buffer were compared with data measured during the test and inferred from end-of-test buffer moisture conditions for both the ITT and the Buffer/Container Experiment. The modelled vertical displacements in the rock are also compared with the measured data in the Buffer/Container Experiment. Based on the comparison of the simulated thermally induced pore water pressure in the rock with measured pore pressure, the possible range of rock permeability, and its dependence on temperature, is discussed. The simulated displacements in the buffer and the stresses in the rock are also presented in this report.

TABLE OF CONTENTS

	<u>Page</u>
ABSTRACT	v
1. INTRODUCTION	1
2. THE ISOTHERMAL TEST	2
2.1 DESCRIPTION OF THE ISOTHERMAL TEST	2
2.1.1 Experiment Set-Up.....	2
2.1.2 Phases Related to the Isothermal Test.....	5
2.1.3 Instrumentation	5
2.2 MODEL GEOMETRY, BOUNDARY CONDITIONS AND INITIAL CONDITIONS	10
2.2.1 Model Geometry	10
2.2.2 Boundary Conditions.....	10
2.2.2.1 Hydraulic Boundary Conditions	10
2.2.2.2 Mechanical Boundary Conditions.....	11
2.2.3 Initial Boundary Conditions	12
2.2.4 Discretization Of The Model.....	12
2.3 MATERIAL PARAMETERS	13
2.3.1 Bentonite-Sand Buffer Material Parameters.....	13
2.3.1.1 Hydraulic Parameters of Materials	13
2.3.1.2 Mechanical Parameters	16
2.3.2 Granite Rock Material Parameters.....	18
2.3.2.1 Hydraulic Parameters	18
2.3.2.2 Mechanical Parameters	18
2.3.3 Concrete Cap Parameters	18
2.4 MODELLED RESULTS AND COMPARISON WITH MEASURED DATA.....	19
2.4.1 Influence of Excavation Damage Zone on the Pore Water Pressure in the Rock before Buffer Installation.....	19
2.4.2 Seepage Prior To The Buffer Placement	20
2.4.3 Pore Water Pressure In The Rock.....	21
2.4.4 Hydraulic Results In The Buffer	25
2.4.5 Mechanical Response In The Buffer	31
2.4.5.1 Earth Pressures at the Interface between the Buffer and the Rock.....	31
2.4.5.2 Simulated Stresses in the Buffer.....	33
2.4.5.3 Simulated Displacements in the Buffer	35
2.5 SUMMARY – ITT MODELLING	38
3. BUFFER/CONTAINER EXPERIMENT	39
3.1 DESCRIPTION OF THE BUFFER/CONTAINER EXPERIMENT	39
3.2 MODEL GEOMETRY, BOUNDARY CONDITIONS AND INITIAL CONDITIONS	51
3.2.1 Model Geometry	51
3.2.2 Boundary Conditions.....	51
3.2.2.1 Thermal Boundary Conditions.....	51

3.2.2.2	Hydraulic Boundary Conditions	51
3.2.2.3	Mechanical Boundary Conditions	52
3.2.3	Initial Conditions	53
3.2.4	Discretization Of The Model	53
3.3	MATERIAL PARAMETERS	53
3.3.1	Bentonite-Sand Buffer Material Parameters.....	54
3.3.1.1	Thermal and Hydraulic Parameters.....	54
3.3.1.2	Mechanical Parameters	55
3.3.2	Granite Material Parameters	55
3.3.2.1	Thermal and Hydraulic Parameters.....	55
3.3.2.2	Mechanical Parameters	55
3.3.3	Backfill Parameters	55
3.3.4	Sand Material Parameters	57
3.4	MODELLING RESULTS AND COMPARISON WITH MEASUREMENTS	58
3.4.1	Thermal Response	58
3.4.1.1	Temperature Changes on the Surface of the Heater	58
3.4.1.2	Thermal Response in the Buffer and the Rock	58
3.4.2	Hydraulic Response.....	67
3.4.2.1	Water Inflow into the Placement Borehole	67
3.4.2.2	Hydraulic Response in the Buffer.....	67
3.4.2.3	Hydraulic Response in the Rock	70
3.4.3	Mechanical Response in the Buffer and the Rock.....	78
3.4.3.1	Mechanical Response in the Buffer.....	78
3.4.3.2	Mechanical Response in the Rock	84
3.5	SUMMARY - BCE MODELLING	87
4.	CONCLUSIONS	88
	ACKNOWLEDGEMENTS	89
	REFERENCES	90

LIST OF TABLES

	<u>Page</u>
Table 1: Depth of Moisture Content Relative to the Top Surface of the Buffer	10
Table 2: Hydraulic Parameters of the Buffer and Granite Rock.....	16
Table 3: Mechanical Parameters of the Buffer and Granite Rock.....	18
Table 4: Measured and Calculated Inflow from the Wall of the Borehole	21
Table 5: Measured and Simulated Water Inflow before Experiment Installation.....	67

LIST OF FIGURES

	<u>Page</u>
Figure 1: General Layout of the URL	2
Figure 2: Plan Illustrating the Geology of the 240 Level and Location of the Isothermal Test (Graham et al. 1997).....	3
Figure 3: Groundwater Pressure (kPa) Contours at the 240 Level of the URL (Graham et al. 1997)	4
Figure 4: Location of Piezometers Surrounding the Isothermal Test (after Chandler 2000)	4
Figure 5: Configuration of the Isothermal Test Seepage Collection System (Chandler 2000) ...	6
Figure 6: Plan View of the Isothermal Test (Dixon et al. 2001).....	6
Figure 7: Cross-section A-A of the Isothermal Test Installation (Dixon et al. 2001).....	7
Figure 8: Cross-sections of Isothermal Test Showing Instrumentation Layers along Sections B-B, C-C and D-D (Dixon et al. 2001)	8
Figure 9: Layout and Numbering System Using Template for Moisture Content Sampling (Dixon et al. 2001).....	9
Figure 10: Dimensions of the Model Geometry and Hydraulic Boundary Conditions.....	11
Figure 11: 2-D Axisymmetric Four-noded Finite Element Mesh	12
Figure 12: Suction - Water Content Relationship for Buffer Materials (Wan et al. 1995; Graham et al. 1997).....	14
Figure 13: Saturation of the Buffer versus Suction.....	15
Figure 14: Hydraulic Conductivity of the Buffer as a Function of Buffer Saturation	16
Figure 15: Pore Water Pressures in the Rock prior to Placing the Buffer.....	19
Figure 16: Pore Water Pressure Contour in the Rock before Placing the Buffer.....	21
Figure 17: Pore Water Pressure Contour in the Rock 1000 Days after Placing the Buffer	22
Figure 18: Pore Water Pressure Contour in the Rock 2400 Days after Placing the Buffer	23
Figure 19: Simulated Pore Water Pressure Contours in the Rock Compared to Measured Data 2400 Days after Placing the Buffer	23
Figure 20: Mid-height Values of Pore Water Pressure in the Rock	24
Figure 21: Pore Water Pressure Evolutions at Locations IRP2, IRP3 and IRP4.....	24
Figure 22: Comparison of the Rock Pore Pressure Computed Using a Hydraulic-Only Model and a Coupled H-M Model.....	25
Figure 23: Suction Predictions at 0.5 m Height from the Bottom of Buffer vs. Distance from the Borehole Centreline for Different Times.....	25
Figure 24: Suction Predictions at Mid-Height of Buffer vs. Distance from the Borehole Centreline for Different Times	26
Figure 25: Suction Predictions at 1.5 m Height from the Bottom of Buffer vs. Distance from the Borehole Centreline for Different Times	26

Figure 26: Transient Pore Water Pressures in the Buffer (from coupled H-M modelling).....	27
Figure 27: Measured End-Of-Test Water Distribution Vertically Through the Buffer (after Dixon and Chandler 2000)	27
Figure 28: Pore Water Pressure Profiles in the Buffer for Layer A.....	28
Figure 29: Pore Water Pressure Profiles in the Buffer for Layer B.....	28
Figure 30: Pore Water Pressure Profiles in the Buffer for Layer C.....	29
Figure 31: Pore Water Pressure Profiles in the Buffer for Layer D.....	29
Figure 32: Pore Water Pressure Profiles in the Buffer for Layer E.....	30
Figure 33: Pore Water Pressure Profiles in the Buffer for Layer F.....	30
Figure 34: Pore Water Pressure Profiles in the Buffer for Layer G.....	31
Figure 35: Pore Water Pressure Profiles in the Buffer for Layer H.....	31
Figure 36: Radial Pressures in the Buffer at Locations of IBG1 and IBG2	32
Figure 37: Vertical Pressures in the Buffer at Locations of IBR1, IBR2 and IBR3	32
Figure 38: Simulated Horizontal Stresses in the Buffer along a Horizontal Section of the Buffer at the Mid-height (negative stress is compressive).....	33
Figure 39: Simulated Vertical Stresses in the Buffer along a Horizontal Section of the Buffer at the Mid-height (negative stress is compressive)	33
Figure 40: Simulated Horizontal Stresses in the Buffer along a Vertical Section of the Buffer 0.39 m from the Centre (negative stress is compressive).....	34
Figure 41: Simulated Vertical Stresses in the Buffer along a Vertical Section of the Buffer 0.39 m from the Centre (negative stress is compressive).....	34
Figure 42: Simulated Horizontal Displacements in the Buffer along a Horizontal Section of the Buffer at the Mid-height (negative values in horizontal displacements means the buffer moved towards the axis of the borehole)	35
Figure 43: Simulated Vertical Displacements in the Buffer along a Horizontal Section of the Buffer at the Mid-height (negative vertical displacement means the buffer moved downwards)	36
Figure 44: Simulated Horizontal Displacements in the Buffer along a Vertical Section of the Buffer 0.39 m from the Centre	37
Figure 45: Simulated Vertical Displacements in the Buffer along a Vertical Section of the Buffer 0.39 m from the Centre.....	37
Figure 46: Measured Density Distribution in the Isothermal Test at the Time of Decommissioning.....	38
Figure 47: Construction Layout and Dimensions of AECL's Buffer/Container Experiment (after Graham et al. 1997)	41
Figure 48: System for Measuring Water Inflow into Placement Borehole before Installation of Buffer (Graham et al. 1997)	42
Figure 49: Section C-C through the Buffer showing Thermocouples (BT, FT), and Earth Pressure Cells (BR) (after Graham et al. 1997)	43
Figure 50: Section AA showing Layout of Thermocouples (BT) and some of the Total Pressure Cells (BR) (Graham et al. 1997).....	44
Figure 51: Installation Geometry for Hydraulic Piezometers (Chandler et al. 1998)	45
Figure 52: Plan of Instrumentation (Graham et al. 1997)	46
Figure 53: Transverse Section of Room 213 showing Rock Strain and Packer Instrumentation.....	46
Figure 54: Longitudinal Section of Room 213 Showing Packer (HG) and Thermistor (T) Instrumentations in the Rock (after Graham et al. 1997).....	47
Figure 55: Section DD showing Psychrometers (BX).....	48
Figure 56: Vertical Section indicating Frequency and Type of Sampling Planned for Decommissioning.....	49
Figure 57: Section BB showing Thermocouples (BT) and Total Pressure Cells (BG, BR).....	50

Figure 58: Dimensions of the Model Geometry and Hydraulic Boundary Conditions	52
Figure 59: 2-D Axisymmetric Four-noded Finite Element Mesh	54
Figure 60: Water Retention Curve for the Backfill used in AECL's Buffer/Container Experiment.....	56
Figure 61: Relationship between the Backfill Hydraulic Conductivity and its Saturation	56
Figure 62: Retention Curve between Suction and Degree of Saturation of Sand Used in this Modelling.....	57
Figure 63: Simulated and Measured Temperatures of the Heater.....	58
Figure 64: Comparison of Simulated and Measured Temperatures in the Buffer at Locations of Instruments 1BT53, 1BT116, 1BT90 and 1BT17	59
Figure 65: Comparison of Simulated and Measured Temperatures in the Rock at Four Locations along the Mid-height of the Buffer	60
Figure 66: Simulated and Measured Transient Temperature Profiles along the Mid-Height of the Heater	61
Figure 67: Simulated and Measured Temperatures through the Placement Borehole Centre...61	
Figure 68: Temperatures at Different Depths from the Top of the Concrete Collar of Borehole T7	62
Figure 69: Temperatures at Different Depths from the Top of the Concrete Collar of Borehole T8	63
Figure 70: Temperature Distributions along Borehole T7 at Four Different Times	64
Figure 71: Temperature Distributions along Borehole T8 at Four Different Times	64
Figure 72: Temperature Contours at Four Different Times of Heating in the Buffer	65
Figure 73: Temperature Contours at Four Different Times of Heating in the Rock.....	66
Figure 74: Pore Water Potential in the Buffer Measured by Thermal Needles and Psychrometers (after Graham et al. 1997) (Note: There were no functioning sensors in the buffer and backfill above the heater)	68
Figure 75: Vertical Section of Water Contents Measured during Decommissioning Aligned with Axis of Room 213 (Graham et al. 1997).....	69
Figure 76: Simulated Transient Pore Water Pressures during Heating in the Buffer.....	69
Figure 77: Comparisons of Simulated and Measured Suctions in the Buffer for IBX01, IBX06 and IBX07.....	70
Figure 78: Comparisons of Simulated and Measured Suctions in the Buffer for IBX12, IBX16 and IBX17.....	70
Figure 79: Measured Pore Water Pressures in a Domain of 4 m x 8 m in the Rock at Four Different Times	71
Figure 80: Simulated Pore Water Pressures during Heating at Four Different Times using $5 \times 10^{-20} \text{ m}^2$ as the Saturated Permeability of the Rock.....	72
Figure 81: Simulated Pore Water Pressures during Heating at Four Different Times using $5 \times 10^{-22} \text{ m}^2$ as the Saturated Permeability of the Rock.....	73
Figure 82: Simulated and Measured Pore Water Pressures at Locations HG9, HG11, HG8, HG10 and HG7 at a Depth of 2.45 m from the Floor of Room 213	74
Figure 83: Simulated and Measured Pore Water Pressures at Locations HG9, HG11, HG8 and HG7 at a Depth of 4.6 m from the Floor of Room 213	74
Figure 84: Simulated and Measured Pore Water Pressure Profiles in the Rock at a Depth of 1.0 m from the Floor of Room 213 (Note: the measured pore water pressure in these intervals remained constant and unchanged through the 896 day duration)	75
Figure 85: Simulated and Measured Pore Water Pressure Profiles in the Rock at a Depth of 2.45 m from the Floor of Room 213.....	76
Figure 86: Simulated and Measured Pore Water Pressure Profiles in the Rock at the Depth of 4.6 m from the Floor of Room 213.....	76

Figure 87: Water Pressures Measured in Hydraulic Piezometers 1RH1 – 1RH4 Close to Wall of Placement Borehole	77
Figure 88: Water Pressures Simulated in Locations of Hydraulic Piezometers 1RH1 – 1RH4 Close to Wall of Placement Borehole	78
Figure 89: Vertical Stresses in the Buffer at Locations 1BR1, 1BR3, 1BR4, 1BR5 and 1BG13.....	79
Figure 90: Horizontal Stresses in the Buffer at Locations 1BG2, 1BG4, 1BG6, 1BG8, 1BG10 and 1BG12.....	79
Figure 91: Simulated Vertical Displacements along a Vertical Line through the Axis of the Heater	80
Figure 92: Simulated Horizontal Displacements along a Horizontal Line through the Mid-height of Heater	81
Figure 93: Simulated Vertical Displacements along a Horizontal Line through the Mid-height of the Heater	81
Figure 94: Simulated Horizontal Displacements along a Vertical Line 0.368 m from the Axis of the Heater	82
Figure 95: Simulated Vertical Displacements along a Vertical Line 0.368 m from the Axis of the Heater	83
Figure 96: Simulated Horizontal Displacements along a Vertical Line 0.57 m from the Axis of the Heater	83
Figure 97: Simulated Vertical Displacements along a Vertical Line 0.57 m from the Axis of the Heater	84
Figure 98: Simulated Horizontal Stress Change Contours in the Rock at Four Different Times (Positive stress indicates tension)	85
Figure 99: Simulated Vertical Stress Change Contours in the Rock at Four Different Times (Positive stress indicates tension)	86
Figure 100: Comparisons of Simulated and Measured Vertical Displacements in the Rock	87

1. INTRODUCTION

The Canadian approach to the management of used fuel is Adaptive Phased Management recommended by the Nuclear Fuel Waste Management Organization (NWMO) (NWMO 2005) and accepted by the government of Canada (NRCan 2007). The Adaptive Phased Management Approach includes future isolation of used nuclear fuel in long-lived used-fuel containers in a deep repository located in a suitable geological formation, such as the crystalline rock of the Canadian Shield or Ordovician sedimentary rock.

The NWMO is conducting research and development in support of Adaptive Phased Management. This program includes advancing the technologies for implementing geological repository concepts. Repository concepts consist of a horizontal array of waste-placement rooms at a nominal depth of 500 to 1,000 m in the stable rock. The containers would be positioned either in boreholes drilled from these rooms (in-floor borehole or horizontal borehole placement method) or horizontally within the confines of each room (in-room placement method) (Maak and Simmons 2005). In either case, the containers are to be isolated by additional Engineering Barrier Systems (EBSs) that include clay-based buffer and backfills. These barriers would limit the rate of movement of contaminants, if any were released from the container.

A bentonite-sand buffer material has been considered as an engineered material that might be placed around the waste container to limit water movement and restrict container corrosion. The Buffer/Container Experiment, conducted by Atomic Energy of Canada Limited (AECL), investigated how heat affects the performance of a dense bentonite-sand buffer. The Isothermal Buffer/Rock/Concrete Plug Interaction Test (or commonly referred to as the Isothermal Test (ITT)) investigated the hydraulic interaction between the rock and the same dense bentonite-sand buffer without influence of thermal gradients. Both experiments were designed and installed at AECL's Underground Research Laboratory (URL) (Figure 1).

Some numerical modelling was done prior to testing to predict the thermally induced moisture migration, the thermal drying of the buffer, and the required heater power for a target temperature of 85°C in support of the design of the Buffer/Container Experiment (Radhakrishna et al. 1992). Later, sensitivity analyses were also done to investigate the effects of varying the thermal conductivity of the sand surrounding the heater between the heater and the buffer, the hydraulic conditions at the buffer/rock interface and the thermal conductivity of the buffer (Graham et al. 1997). The hydraulic response due to drilling the placement borehole, the water inflow from the surrounding rock to the borehole prior to placement of the buffer, the temperature changes in the surrounding rock before and after drilling and vertical displacements in the rock due to placement hole drilling were also modelled using FLAC (Chandler et al. 1992; Graham et al. 1997). Thermoporoelastic solutions were also conducted to examine potential gradients in water in the rock (Detournay and Berchenko 1994; Graham et al. 1997). Back-analyses were also conducted for the ITT and the Buffer/Container Experiment using COMPASS, a coupled thermohydromechanical finite element computer program (Thomas et al. 2002; Thomas et al. 2003).

In order to evaluate the effectiveness of several mathematical models in predicting the evolution of the coupled processes in unsaturated clay-based material, the information about the ITT and the Buffer/Container Experiment supplied by AECL has been shared with the international Engineering Barrier System Task Force modelling group (EBS TF modelling group) to compare

their modeling results to the measured results. AECL represents the NWMO as a member of the EBS TF modeling group.

This report describes the recently updated results of the coupled hydro-mechanical (H-M) analyses of the ITT and the thermo-hydro-mechanical (T-H-M) analyses of the Buffer/Container Experiment based on the previously modelling results (Guo and Dixon 2005 and Guo 2006). This report is part of the NWMO and AECL contribution to the EBS TF.

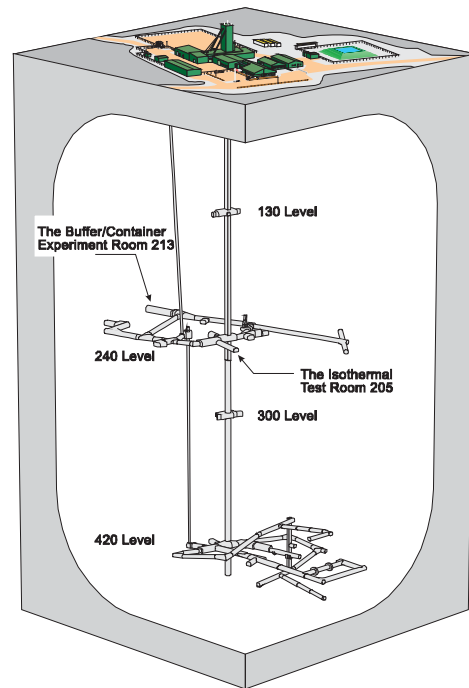


Figure 1: General Layout of the URL

2. THE ISOTHERMAL TEST

2.1 DESCRIPTION OF THE ISOTHERMAL TEST

The ITT was located on the 240 Level of the URL (Figure 2). Figure 3 presents the water pressures in the granite surrounding the 240 Level of the URL. Water pressures beyond approximately 30 m of the excavations are nearly hydrostatic (2.1 MPa).

2.1.1 Experiment Set-Up

The ITT was installed within a 5-m-deep by 1.24-m-diameter in-floor borehole in the unfractured, homogeneous, grey granite on the 240 Level of the URL (Figure 2). The buffer material (Dixon et al. 2001) was compacted in situ into the bottom 2 m of the borehole. A

1.25-m-thick concrete plug was placed over the compacted bentonite-sand buffer¹ to provide a vertical restraint against swelling (Figure 4). The bentonite-sand buffer material was a mixture of sodium bentonite and silica sand. Various instruments were installed in the bentonite-sand buffer in order to provide information on its rate of wetting and saturation. After installation of the experiment, the ITT was then left undisturbed and monitored for six and half years as it took on water from the surrounding rock. The rate of inflow from the surrounding rock to the bentonite-sand buffer was evaluated by measuring water inflow before bentonite-sand buffer installation and monitoring the hydraulic gradient in the surrounding rock. After the test, the bentonite-sand buffer material was sampled to determine water content and density changes.

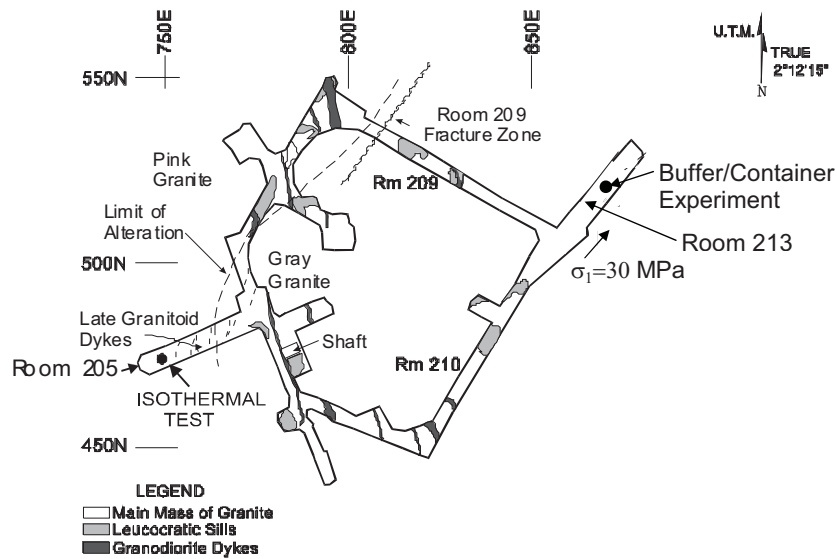


Figure 2: Plan Illustrating the Geology of the 240 Level and Location of the Isothermal Test (Graham et al. 1997)

¹ At the time of the experiment, the material was referred to as Reference Buffer Material (RBM). RBM is a 50:50 sand-bentonite mixture by that has been compacted to better than 95% ASTM Modified Dry Density – 1.67 Mg/m³ at a water content of 18%.

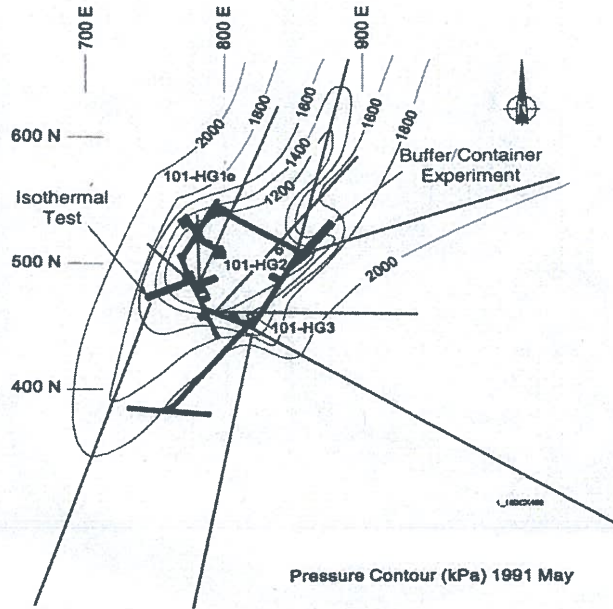


Figure 3: Groundwater Pressure (kPa) Contours at the 240 Level of the URL (Graham et al. 1997)

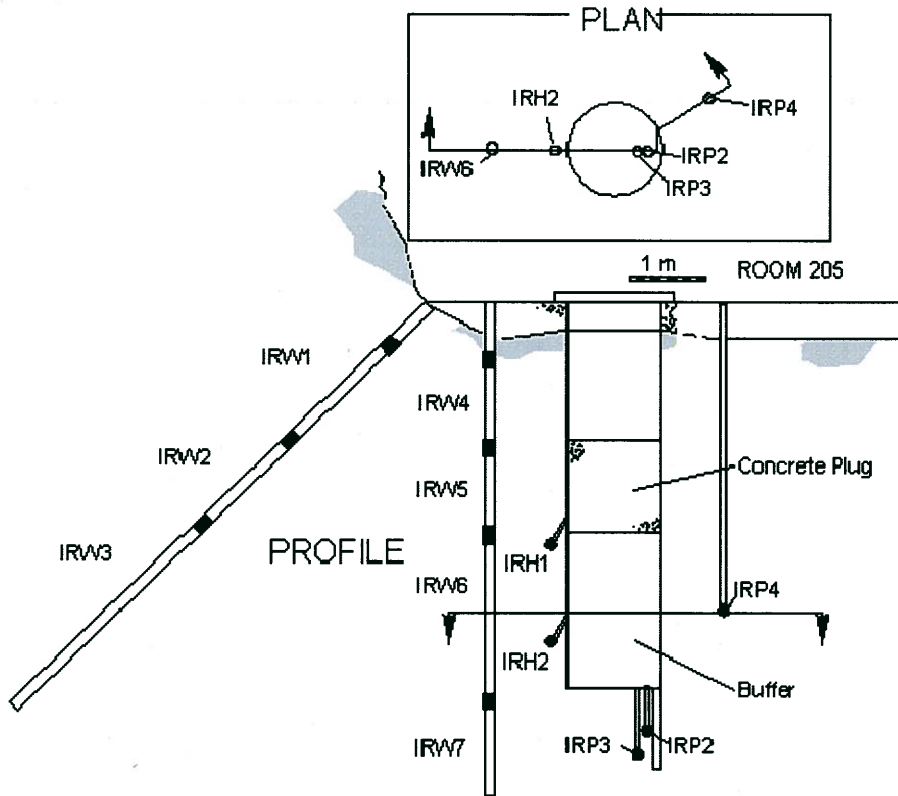


Figure 4: Location of Piezometers Surrounding the Isothermal Test (after Chandler 2000)

2.1.2 Phases Related to the Isothermal Test

The ITT consisted of the following three phases:

- During the first phase, the placement borehole was empty for a period of three years from 1989 March to 1992 September, during which time water seepage from the rock into the borehole was monitored for a period of 54 days from 1992 March 5 to 1992 April 27;
- During the second phase, the placement borehole was filled with bentonite-sand buffer and the earth pressure at the interface between the bentonite-sand buffer and the rock, the suction in the bentonite-sand buffer and the pore water pressure in the surrounding rock were monitored for a period of about 4.5 years from 1992 September 22 to 1997 February 10; and
- During the third phase, the material in the placement borehole was removed and the seepage was monitored again.

2.1.3 Instrumentation

A series of collection rings, illustrated in Figure 5, was installed to measure the inflow into the open borehole, before and after the ITT, providing physical measurement of the water influx from the rock. Four rings, SR1, SR2, SR3 and SR4, collected the inflow from different parts in the borehole. SR1 collected the water from the fractured rock in the floor of the tunnel and the interface between the rock and the concrete floor. SR2 collected the water from the rock location, corresponding to the concrete plug. SR3 and SR4 collected the seepage from the region that would be supplying water to the bentonite-sand buffer in the experiment. SR4 was not a collection ring but was a borehole drilled into the rock at the base of the placement borehole that collected seepage from the borehole wall below SR3 and the floor of the borehole.

Pore water pressures in the rock surrounding the borehole were monitored using different kinds of sensors (Figures 6 and 7). A system of packers was used to isolate borehole intervals (symbol IRW) in which the hydraulic pressure in the rock around the ITT was monitored. An average pressure measurement over each packed-off interval of a borehole was provided by these packers. Seven intervals (IRW1 to IRW7) were located in two boreholes at the end of Room 205 as shown in Figure 7. IRH1 and IRH2 were hydraulic piezometers installed in the rock in short boreholes drilled outward from the test boreholes (Figure 7). Pneumatic piezometer IRP4 was installed in a borehole parallel to the bentonite-sand buffer borehole at about the midpoint of the bentonite-sand buffer shown in Section D-D of Figure 8. Pneumatic and hydraulic piezometers measured the rock pore pressure at the tip of the sensor, as opposed to the packer systems that are used to monitor the average pressure in long intervals. The piezometers were all grouted within the boreholes to isolate the sensors at the tips of the boreholes. Locations of piezometers to measure the pressures in the rock below the placement borehole are also shown in Figure 7. Of these seven piezometers, two (IRP5 and IRP6) failed very early in the test and a third showed zero pore pressure (IRP8) throughout the test (Figure 8).

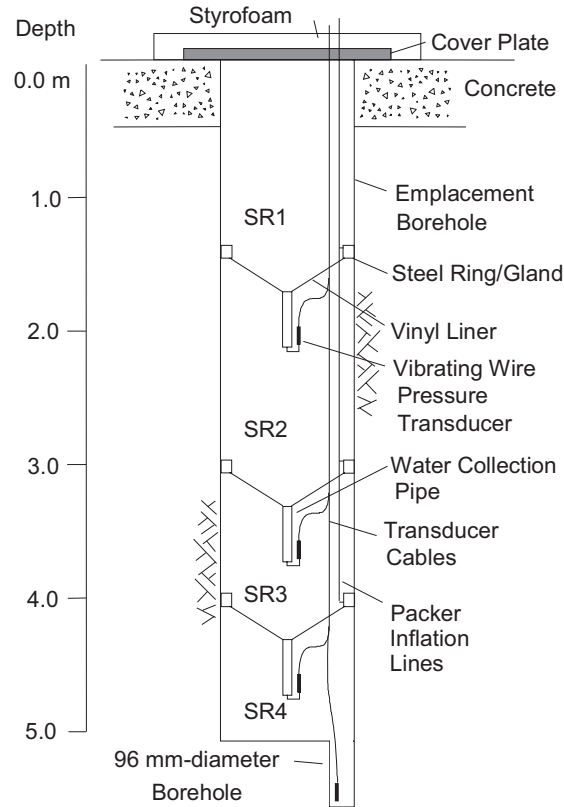


Figure 5: Configuration of the Isothermal Test Seepage Collection System (Chandler 2000)

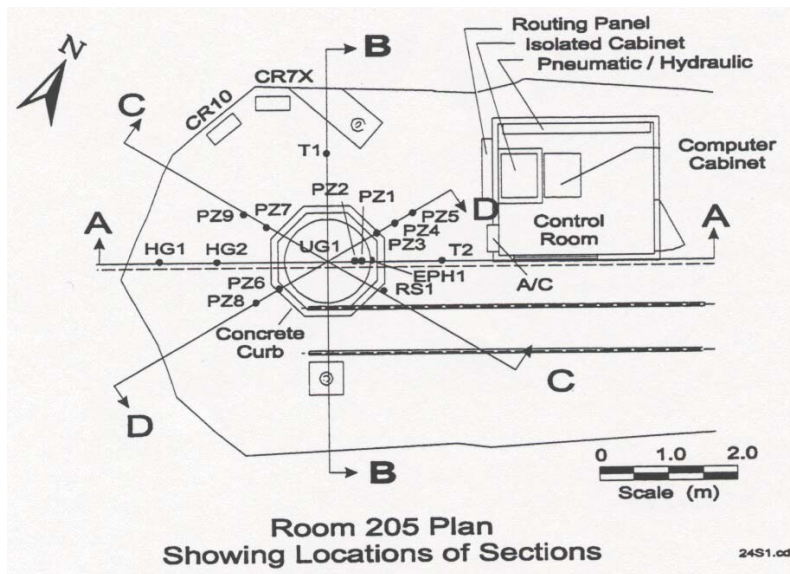


Figure 6: Plan View of the Isothermal Test (Dixon et al. 2001)

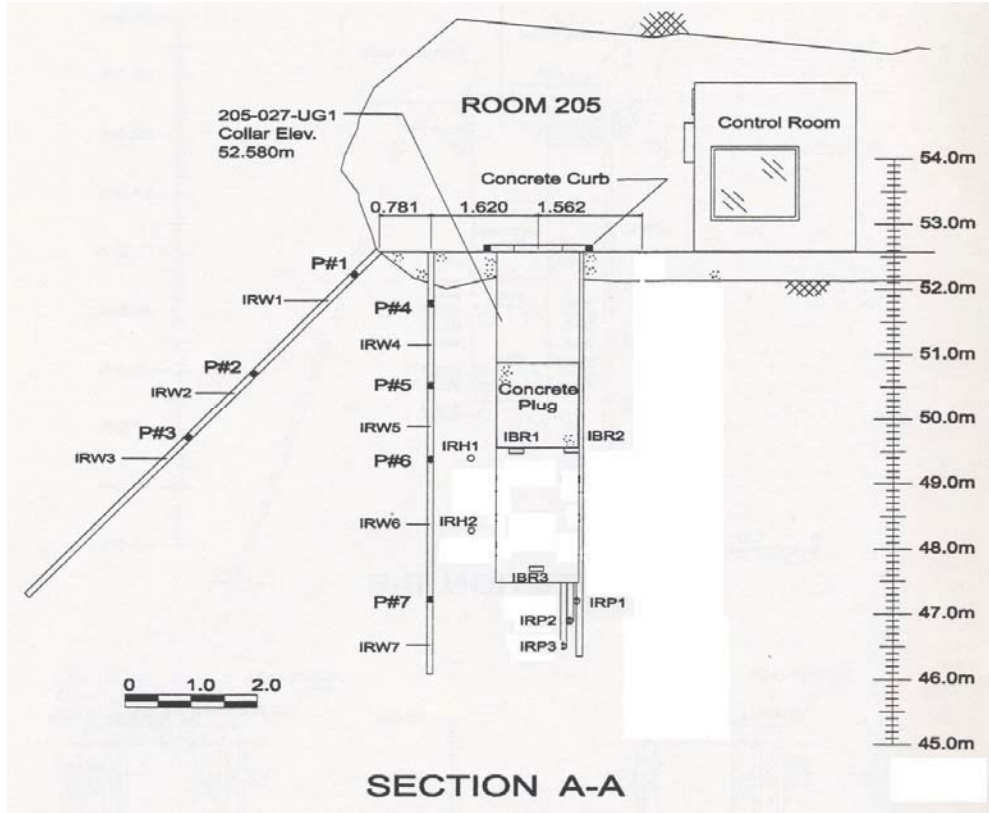


Figure 7: Cross-section A-A of the Isothermal Test Installation (Dixon et al. 2001)

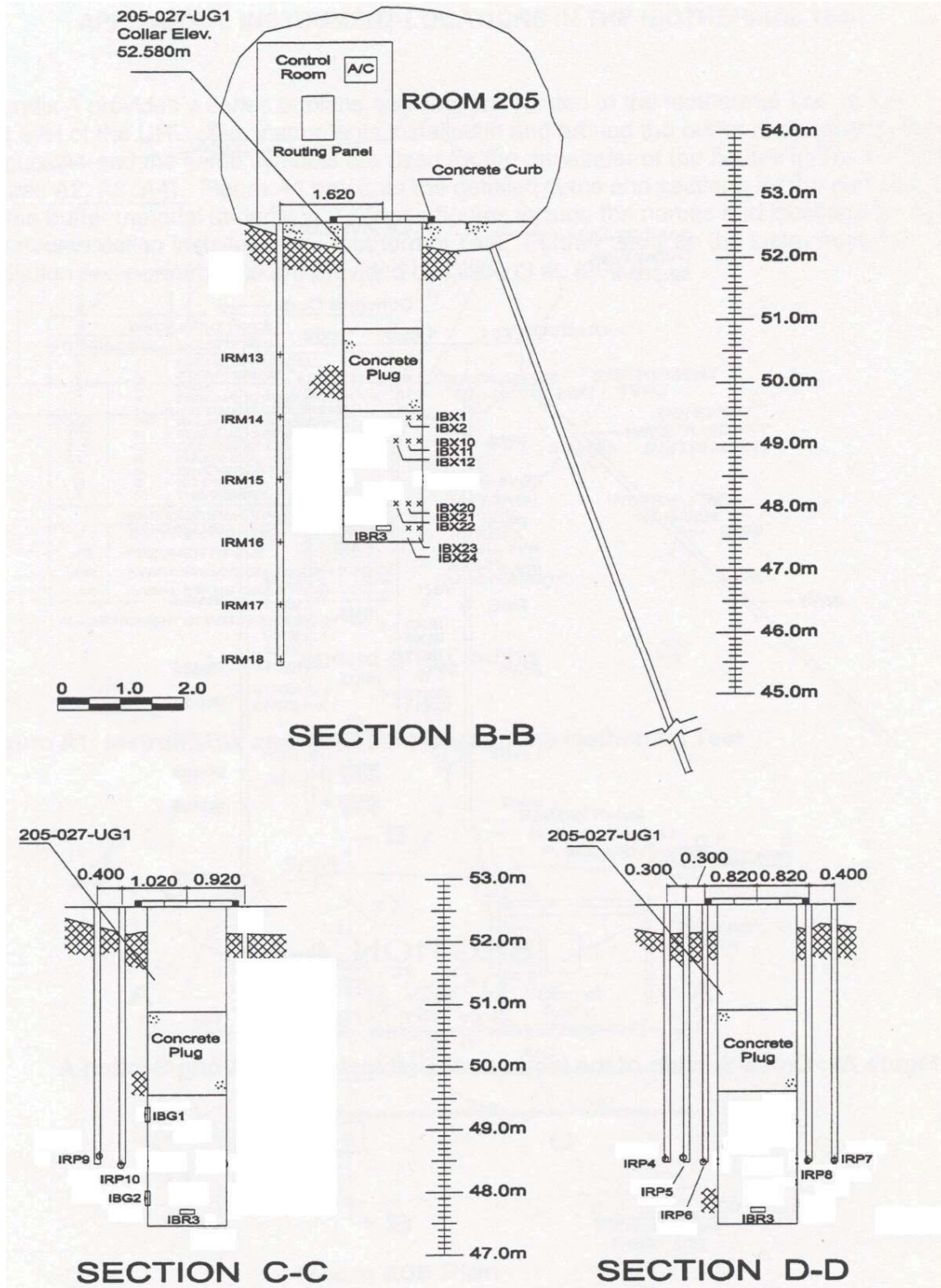


Figure 8: Cross-sections of Isothermal Test Showing Instrumentation Layers along Sections B-B, C-C and D-D (Dixon et al. 2001)

There were 24 thermocouple psychrometers installed in the bentonite-sand buffer to measure the suction (moisture content) during the course of the experiment. The locations of 10 psychrometers are shown on Section B-B in Figure 8.

There were three pneumatic Roctest earth pressure cells installed horizontally in the bentonite-sand buffer, two at the buffer-concrete plug interface (IBR1 and IBR2) and one near the buffer-rock interface (IBR3) (Figure 7). Two Geonor total earth pressure cells (IBG1 and IBG2) were mounted vertically in the interface between the rock and the bentonite-sand buffer and their locations are shown in Section C-C of Figure 8.

During the decommissioning stage, thorough sampling to determine the water content and density determination of the bentonite-sand buffer was conducted (Dixon and Chandler 2000) with up to 107 moisture content samples and 33 density samples being taken at each of the eight elevations sampled. Locations of sampling on plan are shown in Figure 9. The distance between each sampling elevation averaged about 0.25 m as shown in Table 1.

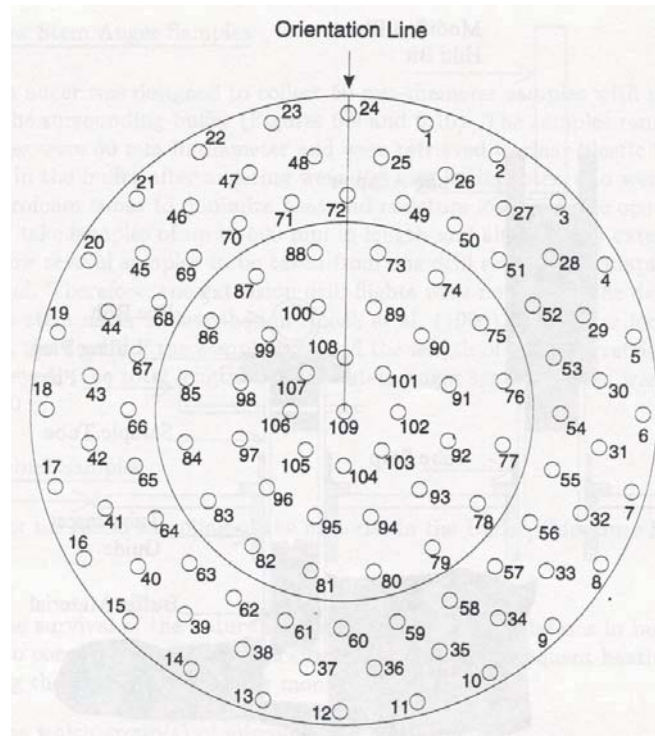


Figure 9: Layout and Numbering System Using Template for Moisture Content Sampling (Dixon et al. 2001)

Chandler (2000) modelled the initial seepage into the borehole and the pore pressure change in the rock using FLAC (Fast Lagrangian Analysis of Continua²) and compared the simulated

² FLAC is an explicit finite difference program for engineering mechanics computation and was developed by Itasca Consulting Group, Inc.

results with the measured results. Thomas et al. (2002) modelled both the seepage into the empty borehole and the moisture movement in the rock and the buffer using COMPASS.

Olsen (1960) derived an equation, which calculates the relationship between the hydraulic conductivity and void ratio. The Olsen method reflects the influence of the density change of the bentonite on its hydraulic conductivity. The Olsen method (Olsen 1960) was applied in Thomas et al. (2002) to get a good match between the simulated pore water pressure in the buffer and the end-of-test suction inferred from measured moisture content and density.

Table 1: Depth of Moisture Content Relative to the Top Surface of the Buffer

Layer designation	Moisture content sample depth below the buffer surface (m)
A	0.05
B	0.31
C	0.61
D	0.81
E	1.07
F	1.31
G	1.62
H	1.81

2.2 MODEL GEOMETRY, BOUNDARY CONDITIONS AND INITIAL CONDITIONS

This report describes both hydraulic-only and coupled hydromechanical (H-M) simulations that were performed on the ITT using CODE_BRIGHT. CODE_BRIGHT is a finite-element program for modelling thermohydromechanical (T-H-M) processes in a coupled way in geological media, including moisture transfer in unsaturated soil. GiD was used for pre-processing and post-processing the CODE_BRIGHT input and output data. GiD is a commercial graphical user interface, developed by the International Center for Numerical Methods in Engineering, for the definition, preparation and visualization of the data related to numerical simulations.

2.2.1 Model Geometry

The two-dimensional axisymmetric model of the ITT is shown in Figure 10. The overall outside radius of the model is 20 m and the height is 30 m. The bottom of the model is 10 m from the borehole bottom and the upper boundary of the model is 10 m from the roof of Room 205.

2.2.2 Boundary Conditions

2.2.2.1 Hydraulic Boundary Conditions

The local groundwater pressure was about 1420 kPa at the 240 Level near the ITT (Graham et al. 1997). Using this value, the hydraulic pore water pressure at the bottom of the

model was fixed at 1560 kPa. The top of the model was fixed at 1260 kPa. The pore pressure along the outside boundary of the model varied linearly with a value of 1260 kPa at the top end and a value of 1560 kPa at the bottom end. There was no fluid flow at the boundary that corresponded to the centre of the axisymmetric model, at the coordinate $X = 0$. On the boundary representing the surface of Room 205, the pore pressure was fixed at -360 kPa based on back-analysis of the pore pressure change of the rock before buffer placement.

2.2.2.2 Mechanical Boundary Conditions

The top boundary and the bottom boundary of the model were fixed in the Y-direction and the outside boundary of the model was fixed in the X-direction.

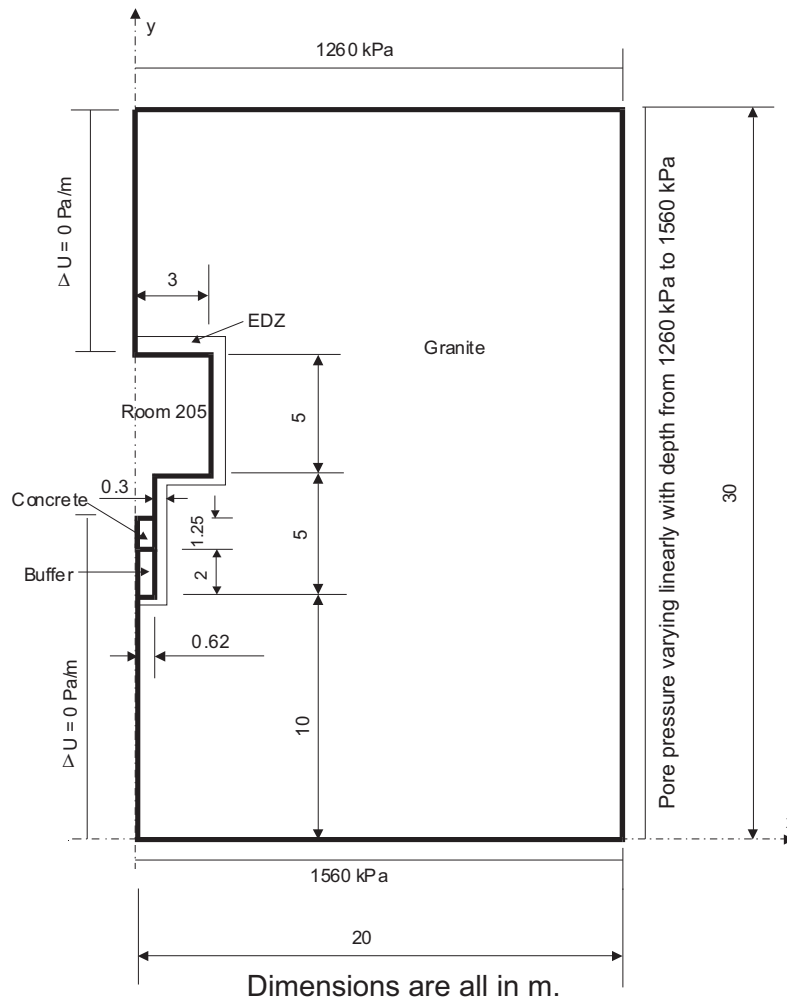


Figure 10: Dimensions of the Model Geometry and Hydraulic Boundary Conditions

2.2.3 Initial Boundary Conditions

The pore pressure change due to borehole and room excavation prior to filling the borehole with buffer or concrete was modelled. The initial pore water pressure in the model was linearly distributed with depth with a pore pressure of 1260 kPa at the top of the model and 1560 kPa at the bottom of the model. The pore pressure in the rock was computed using -360 kPa as a rock surface pressure. The resulted pore pressure and the derived stresses were used as the initial hydraulic and mechanical conditions in the rock for the modelling after buffer placement.

The initial pore water pressure in the “as-placed” sand/clay buffer was set at -4.4 MPa, calculated using the soil-characteristic curve described in Section 2.3 and the as-placed degree of saturation for the buffer. The concrete cap was assumed to be impermeable.

2.2.4 Discretization Of The Model

The discretization of the 2-D axisymmetric model is illustrated in Figure 11. There were 898 nodes and 827 four-noded elements. The size of the elements around the interface between the rock and the buffer was set smaller than those elements farther from the interface.

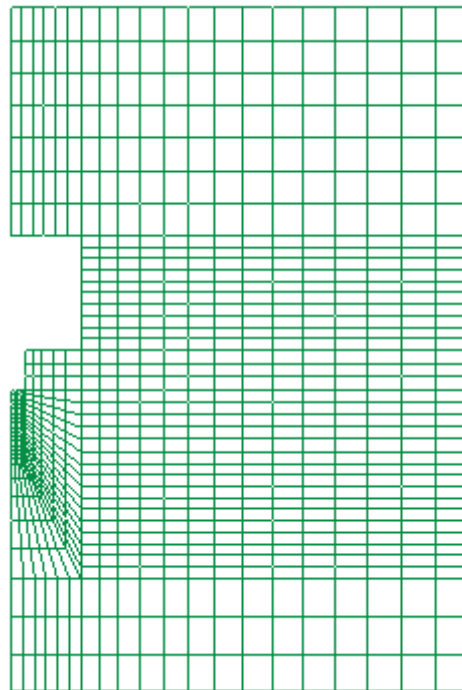


Figure 11: 2-D Axisymmetric Four-noded Finite Element Mesh

2.3 MATERIAL PARAMETERS

The modelled domain consisted of three different materials: the 50:50 bentonite-sand buffer, the granite and the concrete. For the simulations described in this report, the concrete plug was assumed to be impermeable and therefore, its hydraulic material parameters were not input. The bentonite-sand buffer was assumed to be a poroelastoplastic material. The granite rock was assumed to be a linear poroelastic material.

2.3.1 Bentonite-Sand Buffer Material Parameters

2.3.1.1 Hydraulic Parameters of Materials

The buffer was compacted in situ with initial gravimetric moisture content of 17.5% and an initial dry density of 1720 kg/m³. Initial porosity of the buffer was 0.359. Therefore, the initial saturation of the buffer was 84.3%. The relationship between water content and suction for the unsaturated buffer was derived from the results of three different types of free swell tests (Wan 1996). Wan described the psychrometer, vapour equilibrium and filler paper tests used to define the soil-water retention relationship in Figure 12. Wan was able to uniquely define suction in terms of gravimetric water content, as shown, but was unable to define suction uniquely as a function of degree of saturation. The relationship between degree of saturation (S_r) and gravimetric water content (w) is also dependent on dry density (γ_d), as defined in the following equation:

$$S_r = \frac{w}{\frac{\gamma_w}{\gamma_d} - \frac{1}{G_s}} \quad (1)$$

where γ_w = water density (i.e., ~1 Mg/m³); and
G_s = relative density of the buffer (i.e., assumed as 2.7).

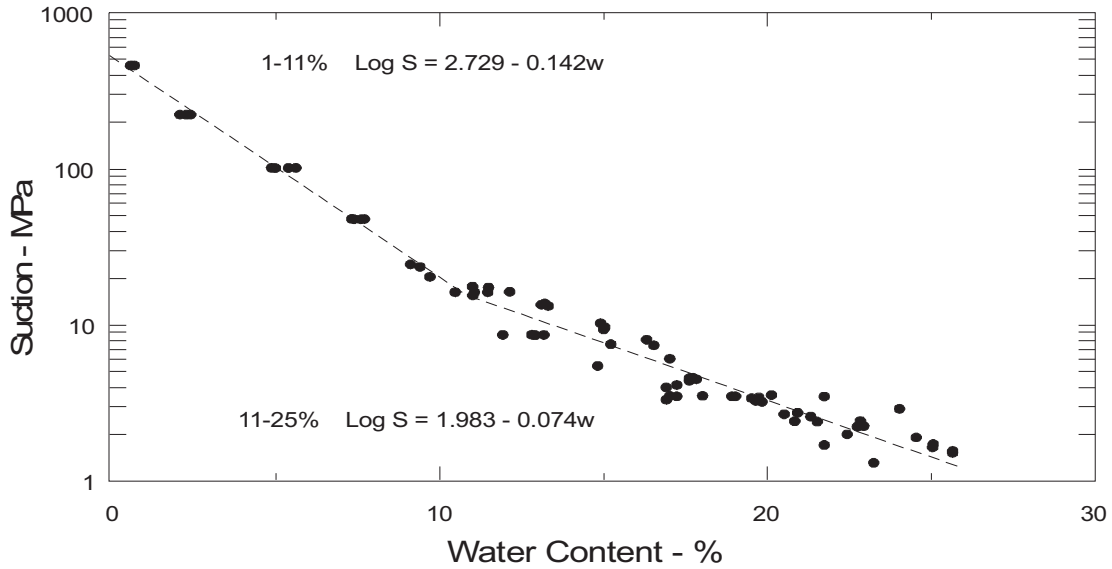


Figure 12: Suction - Water Content Relationship for Buffer Materials (Wan et al. 1995; Graham et al. 1997)

The suction versus water content relationship for 11% ~ 25% water content in Figure 12 can be rewritten as follows:

$$w = \frac{1.983 - \log s}{0.074} \quad (2)$$

The retention curve for constant volume, i.e., dry density unchanged at 1.73 Mg/m^3 , was estimated by substituting (2) into (1) (Figure 13). The suction-saturation relationship can be fitted to Van Genuchten-type equation used in CODE_BRIGHT:

$$S_r = \left[1 + \left(\frac{s}{P_0} \right)^{1/(1-\beta_1)} \right]^{-\beta_1} \quad (3)$$

where s is suction in MPa;
 S_r is the degree of saturation;
 P_0 is the air entry value; and
 β_1 is a curve fitting parameter.

From regression analysis, it was determined that P_0 was 7.0 and β_1 was equal to 0.73.

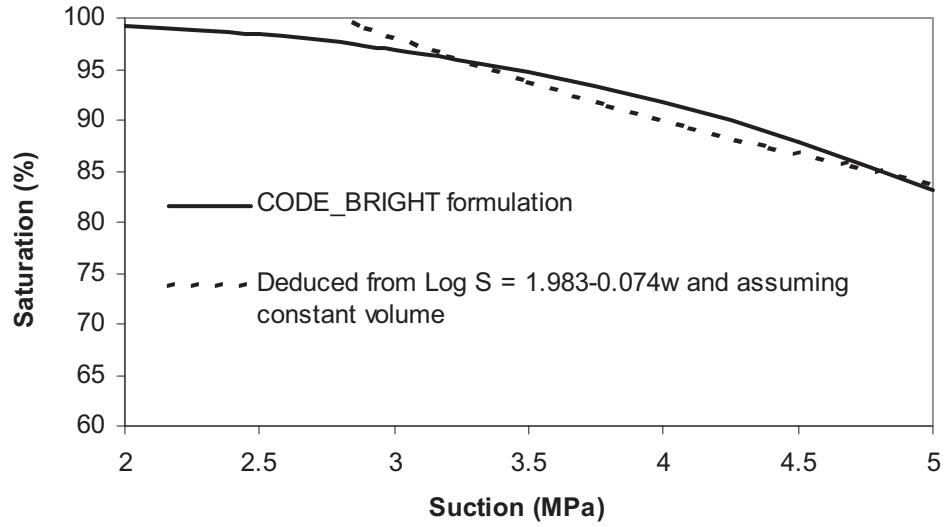


Figure 13: Saturation of the Buffer versus Suction

The hydraulic conductivity of the buffer has been described as a function of its saturation (Green and Corey 1971) (Figure 14), which can be fitted using the following regression equation (proposed by Gens et al. 1998):

$$k = k_0 \cdot S_r^{1/2} (1 - (1 - S_r^{1/\beta})^\beta)^2 \quad (4)$$

where k is the hydraulic conductivity of the unsaturated buffer in m/s;
 k_0 is the saturated hydraulic conductivity, taken to be equal to 1×10^{-12} m/s for this analysis; and
 β is a regression parameter, taken to be 0.3, a value typical for bentonite-sand (Table 2).

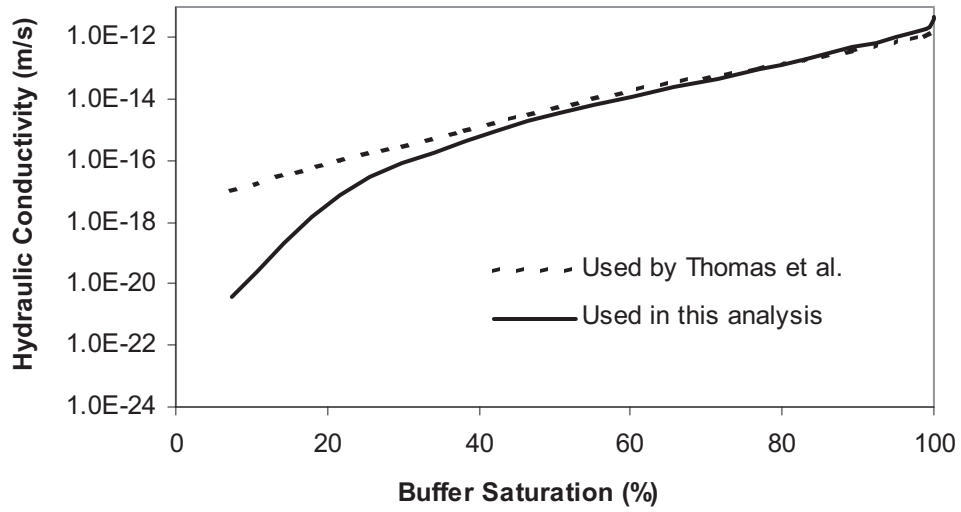


Figure 14: Hydraulic Conductivity of the Buffer as a Function of Buffer Saturation

Table 2: Hydraulic Parameters of the Buffer and Granite Rock

Material Parameters	Buffer	Granite Rock
Water retention curve (Pa)	$S_r = \left[1 + \left(\frac{S}{P_0} \right)^{1/(1-\beta_1)} \right]^{-\beta_1}$ $P_0 = 7.0; \beta_1 = 0.73$	$S_r = \left[1 + \left(\frac{S}{P_0} \right)^{1/(1-\beta_1)} \right]^{-\beta_1}$ $P_0 = 0.7; \beta_1 = 0.33$
Hydraulic conductivity (m/s)	$k = k_0 \cdot S_r^{1/2} (1 - (1 - S_r^{1/\beta})^\beta)^2$ $k_0 = 1 \times 10^{-12}; \beta = 0.3$	$k = k_0 \cdot S_r^{1/2} (1 - (1 - S_r^{1/\beta})^\beta)^2$ $k_0 = 4 \times 10^{-13}; \beta = 0.345$
Porosity	0.369	0.005
Dry density (Mg/m ³)	1.73	2.63
Initial saturation (%)	84.3	100

2.3.1.2 Mechanical Parameters

The Barcelona Basic Model, an elasto-plastic model, was used to simulate the clay-sand buffer. In order to help understand the selection of parameters, some of the mechanical equations used in this modelling are presented in the following section (Alonso et al. 1990).

The volumetric elastic strain ($d\varepsilon_v^e$) can be calculated using the following equation:

$$d\varepsilon_v^e = \frac{k}{1+e} \frac{dp'}{p'} + \frac{k_s}{1+e} \frac{ds}{s+0.1} \quad (5)$$

where p' is the mean effective stress and is equal to $\frac{1}{3}(\sigma_x + \sigma_y + \sigma_z) - \max(p_g, p_l)$;

p_g is the pore gas pressure;

p_l is the pore liquid pressure;

k_s is a compressibility coefficient for strain in response to changes in suction (s); and

k is a compressibility coefficient for the response to mean stress changes.

The plastic strain can be obtained by plastic theory. The equations for the yield curve in (p' , s) space is:

$$\left(\frac{p_0}{p^c}\right) = \left(\frac{p_0^*}{p^c}\right)^{[\lambda(0)-k]/[\lambda(s)-k]} \quad (6)$$

where p_0 is preconsolidation stress at varying suction (s);

p_0^* is preconsolidation stress for saturated conditions, its value is 1 MPa (Blatz and Graham 2003);

p^c is a reference stress; and

$\lambda(s)$ is the stiffness parameter at a given suction (s).

$\lambda(s)$ is calculated by:

$$\lambda(s) = \lambda(0)[(1-r)\exp(-\beta s) + r] \quad (7)$$

where $\lambda(0)$ is the stiffness parameter at saturation;

r is a parameter defining the maximum soil stiffness;

s is suction; and

β is a constant describing the rate of increase in soil stiffness with suction.

The values of $\lambda(0)$, r , β and p_c were calculated by Thomas et al. (2002) using the experiment data from Blatz and Graham (2003) and from Lingnau et al. (1995). Thomas et al.'s values are:

$$r = 0.65 \quad \beta = 5 \times 10^{-7} \text{ Pa}^{-1} \quad p_c = 1.8 \times 10^5 \text{ Pa.}$$

The values for the other parameters used in this modelling are also the same as those in Thomas et al. (2002). They are: $\lambda(0) = 0.0597$; $k = 0.0125$; $k_s = 0.0111$; shear modulus $G = 10$ MPa; Poisson's ratio $\nu = 0.2$; and the slope of the critical state line $M = 0.526$ (Table 3).

2.3.2 Granite Rock Material Parameters

2.3.2.1 Hydraulic Parameters

The retention formula for the granite was the same as Equation 3 with β_1 assumed to be 0.33 from Gens et al. (1998). P_0 is the air entry value, taken as 0.7 for granite (Thomas et al. 2002). The hydraulic conductivity for the granite rock was expressed using Equation 4. The regression parameter β was taken as 0.345. The hydraulic conductivity of the saturated rock was 4×10^{-13} m/s (Table 2).

Table 3: Mechanical Parameters of the Buffer and Granite Rock

Material Parameters	Buffer	Granite Rock
p_0^* (MPa)	1.0	N/A
$\lambda(0)$	0.0597	N/A
k	0.0125	N/A
r	0.65	N/A
ξ (Pa ⁻¹)	5×10^{-7}	N/A
p^c (Pa)	1.8×10^5	N/A
λ_s	0.111	N/A
k_s	0.0111	N/A
G (MPa)	10,000	N/A
M	0.526	N/A
s_0 (MPa)	4.4	N/A
E (MPa)	-	60
ν	-	0.22

2.3.2.2 Mechanical Parameters

The granite rock was assumed to be linear elastic. Its Young's modulus was set as 60 MPa and its Poisson's ratio was set as 0.22 (Graham et al. 1997) (Table 3).

2.3.3 Concrete Cap Parameters

The hydraulic conductivity of the concrete cap was not considered in this modelling. The concrete was also assumed to be elastic, with its mechanical parameters assumed to be the same as those of the rock.

2.4 MODELLED RESULTS AND COMPARISON WITH MEASURED DATA

2.4.1 Influence of Excavation Damage Zone on the Pore Water Pressure in the Rock before Buffer Installation

A series of the modelling exercises was conducted to investigate the influence of the hydraulic conductivity of the excavation damage zone (EDZ) on the pore water pressure in the rock. The thickness of the EDZ was set to about 30 cm.

Five different cases were simulated.

1. Without EDZ and without allowing desaturation of the rock to affect its hydraulic conductivity.
2. With an EDZ having a hydraulic conductivity of 1×10^{-12} m/s and without allowing desaturation to affect the hydraulic conductivity of the rock.
3. With an EDZ having a hydraulic conductivity of 8×10^{-13} m/s and without allowing desaturation to affect the hydraulic conductivity of the rock.
4. With an EDZ having a hydraulic conductivity of 5×10^{-12} m/s and without allowing desaturation to affect the hydraulic conductivity of the rock.
5. With an EDZ having a hydraulic conductivity of 8×10^{-13} m/s and allowing desaturation to affect the hydraulic conductivity of the rock.

Comparisons of the simulated pore water pressure in the rock to the measured data for each case modelled is shown in Figure 15. Without allowing desaturation of the rock to affect the hydraulic conductivity of the rock, the simulated pore water pressure (see Cases 1, 2 and 3) was close to the measured data. The best fit was Case 3, which used an EDZ having a hydraulic conductivity of 8×10^{-13} m/s, an EDZ thickness of 30 cm and a negative pore water pressure of 360 kPa applied on the surface of the borehole.

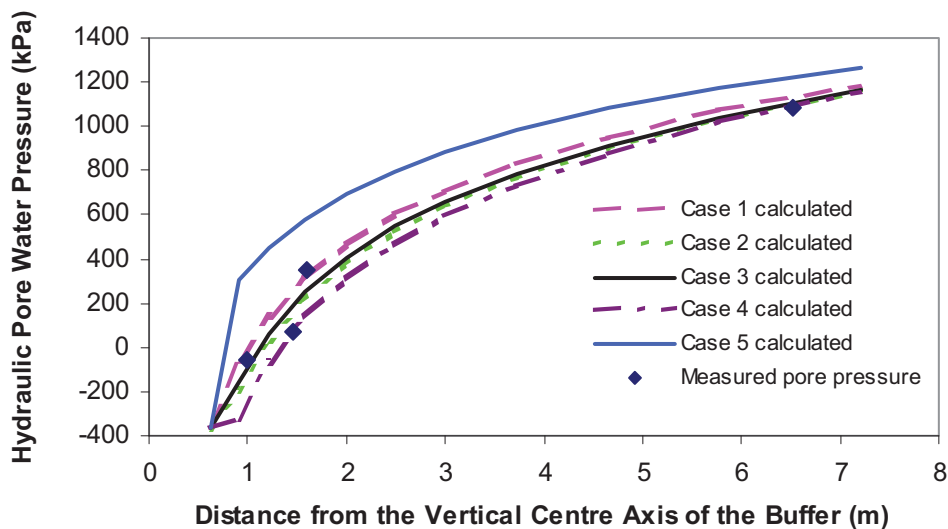


Figure 15: Pore Water Pressures in the Rock prior to Placing the Buffer

When the influence of desaturation of the rock on the hydraulic conductivity was considered (Case 5), there was a large difference between the simulated pore water pressure and the measured data even though the hydraulic conductivity of the EDZ was set to ten times that of the undamaged rock. The rationale for not expecting desaturation of the pores and the micro-cracks of the EDZ to affect the results is that the inflow from the micro-cracks accounted for most of the inflow from the wall of the borehole and the pore water pressure at these micro-cracks was zero. Later, once the buffer was placed into the borehole, the micro-cracks were isolated by the expansive buffer, and the 4.4 MPa suction in the buffer caused the pore pressure in the micro-cracks to become negative, the seepage from the micro fractures may not be as important as it was when the borehole was empty. Therefore, desaturation of the rock would influence the hydraulic conductivity of the rock after the buffer was placed in the borehole.

2.4.2 Seepage Prior To The Buffer Placement

The borehole had been open for three years before the buffer and concrete cap were installed. Chandler (2000) had modelled the initial seepage into the borehole using FLAC (Fast Lagrangian Analysis of Continua), a finite-difference model, and Thomas et al. (2002) had modelled the initial water seepage by applying a -250 kPa hydraulic pressure on the surfaces of Room 205 and the borehole using the finite-element program COMPASS. The first modelling task described in this report, using CODE_BRIGHT, was performed on the pore water pressure evolution during the three years before the buffer placement. In this model, the EDZ was set at the first layer of the elements around Room 205 and the borehole with a thickness of about 30 cm.

Although desaturation of the rock can influence its hydraulic conductivity, in this modelling the influence of desaturation on the rock hydraulic conductivity was not a factor, as described in Section 2.4.1. Based on a back-analysis that best matched the measured and simulated pore water pressure in the rock, the hydraulic conductivity of the rock was selected to be 4×10^{-13} m/s and a layer of excavation-induced damaged rock (EDZ) existed with a hydraulic conductivity of 8×10^{-13} m/s.

Table 4 shows the measured and calculated water inflow from the rock using FLAC, COMPASS and CODE_BRIGHT. All of the calculated inflows for Zones SR1 and SR2 using FLAC, COMPASS and CODE_BRIGHT were greater than the measured data and for SR4 were less than the measured data. All three simulations provided a reasonable estimate of inflow for SR3. The total results calculated using COMPASS and CODE_BRIGHT were both greater than those using FLAC because both the COMPASS and CODE_BRIGHT models incorporated an EDZ. The total inflow calculated using CODE_BRIGHT was greater than the results from the COMPASS model because the CODE_BRIGHT model did not consider the influence of the desaturation on the hydraulic conductivity of the EDZ. Overall, the total inflow into the borehole was simulated reasonably well using CODE_BRIGHT, and the results were in the same range as Chandler (2000) and Thomas et al. (2002).

Table 4: Measured and Calculated Inflow from the Wall of the Borehole

Seepage Collection Zone	Measured x 10 ⁻⁶ l/min	FLAC (not EDZ) x 10 ⁻⁶ l/min	COMPASS (EDZ) x 10 ⁻⁶ l/min	CODE_BRIGHT (EDZ) x 10 ⁻⁶ l/min
Uppermost region SR1	1.6	2.9	2.2	4.2
SR2	2.7	8.0	8.2	8.6
SR3	10.0	8.5	8.5	11.7
SR4 Borehole base	34.0	15.4	23.4	20.3
Total	48.3	34.8	42.3	44.6

2.4.3 Pore Water Pressure In The Rock

The simulated pore water pressure contour of the rock prior to placement of the clay/sand buffer is presented in Figure 16. Figures 17 and 18 show the simulated pore water pressure contours of the rock after 1000 and 2400 days of placement of the buffer, respectively. Comparison of Figures 17 and 18 to Figure 16 shows there are no differences in the pattern of the simulated pore water pressure distribution except in the area immediately around the unsaturated buffer in borehole.

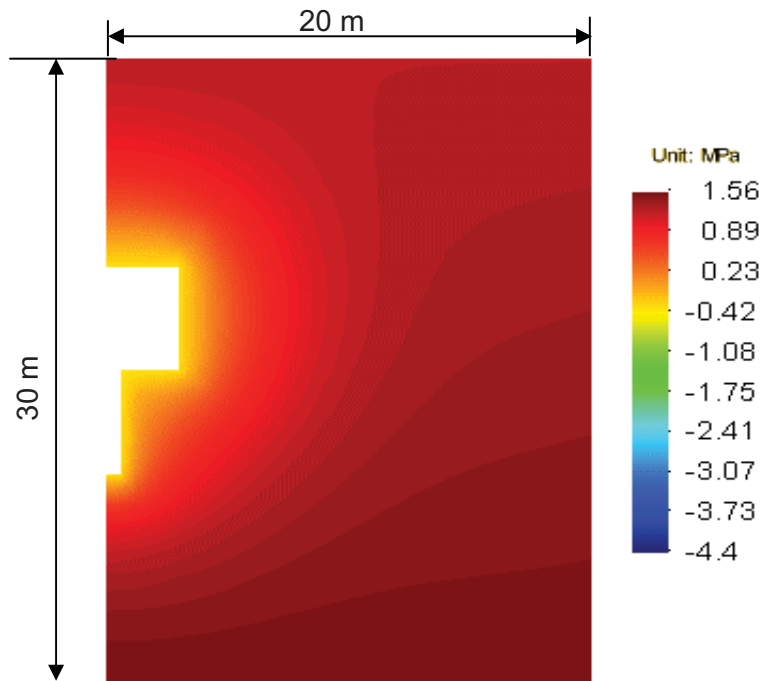


Figure 16: Pore Water Pressure Contour in the Rock before Placing the Buffer

The simulated pore water pressure in the rock adjacent to the buffer was negative after placing the buffer.

The simulated equipotentials of pore water pressure in the rock after 2400 days of placing the clay/sand buffer are compared with the measured pressures in Figure 19. The measured data at central locations of the packer intervals IRW1 to IRW7 are also shown in Figure 19. The simulated pore pressure matched the measured data reasonably well.

The simulated pore water pressure is compared with the measured pore water pressure in the rock along the line at mid-height of the buffer shown in Figure 20. The simulated pore water pressure matched the measured data very well with the possible exception of IRP4 at 2350 days.

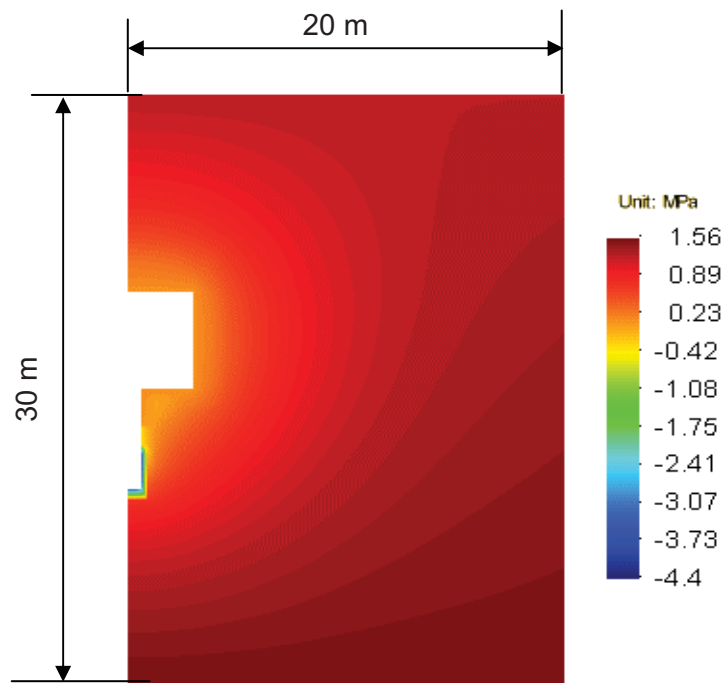


Figure 17: Pore Water Pressure Contour in the Rock 1000 Days after Placing the Buffer

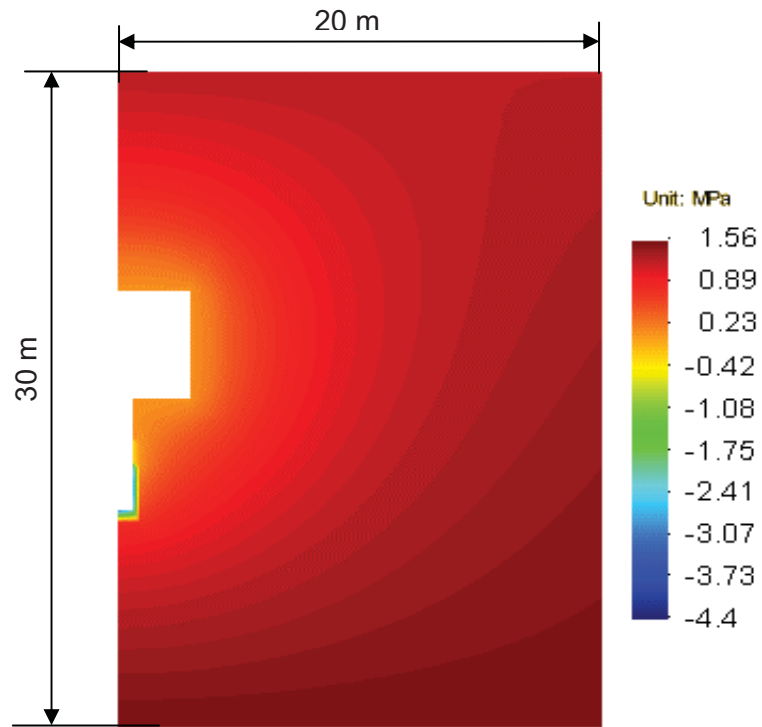


Figure 18: Pore Water Pressure Contour in the Rock 2400 Days after Placing the Buffer

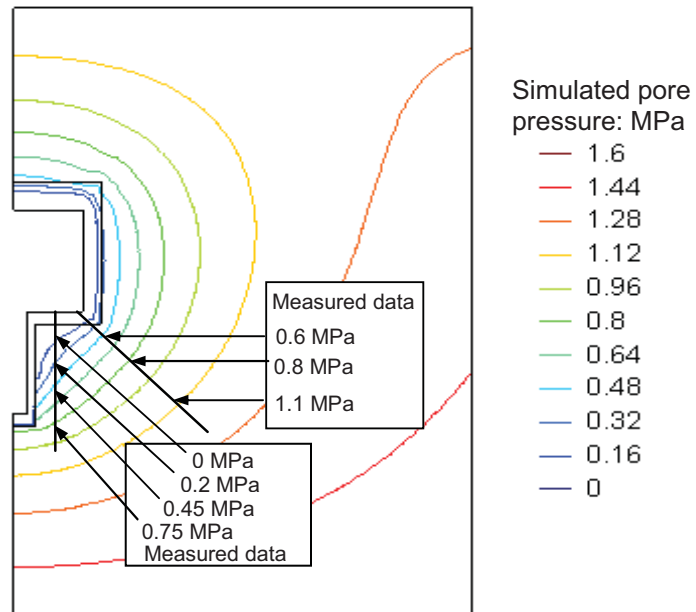


Figure 19: Simulated Pore Water Pressure Contours in the Rock Compared to Measured Data 2400 Days after Placing the Buffer

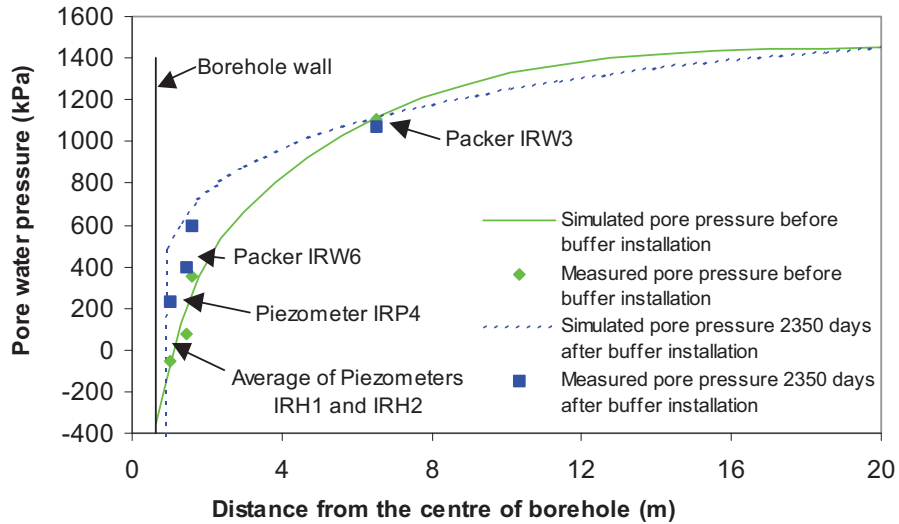


Figure 20: Mid-height Values of Pore Water Pressure in the Rock

The simulated pore water pressure evolution is compared to measured data at locations of IRP2, IRP3 and IRP4 in Figure 21. Based on their locations (refer to Figure 4), the simulations indicated that IRP3 should have readings higher than IRP2 but this was not observed. Instead IRP3 read some 200 kPa lower than predicted and less than IRP2. The cause of these differences, as well as the sudden pore pressure jump at IRP2 on day 550 have not been determined. IRP4 shows a trend similar to that predicted but consistently read lower than the prediction.

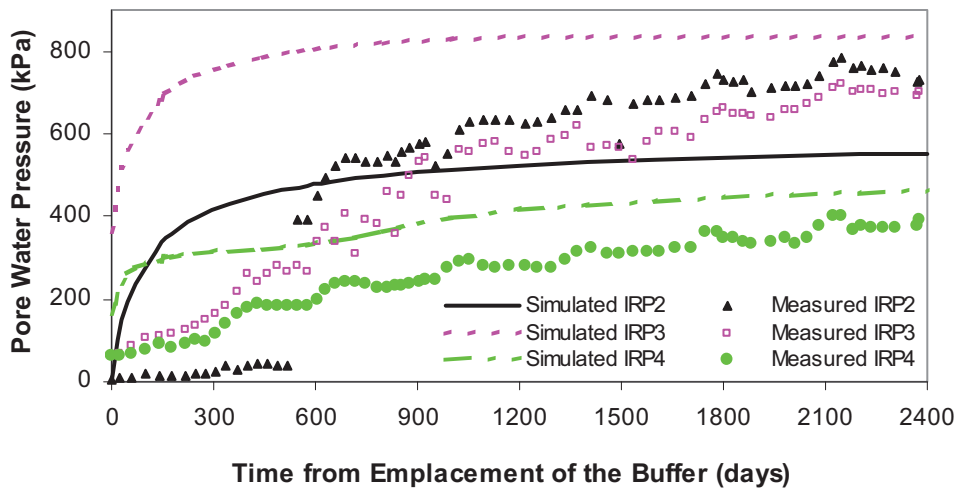


Figure 21: Pore Water Pressure Evolutions at Locations IRP2, IRP3 and IRP4

Figure 22 compares the simulated pore water pressure radially outwards into the granite at buffer mid-height from a hydraulic-only model and from a coupled H-M model at two times;

before buffer installation and 2350 days after installation. Except for locations near the buffer, there was no discernible difference in the hydraulic response between the coupled and uncoupled models. This is due to the fact that there was no large change in stresses in the rock. Therefore, the mechanical response of the rock was not shown in this report.

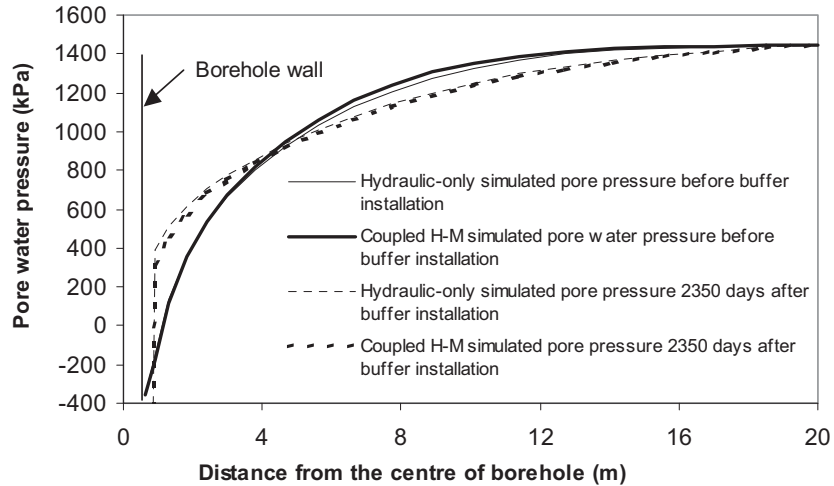


Figure 22: Comparison of the Rock Pore Pressure Computed Using a Hydraulic-Only Model and a Coupled H-M Model

2.4.4 Hydraulic Results In The Buffer

Figures 23, 24 and 25 shows the predicted suctions in the buffer along a horizontal line 0.5 m, 1.0 m and 1.5 m from the bottom of the buffer at four different times, respectively. It can be seen that the buffer was far from full saturation whether the buffer was located in the centre or near the interface between the buffer and the rock.

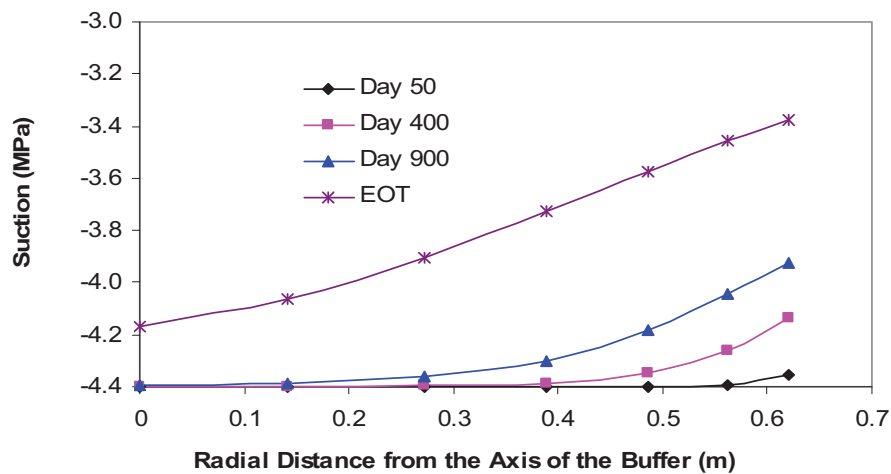


Figure 23: Suction Predictions at 0.5 m Height from the Bottom of Buffer vs. Distance from the Borehole Centreline for Different Times

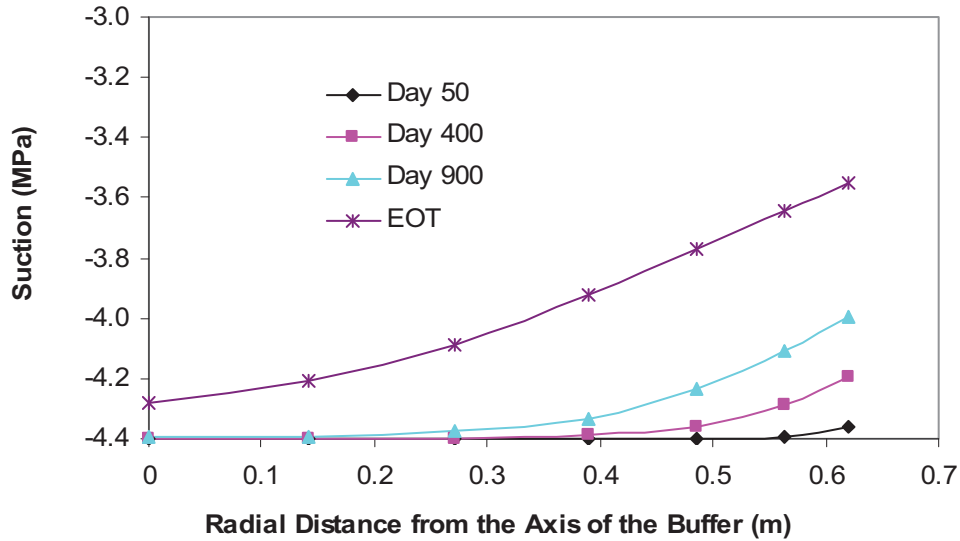


Figure 24: Suction Predictions at Mid-Height of Buffer vs. Distance from the Borehole Centreline for Different Times

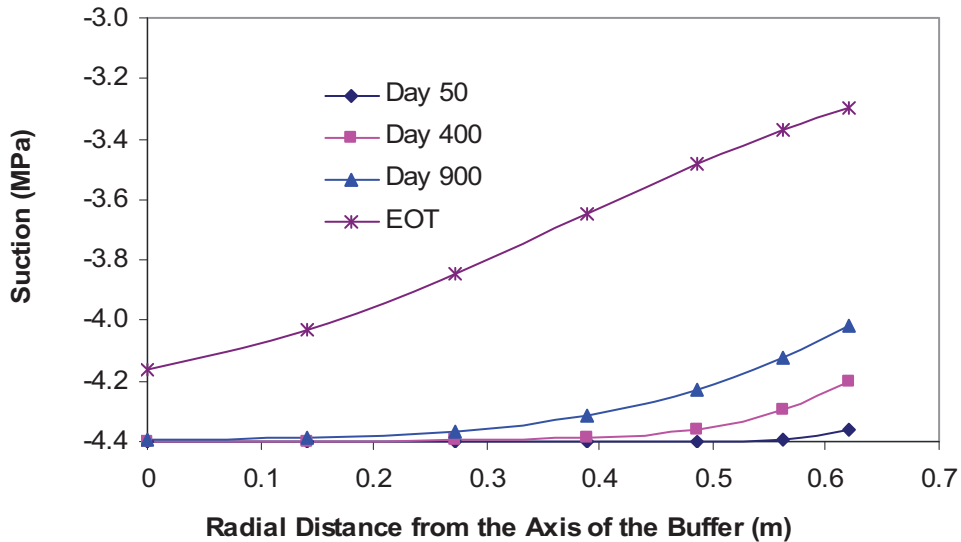


Figure 25: Suction Predictions at 1.5 m Height from the Bottom of Buffer vs. Distance from the Borehole Centreline for Different Times

Figure 26 shows the suction distributions of the buffer in the vertical cross section through the axis of the buffer within the placement borehole. Figure 27 shows the measured water content distribution in the vertical cross section through the axis of the buffer in the ITT at the end of the test. As water content and suction are directly related by the retention formulae (Figure 12), the

suction predictions can be compared to physical water content measurements. The distribution pattern of moisture in the buffer from the numerical simulation resembled the measured pattern.

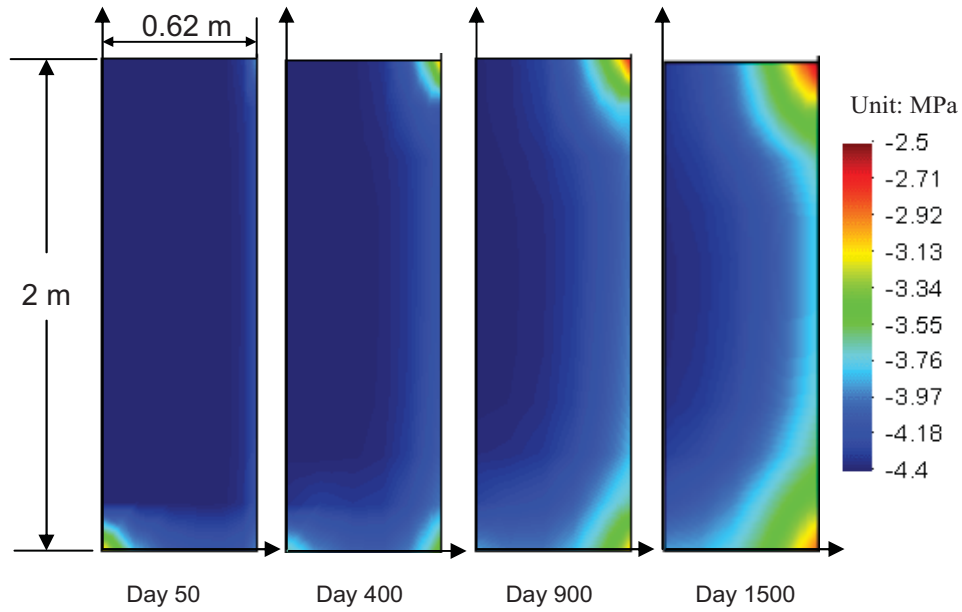


Figure 26: Transient Pore Water Pressures in the Buffer (from coupled H-M modelling)

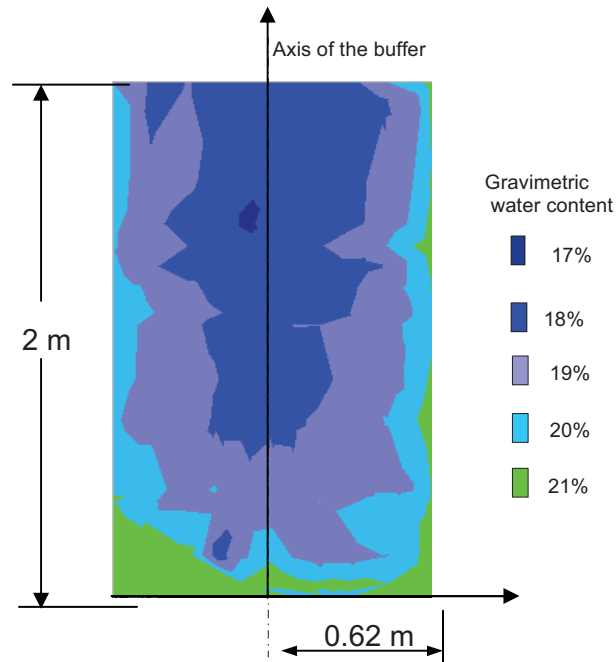


Figure 27: Measured End-Of-Test Water Distribution Vertically Through the Buffer (after Dixon and Chandler 2000)

Figures 28 to 35 show the comparison of the simulated pore water pressure for both hydraulic-only and coupled hydro-mechanical modelling to the measured data in the different layers of the buffer after decommissioning. For Layers A, B, C, D, E, F and G, the simulated data matched the measured data very well. The greatest difference between the simulated and the measured pore water pressure was present at Layer H (lower most region of the buffer) where buffer conditions were much wetter (lower suction) than predicted. The CODE_BRIGHT model underestimated the inflow of water through the base of borehole. The same discrepancy was observed for flow predictions into the empty borehole (Table 4).

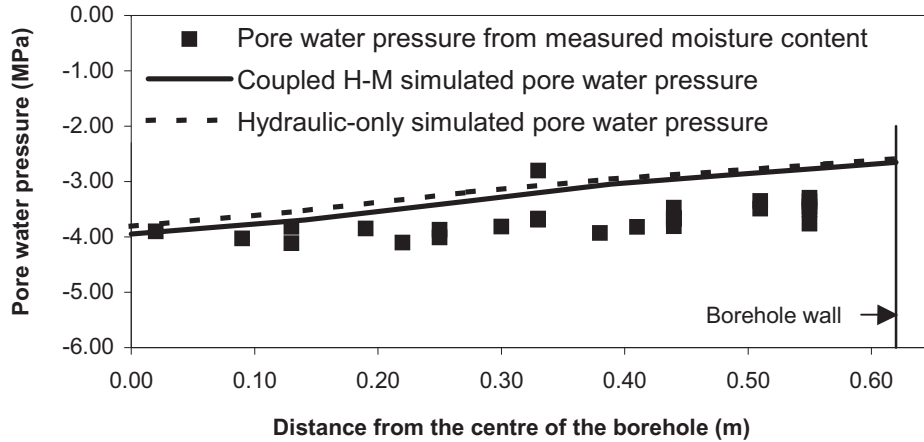


Figure 28: Pore Water Pressure Profiles in the Buffer for Layer A

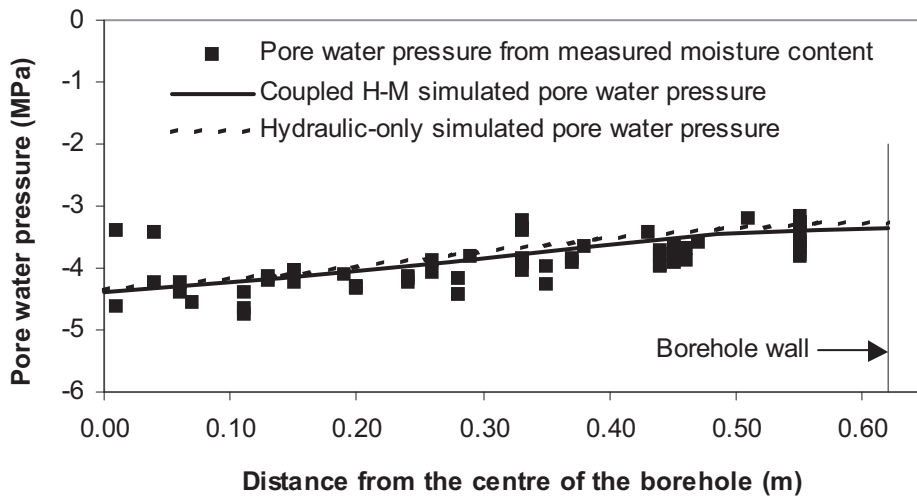


Figure 29: Pore Water Pressure Profiles in the Buffer for Layer B

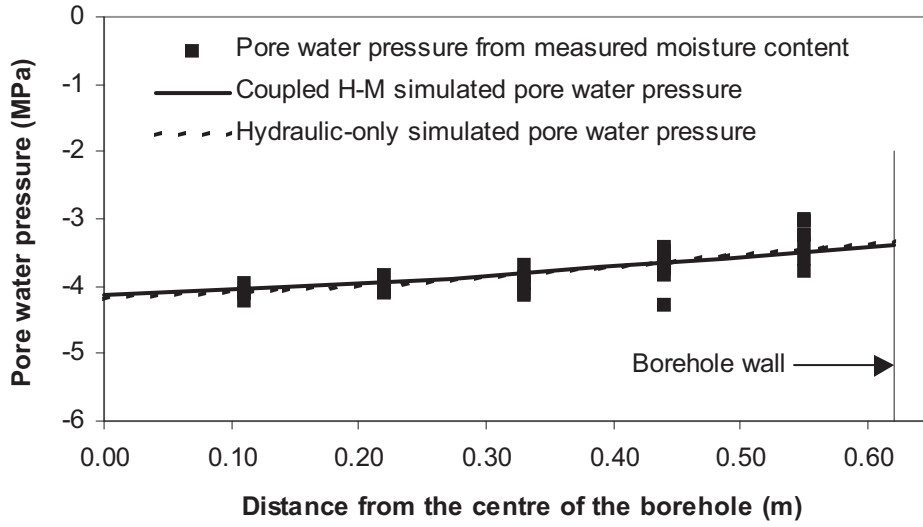


Figure 30: Pore Water Pressure Profiles in the Buffer for Layer C

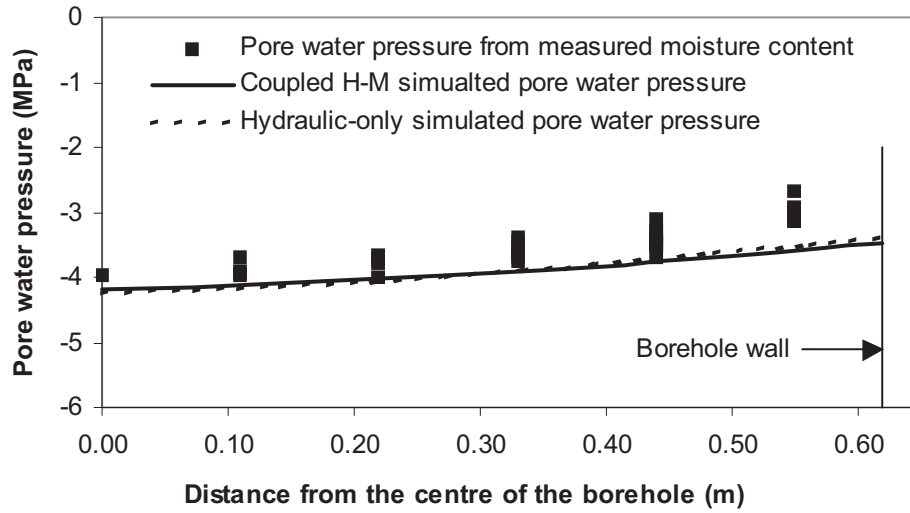


Figure 31: Pore Water Pressure Profiles in the Buffer for Layer D

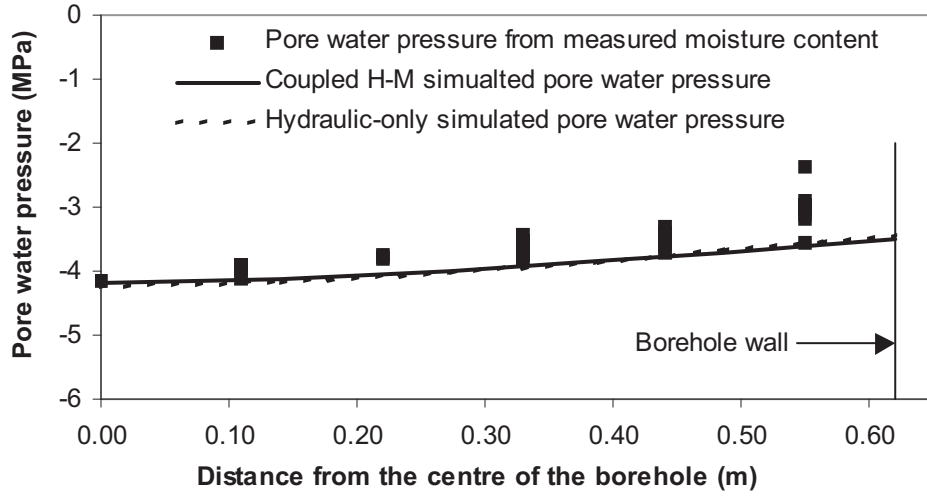


Figure 32: Pore Water Pressure Profiles in the Buffer for Layer E

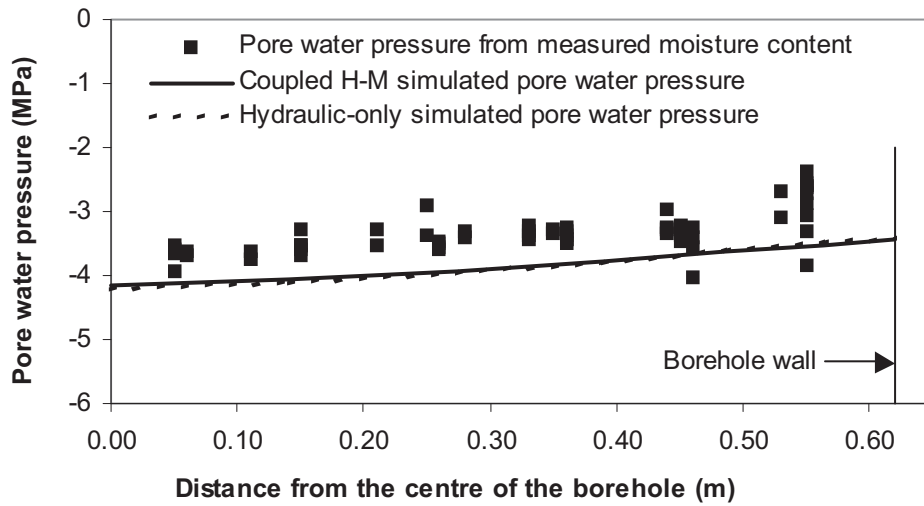


Figure 33: Pore Water Pressure Profiles in the Buffer for Layer F

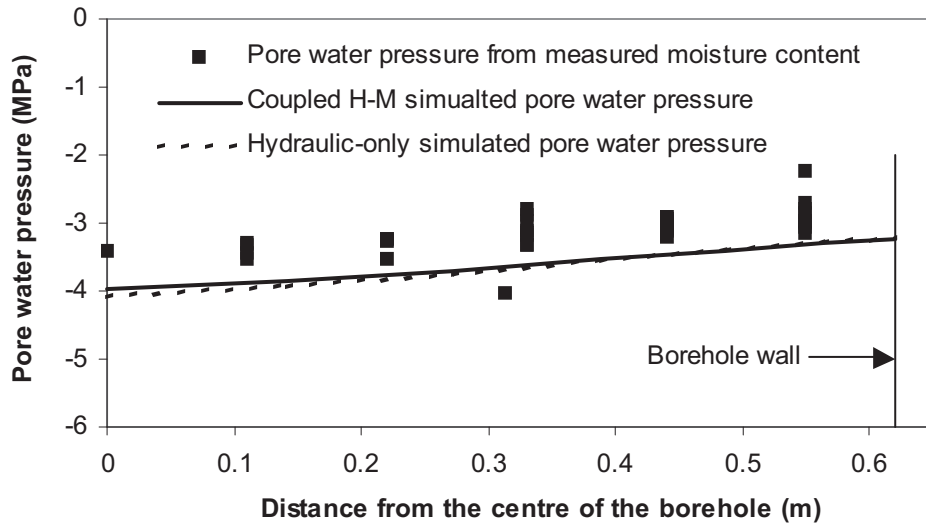


Figure 34: Pore Water Pressure Profiles in the Buffer for Layer G

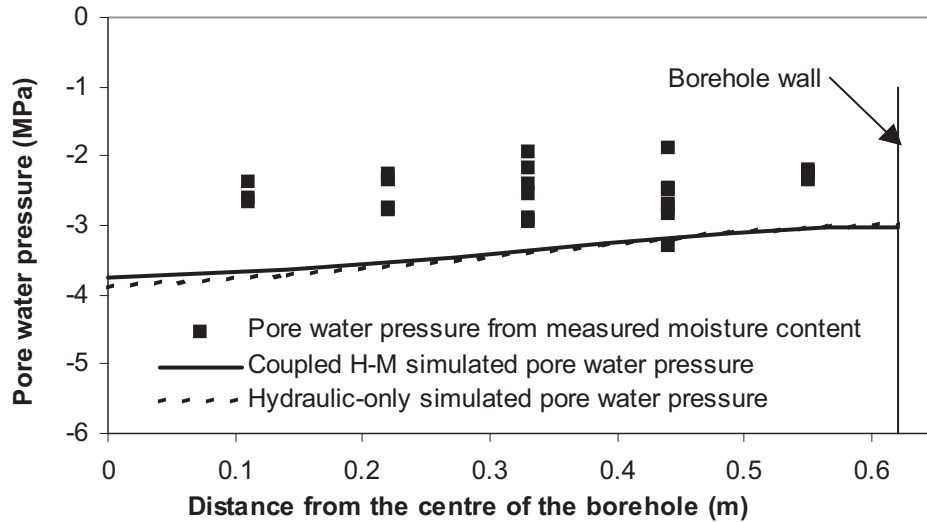


Figure 35: Pore Water Pressure Profiles in the Buffer for Layer H

2.4.5 Mechanical Response In The Buffer

2.4.5.1 Earth Pressures at the Interface between the Buffer and the Rock

The simulated radial pressures in the buffer at locations IBG1 and IBG2 are compared with the measurements as shown in Figure 36. The simulated horizontal pressures in the buffer at locations IBR1, IBR2 and IBR3 are as shown in Figure 37. Although the pattern of the

simulated results was different from the measurement, the simulated final pressures approached the measurements reasonably. Given that the simulated total pressures matched the measurements well for the Buffer/Container Experiment as will be shown in Section 3, the reason for the differences for the ITT is currently not understood.

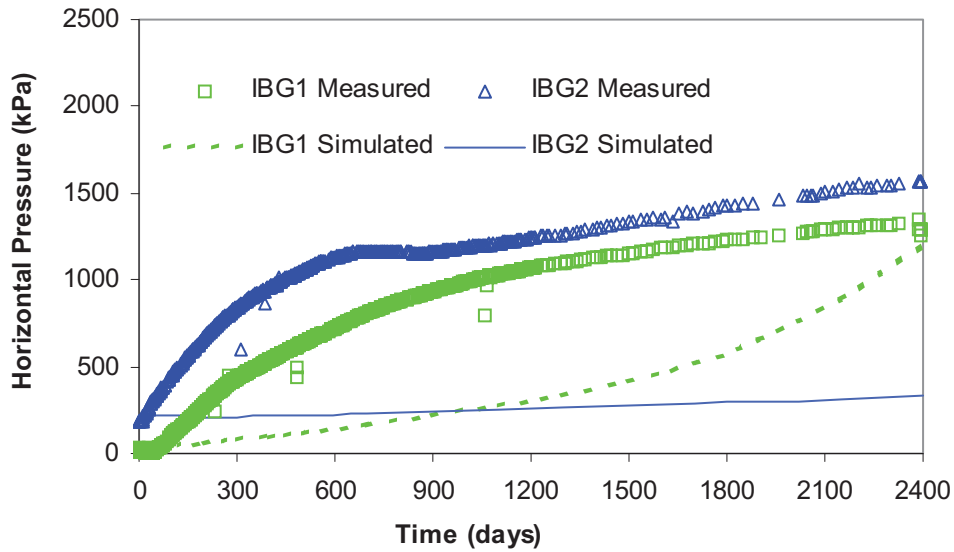


Figure 36: Radial Pressures in the Buffer at Locations of IBG1 and IBG2

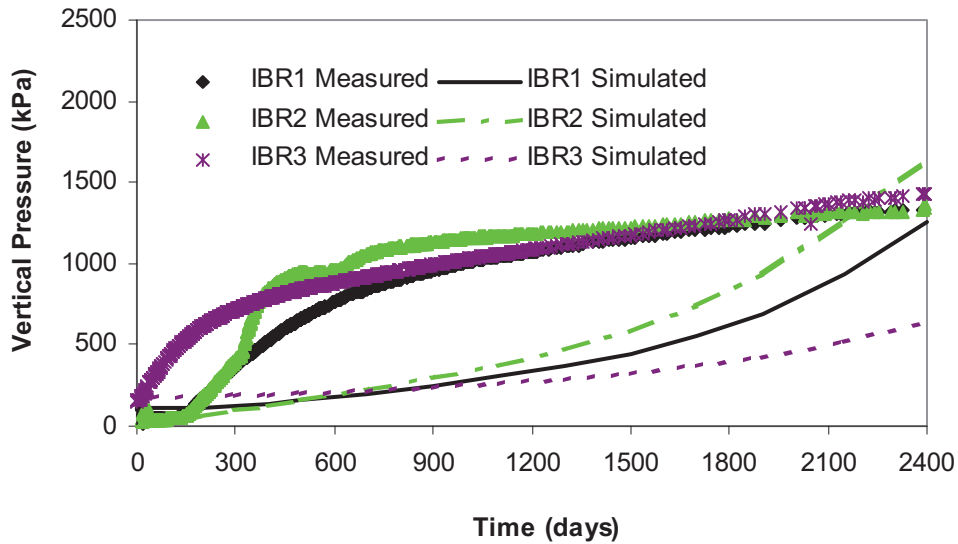


Figure 37: Vertical Pressures in the Buffer at Locations of IBR1, IBR2 and IBR3

2.4.5.2 Simulated Stresses in the Buffer

In this modelling, 200 kPa initial compaction stress (negative stress is compressive in CODE_BRIGHT) was applied into the clay/sand buffer. Figures 38 and 39 show the simulated horizontal and the vertical stresses along the mid-height of the clay/sand buffer at four different times, respectively. The horizontal compressive stress in the buffer increased with the more water it absorbed. The same phenomenon can be seen in the vertical stress.

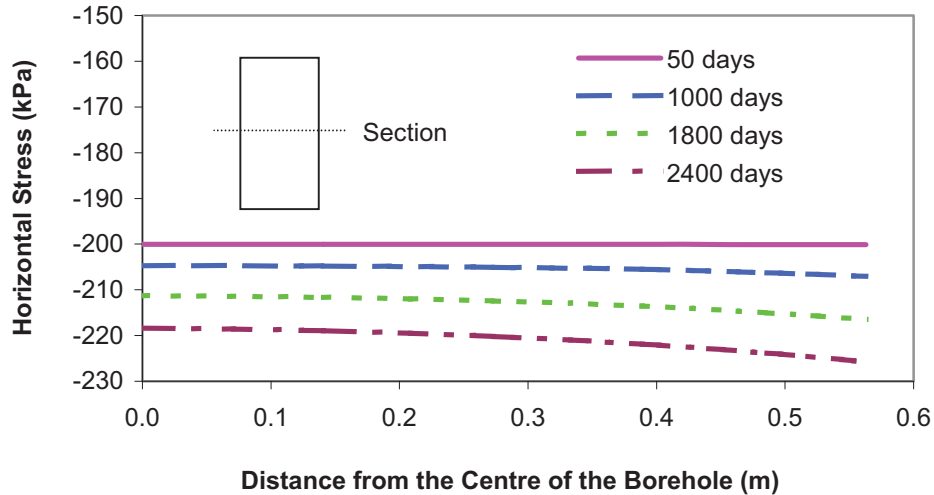


Figure 38: Simulated Horizontal Stresses in the Buffer along a Horizontal Section of the Buffer at the Mid-height (negative stress is compressive)

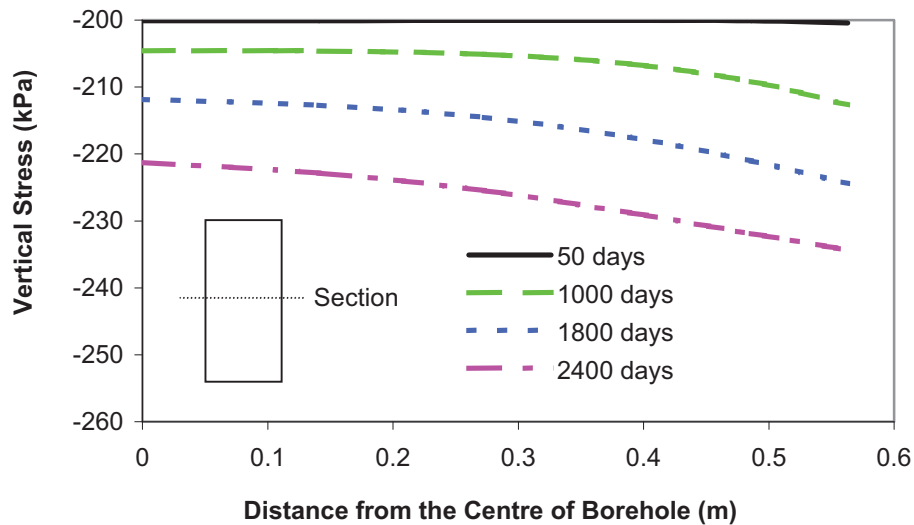


Figure 39: Simulated Vertical Stresses in the Buffer along a Horizontal Section of the Buffer at the Mid-height (negative stress is compressive)

Figures 40 and 41 show the horizontal and the vertical stresses, respectively, along a vertical line 0.39 m from the axis of the clay/sand buffer at four different times. With time, as more water was absorbed by the clay/sand buffer from the surrounding rock, the more the horizontal and the vertical stresses increased.

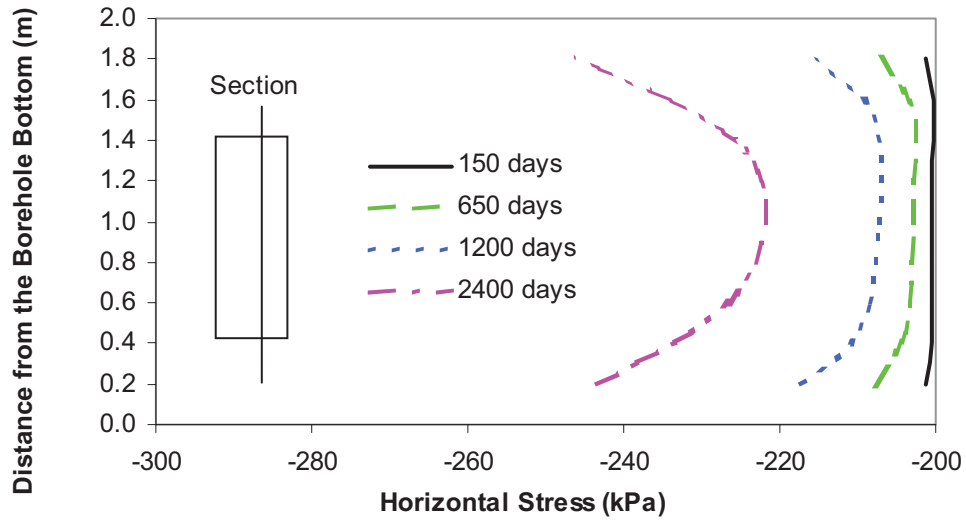


Figure 40: Simulated Horizontal Stresses in the Buffer along a Vertical Section of the Buffer 0.39 m from the Centre (negative stress is compressive)

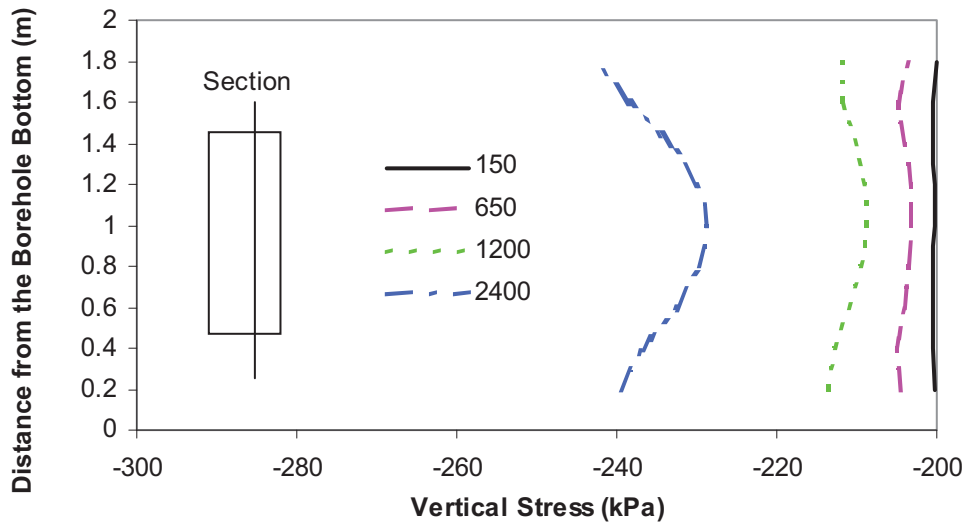


Figure 41: Simulated Vertical Stresses in the Buffer along a Vertical Section of the Buffer 0.39 m from the Centre (negative stress is compressive)

2.4.5.3 Simulated Displacements in the Buffer

Figures 42 and 43 show the horizontal and the vertical displacements, respectively, along a horizontal line through the mid-height of the clay/sand buffer at four different times. With the absorption of water from the surrounding rock, the clay/sand buffer started to expand towards the axis of the buffer. Due to the saturation of the clay/sand buffer happening quickly near the borehole bottom, the buffer at the mid-height of the test moved upwards for the first 1200 days. With time, the buffer became saturated not only at the lower part but also at the upper part, resulting in the buffer at the mid-height moving downwards.

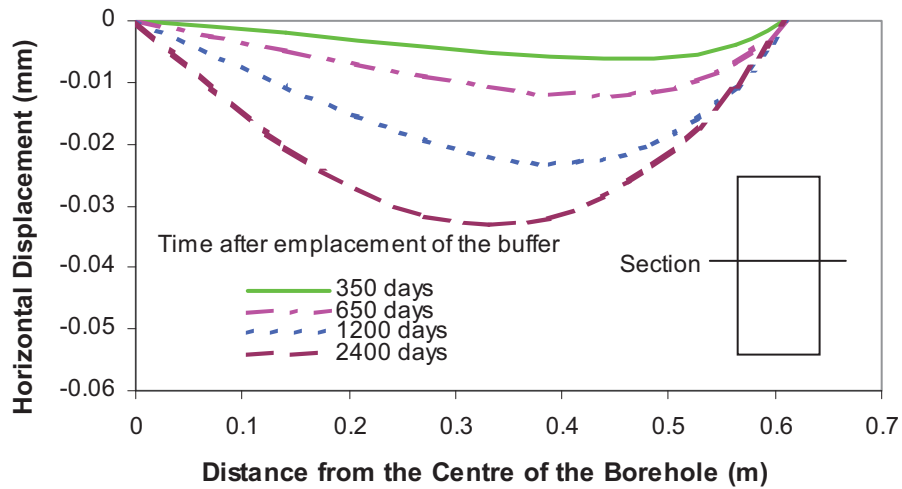


Figure 42: Simulated Horizontal Displacements in the Buffer along a Horizontal Section of the Buffer at the Mid-height (negative values in horizontal displacements means the buffer moved towards the axis of the borehole)

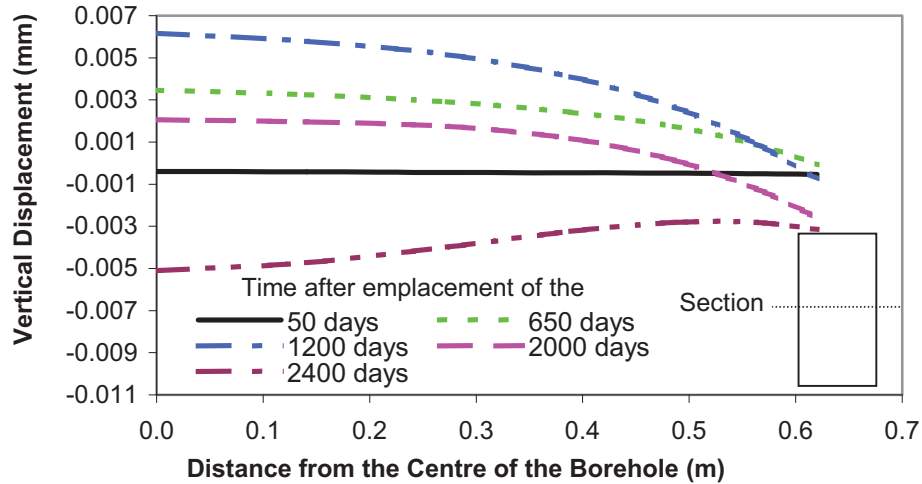


Figure 43: Simulated Vertical Displacements in the Buffer along a Horizontal Section of the Buffer at the Mid-height (negative vertical displacement means the buffer moved downwards)

Figures 44 and 45 show the horizontal and vertical displacements along a vertical line 0.39 m from the axis of the buffer. Figure 26 shows the upper and lower portions of the buffer becoming increasingly wet with time (lower suction). Considering Figure 26 together with Figure 45, it can be seen that the greater the quantity of moisture, the larger the vertical displacement.

Due to the greater stiffness of the concrete cap and the surrounding rock, the buffer expanded inwards towards the middle of the buffer as it absorbed water. Also, the vertical displacement of the buffer above the mid-height was downwards while the buffer below the mid-height moved upwards.

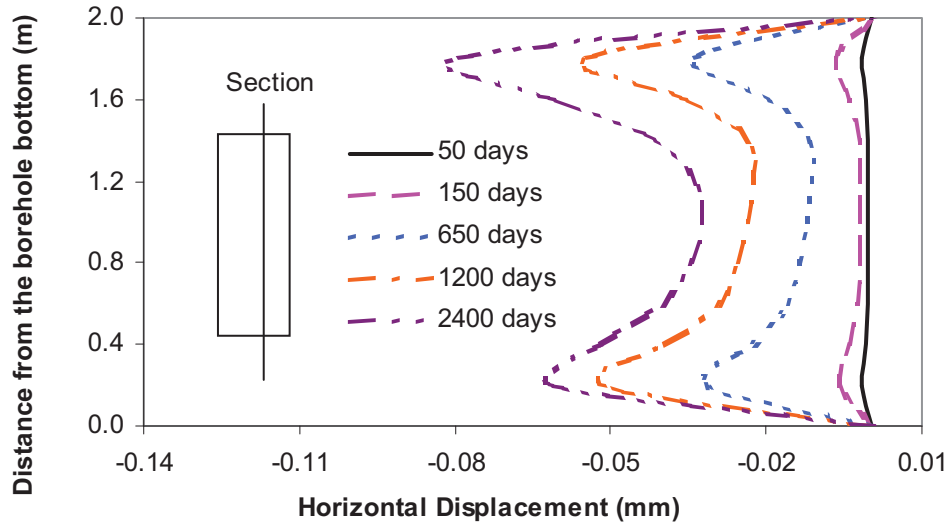


Figure 44: Simulated Horizontal Displacements in the Buffer along a Vertical Section of the Buffer 0.39 m from the Centre

The measured dry density of the buffer when it was decommissioned is shown in Figure 46. The initial dry density of the buffer was 1720 kg/m^3 . After 2350 days of hydration, the buffer absorbed some water from the surrounding rock and expanded, especially at the base of the borehole and, to a lesser extent, close to the top of the buffer. Because of the restraint from the surrounding rock and concrete cap, the buffer below mid-height displaced upwards and the buffer above mid-height displaced downwards. The buffer in the central region experienced compression and higher densities (Figure 45).

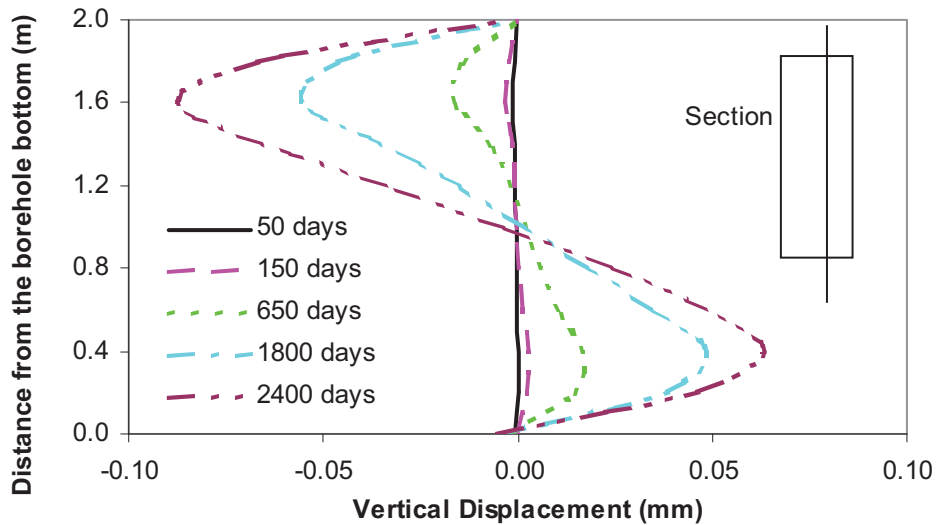


Figure 45: Simulated Vertical Displacements in the Buffer along a Vertical Section of the Buffer 0.39 m from the Centre

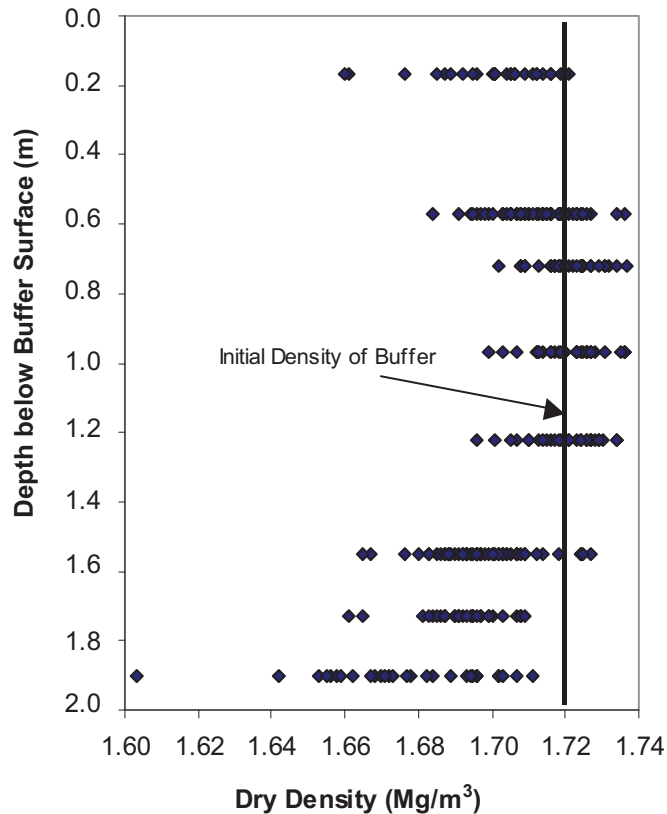


Figure 46: Measured Density Distribution in the Isothermal Test at the Time of Decommissioning

2.5 SUMMARY – ITT MODELLING

The simulated pore water pressure matched the measurements at the end of the test reasonably well for different layers except for the bottom most layer of the buffer. CODE_BRIGHT underestimated the moisture flow from the rock through the base of the borehole for both the case of an empty borehole when the borehole was filled with buffer.

The water seepage into the borehole could be calculated without considering the desaturation influence on the hydraulic conductivity of the rock when the rock surface was not sealed by sand-bentonite buffer. The modelled total water seepage using CODE_BRIGHT was 4.46×10^{-5} l/min, compared to the measured total water seepage of 4.86×10^{-5} l/min, and the simulated total water seepage of 3.48×10^{-5} l/min using FLAC and 4.23×10^{-5} l/min using COMPASS.

A series of analyses for the stage prior to placement of the buffer was carried out to understand the influence of boundary conditions and the excavation-induced damage zone on the hydraulic evolution of the rock. Back analyses of the pore water pressure in the rock indicate that there was desaturation in the rock around the borehole and Room 205. The back-analyses with

application of a pore water pressure of -360 kPa on the wall of Room 205 and the borehole can provide the best match for the pore pressure in the rock before buffer placement.

Comparison of the hydraulic pore pressures from hydraulic-only modelling to those from coupling mechanical and hydraulic components showed negligible difference because the mechanical response had little effect on water uptake by the buffer or flow through the rock.

The numerical simulation captured the characteristics of the main mechanical behaviour of the buffer. The prediction of expansion in the upper and lower portions of the buffer and compression in the central region from the simulated displacements in the buffer was consistent with the density distribution after it was decommissioned. However, the development history of the predicted vertical and horizontal pressures did not match the measurements very well. This indicates that hydraulic parameters for the buffer in the ITT need to be further refined.

3. BUFFER/CONTAINER EXPERIMENT

3.1 DESCRIPTION OF THE BUFFER/CONTAINER EXPERIMENT

The Buffer/Container Experiment was a multi-disciplinary experiment carried out at a depth of approximately 240 m below ground surface at the URL. At the 240 Level, the rock is essentially unfractured, homogeneous, grey granite in the experiment area. The geology of the 240 Level is shown in more detail in Figure 2. The experiment examined the behaviour of a bentonite-sand buffer in a realistic geologic setting under the effects of heat and the availability of water from the host rock. The experiment was designed to provide data that could be used for validating predictions of temperature, moisture movement, and mechanical behaviour from conceptual and numerical models that drew on the accompanying materials research program underway at AECL, at various universities, and at Ontario Hydro (Kjartanson and Gray 1987; Onofrei et al. 1995; Radhakrishna et al. 1992).

The Buffer/Container Experiment consisted of a series of discrete phases, each of which involved the collection of data. After the excavation of the experiment room, the experiment can be divided into six discrete phases.

- Phase A from 1990 May 15 to 1991 May 13, drilling the placement borehole and monitoring the effect that had on water pressures, temperatures and hydraulic influxes;
- Phase B from 1991 May 13 to 1991 September 13, installation of the buffer, backfill, heater and instrumentation in the borehole.
- Phase C from 1991 September 13 to 1991 November 20, a baseline monitoring period to allow temperatures, swelling and hydraulic pressures to stabilize.
- Phase D from 1991 November 20 to 1994 May 05, a heating period, with power supplied to the heater for a total of 896 days (the heater power was 1000 W for the first 26 days and thereafter the heater power was increased to 1200 W).
- Phase E from 1994 May 5 to 1994 May 13, a decommissioning phase in which the backfill, buffer, heater and instrumentation were removed from the placement borehole.
- Phase F 1994 May 13 to 1995 December, a follow-up period after the experiment during which water pressure and temperatures in the host rock continued to be monitored.

In this document, day “0” (day zero) indicates the day when power was first delivered to the heater.

The Buffer/Container Experiment was installed in a buffer mass compacted in situ in a 5-m-deep 1.24-m-diameter borehole in the floor of Room 213 at a depth of 240 m (Figure 47). A 50-mm-radial thickness of sand was installed between the electrical heater and the surrounding buffer. A 100-mm-thick layer of sand was placed below the heater body and a 300-mm-thick layer of sand was installed above the heater body prior to completion of buffer placement. A 1-m-thick layer of a well-graded, gravel-sand-clay mixture (known as backfill) was installed in the upper part of the placement borehole, above the buffer, and below the cell cap and reaction frame. The backfill consisted of 75% (by weight) of well-graded gravel aggregate and 25% glaciolacustrine clay compacted to minimum 95% modified Proctor dry density. The gravel component was small – medium gravel-size particles broken from granite excavated from the underground facility and the granite consisted of quartz, plagioclase feldspar, microcline feldspar, biotite, and chlorite in decreasing order of abundance. The clay used in the backfill was a mixture of 75% illitic clay (by dry weight) with 25% sodium bentonite from Avonlea, SK (Graham et al. 1997).

Water Inflow Measuring System:

Prior to installation of material and instrumentation in the borehole, water inflow into the placement borehole was monitored (Phase A) by installing five water collection rings, as shown in Figure 48. The first ring SR1 collected the water inflow from the concrete/rock interface and the upper 0.25 m borehole wall near the concrete. Each of the other four rings collected water inflow from a 1 m length of borehole wall.

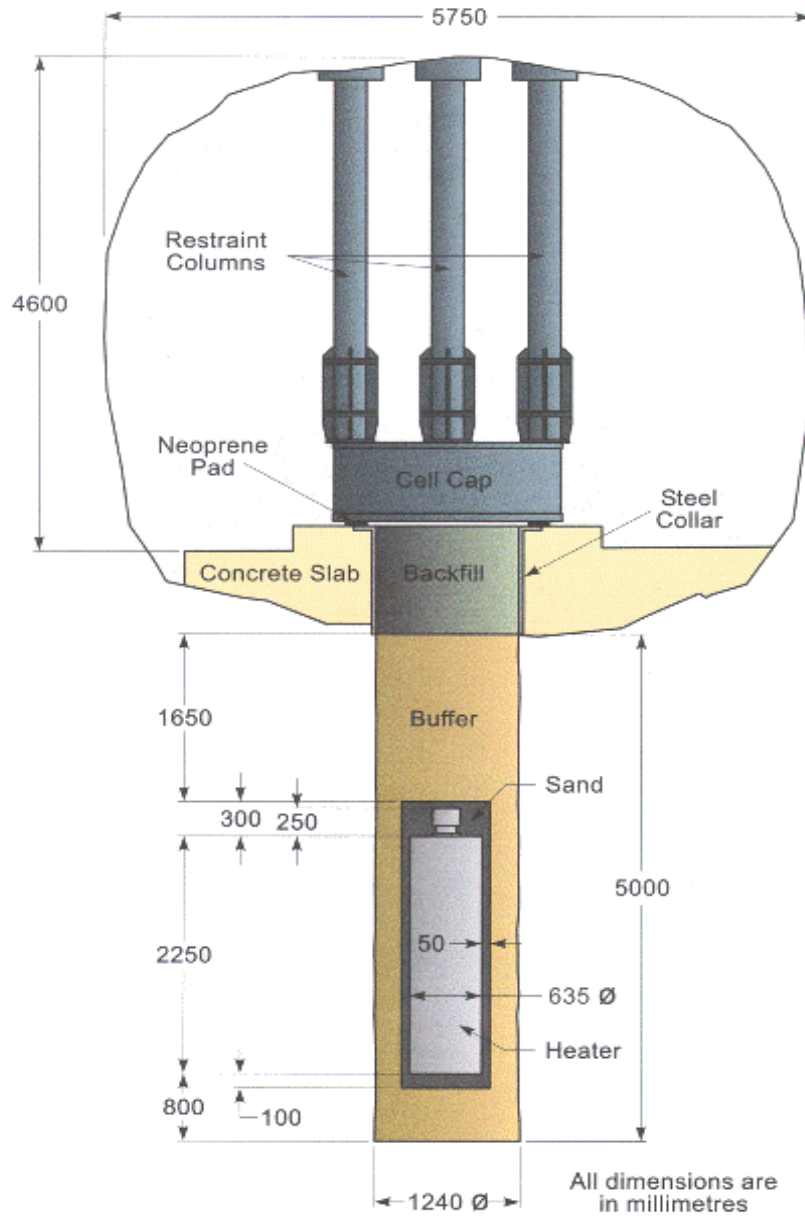


Figure 47: Construction Layout and Dimensions of AECL's Buffer/Container Experiment (after Graham et al. 1997)

Instruments for Measuring the Temperature in the Buffer and the Heater:

Thermocouples and thermistors were installed in the buffer and backfill to measure the temperature development. Figures 49 and 50 show the location of the sensors that have been selected for use in modelling of the THM evolution of the BCE. Sensors 1HT2, 1HT6, 1HT11, 1HT14 and 1HT18 were located on the surface of the heater 1.9 m, 1.5 m, 1.1 m, 0.7 m, 0.3 m from the bottom of the heater, respectively, and are not shown in Figures 49 and 50.

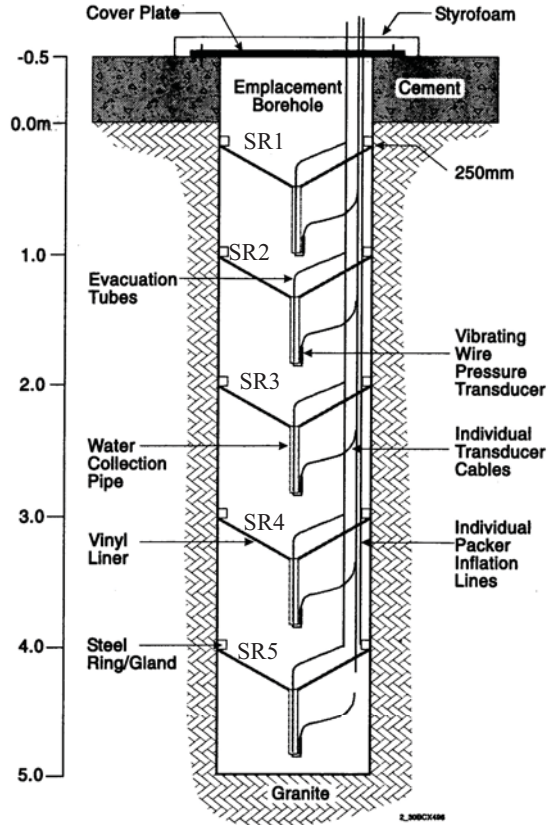


Figure 48: System for Measuring Water Inflow into Placement Borehole before Installation of Buffer (Graham et al. 1997)

Instruments for Measuring the Pore Hydraulic Pressure in the Rock:

Pore hydraulic pressures in the rock surrounding the placement borehole were monitored using vibrating wire piezometers (refer to Figure 51 for locations of 1RH1, 1RH2, 1RH3 and 1RH4) and using pressure transducers (HG) monitoring zones isolated by packers (Figures 52, 53 and 54). Boreholes HG7, HG8, HG9 and HG11 were vertical boreholes 3.5, 2.5, 1.5 and 2.206 m from the axis of the placement borehole (Figures 52, 53 and 54). HG10 was an inclined borehole with a plunge of 44.11° (Figures 52 and 53).

Instruments for Measuring the Temperature in the Rock:

Temperatures in the rock surrounding the borehole were monitored using different types of sensors (Figure 54). A series of thermistors (T) was installed in vertical boreholes T7, T8, T9, T10 and T11 to measure the temperature development in the rock (Figure 54). Three thermocouples (1RT1, 1RT2 and 1RT3) were installed in a borehole in the bottom of the placement borehole to measure the rock temperature below the placement borehole (Figure 54).

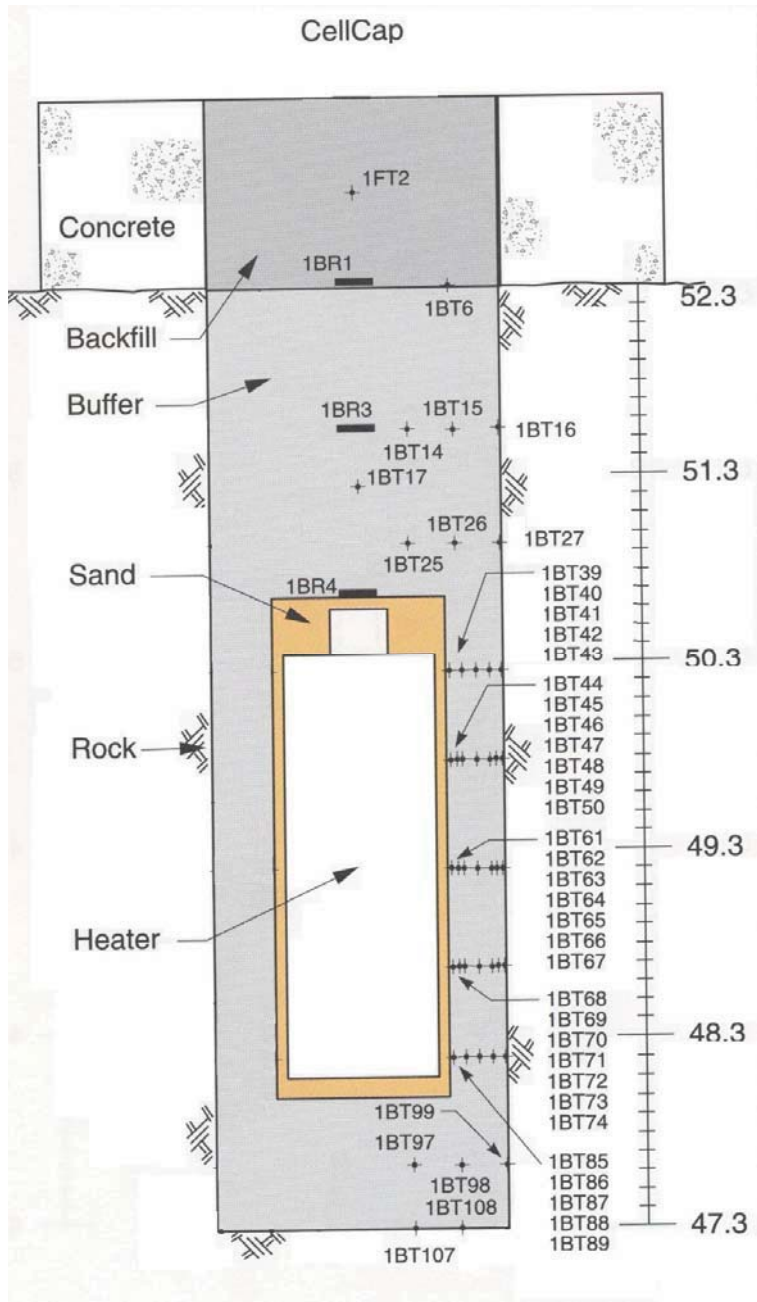


Figure 49: Section C-C through the Buffer showing Thermocouples (BT, FT), and Earth Pressure Cells (BR) (after Graham et al. 1997)

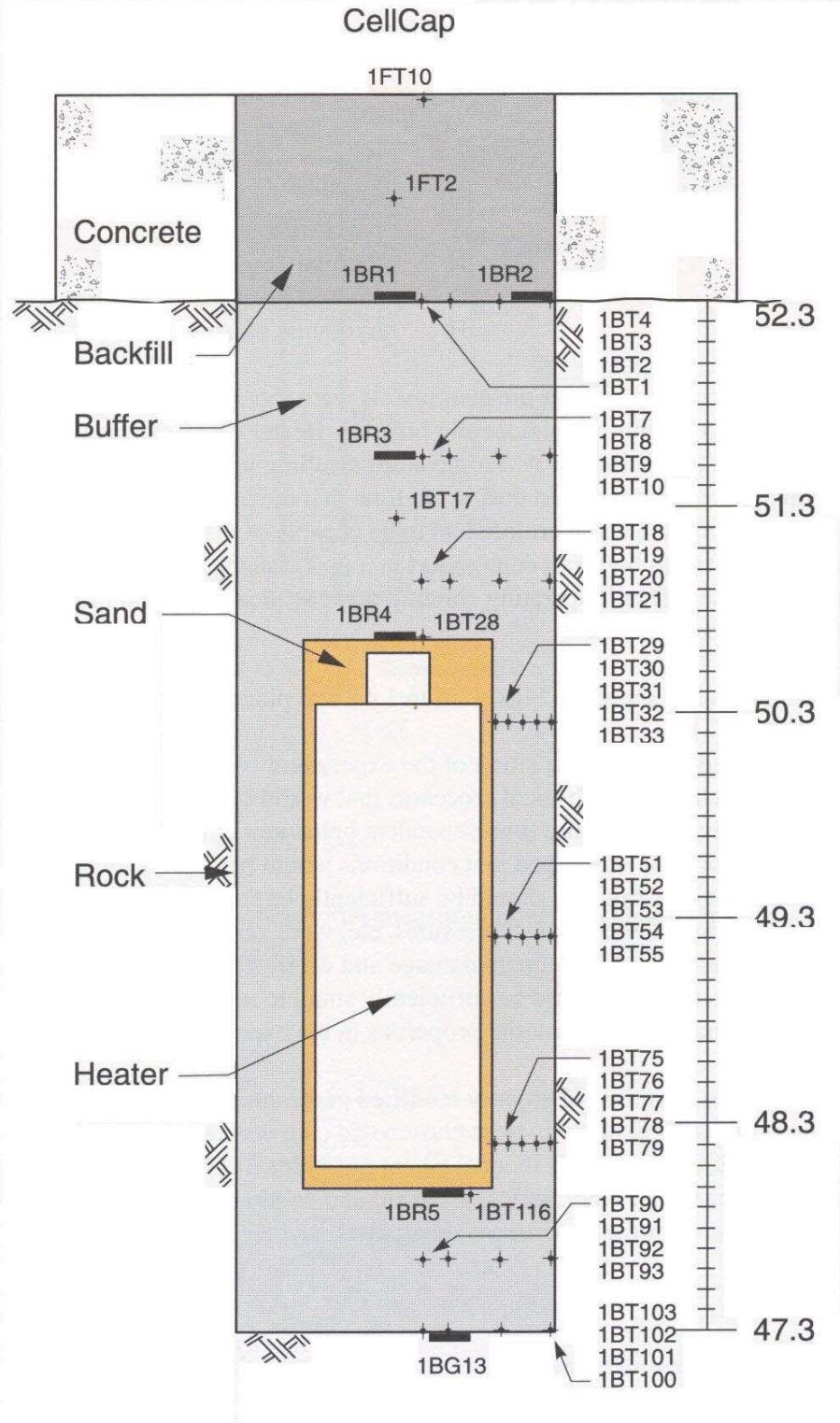


Figure 50: Section AA showing Layout of Thermocouples (BT) and some of the Total Pressure Cells (BR) (Graham et al. 1997)

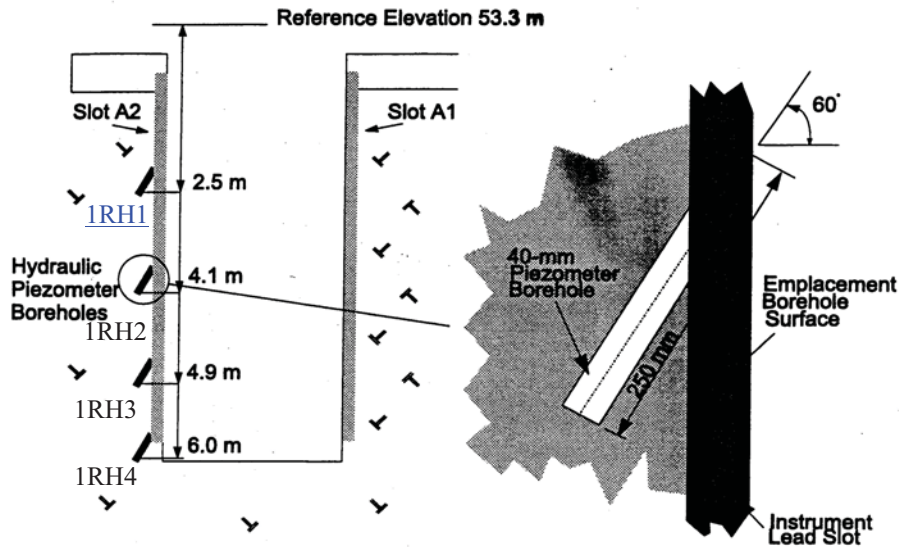


Figure 51: Installation Geometry for Hydraulic Piezometers (Chandler et al. 1998)

Measuring the Suction in the Buffer and the End-of-Test Water Content:

The suctions in the buffer were monitored using thermocouple psychrometers (BX) (Figure 55). The end-of-test water content was also determined for the samples taken from different locations (Figures 56 and 9).

Instruments for Measuring the Vertical Displacement in the Rock:

Extensometers (EXT) were installed in a vertical borehole in the rock 1.4 m from the axis of the placement borehole to measure the vertical displacements (Figure 53).

Earth Pressure Measurement:

Geonor earth pressure cells (BG) were installed in the interfaces between the buffer and the rock to measure horizontal pressures acting on the rock (Figure 57) and vertical pressure acting on the rock (Figure 50). Roctest earth pressure cells (BR) were installed in the buffer and the backfill to measure the vertical earth pressure (Figures 49 and 50).

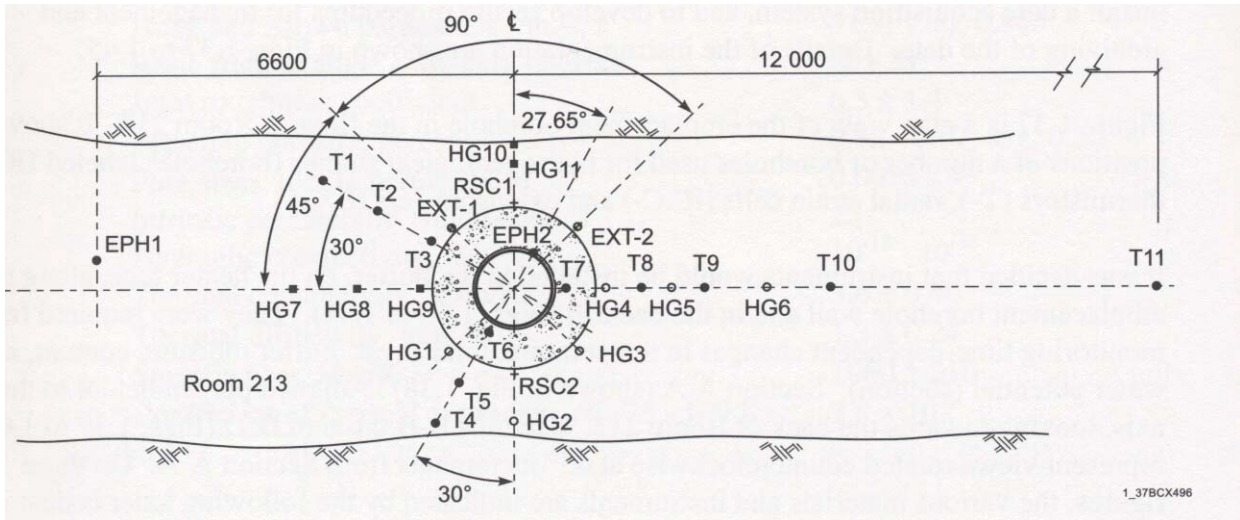


Figure 52: Plan of Instrumentation (Graham et al. 1997)

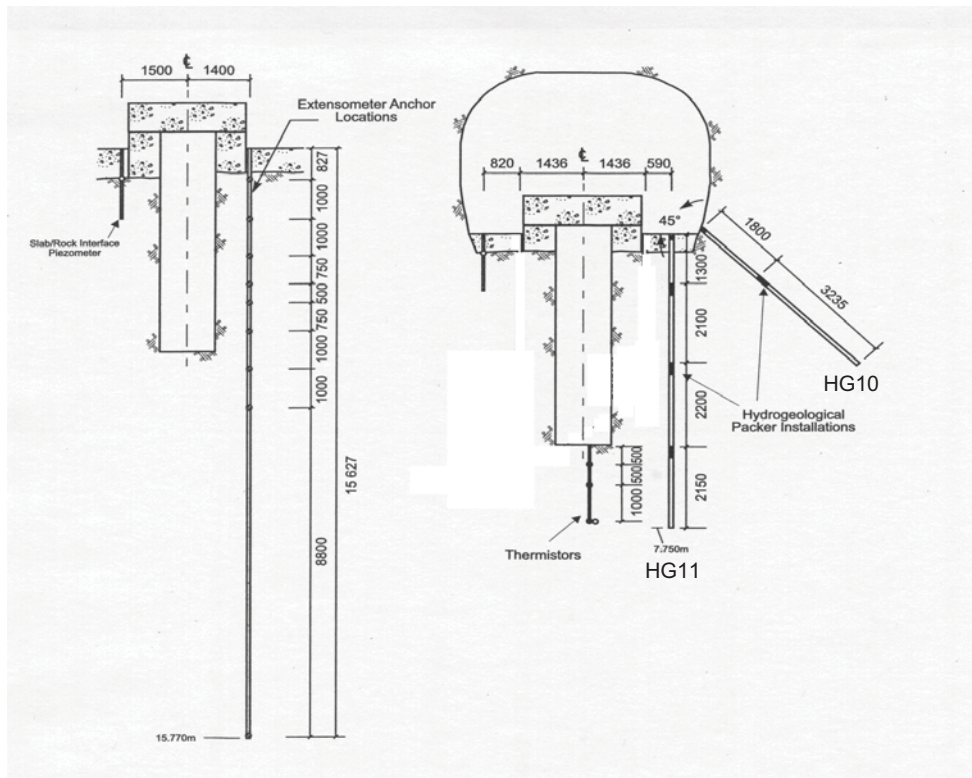


Figure 53: Transverse Section of Room 213 showing Rock Strain and Packer Instrumentation

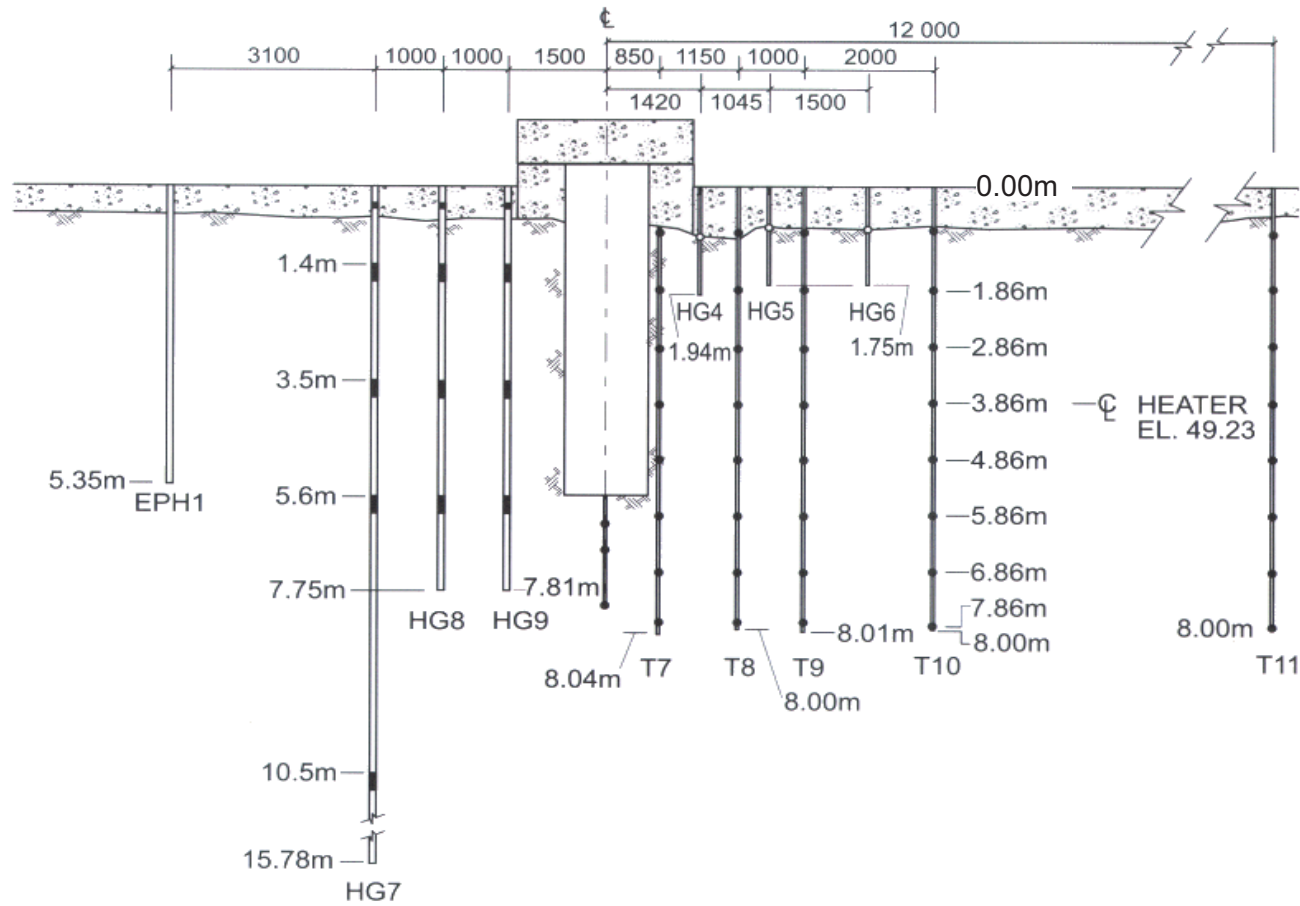


Figure 54: Longitudinal Section of Room 213 Showing Packer (HG) and Thermistor (T) Instrumentations in the Rock (after Graham et al. 1997)

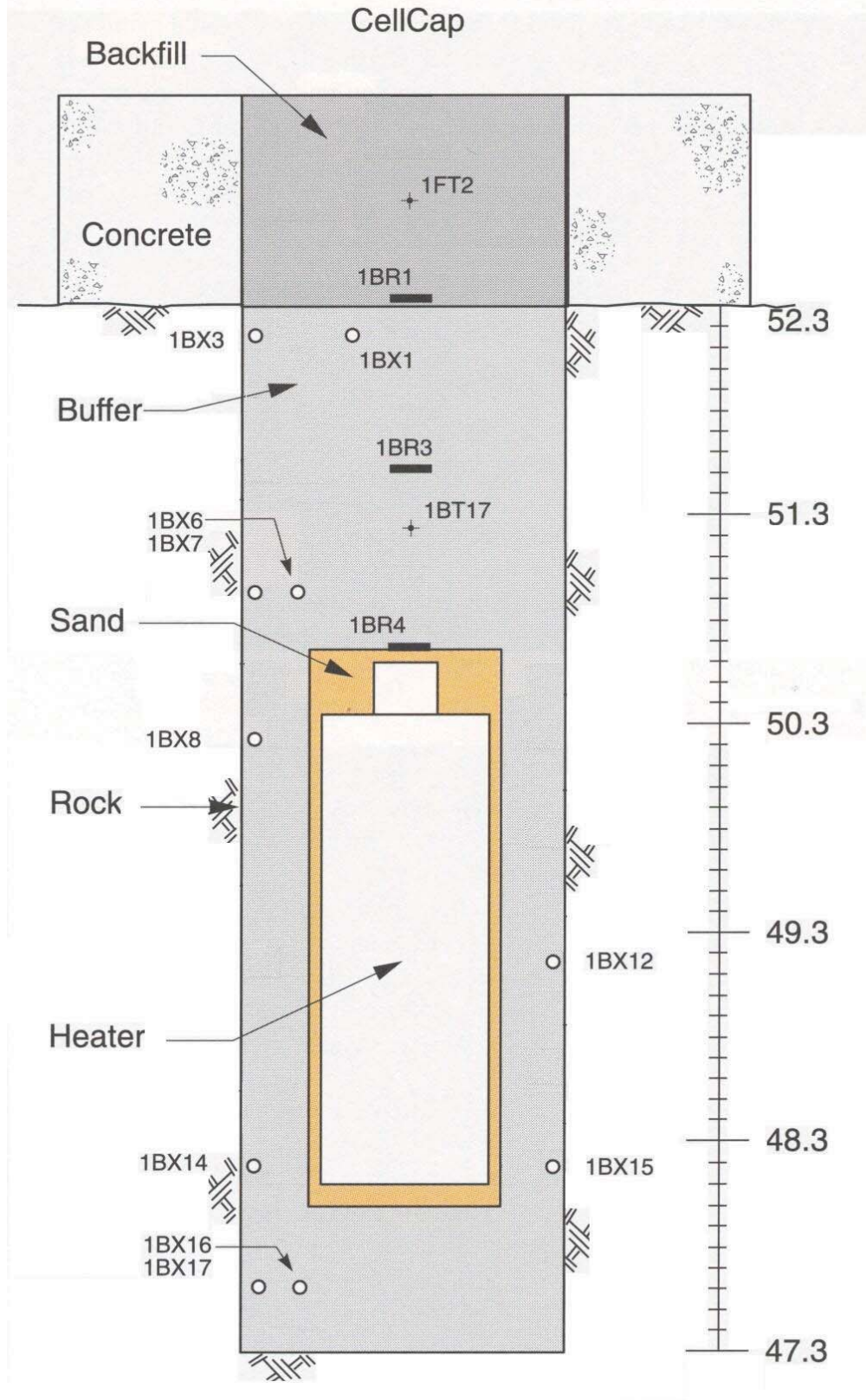


Figure 55: Section DD showing Psychrometers (BX)

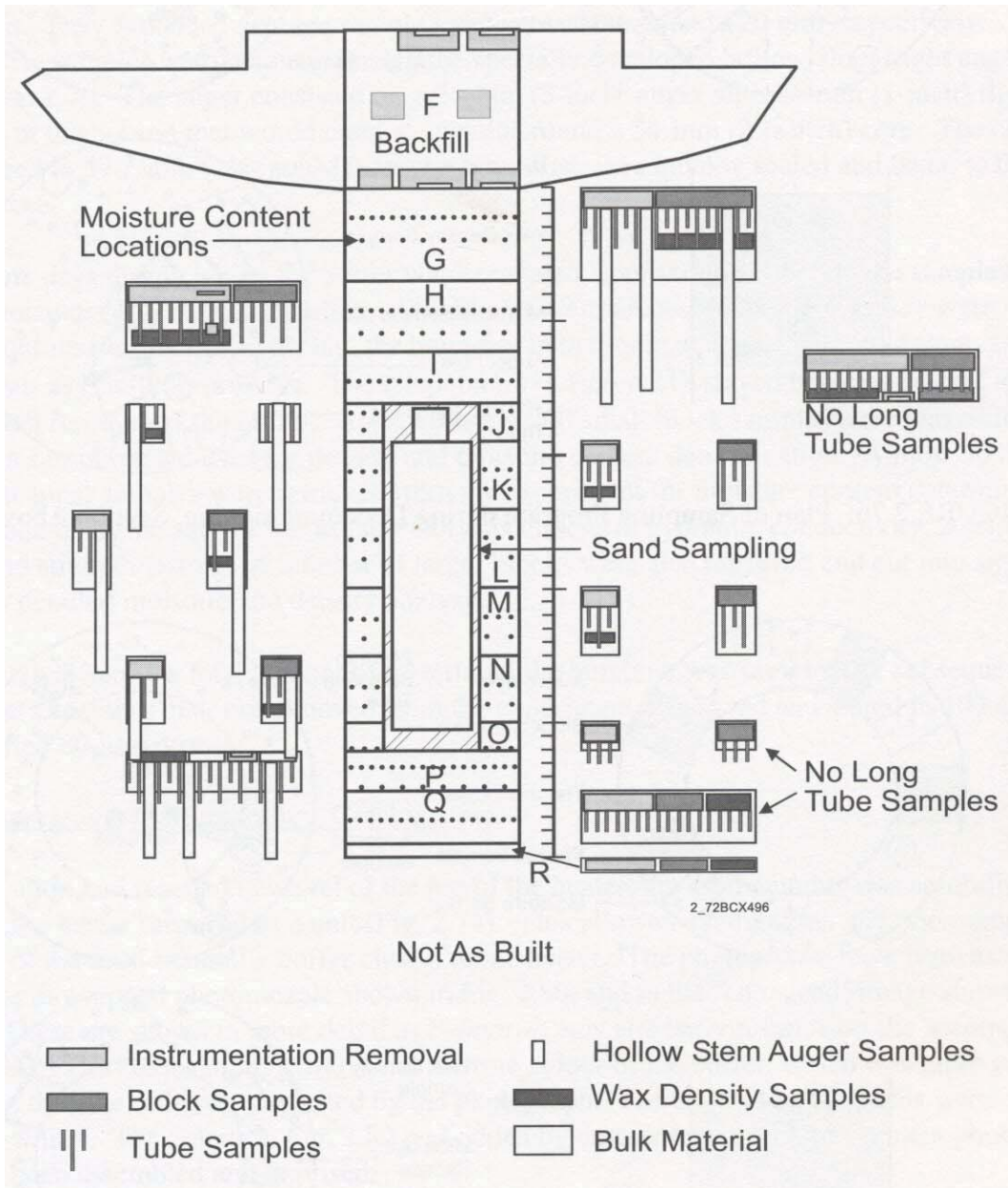


Figure 56: Vertical Section indicating Frequency and Type of Sampling Planned for Decommissioning

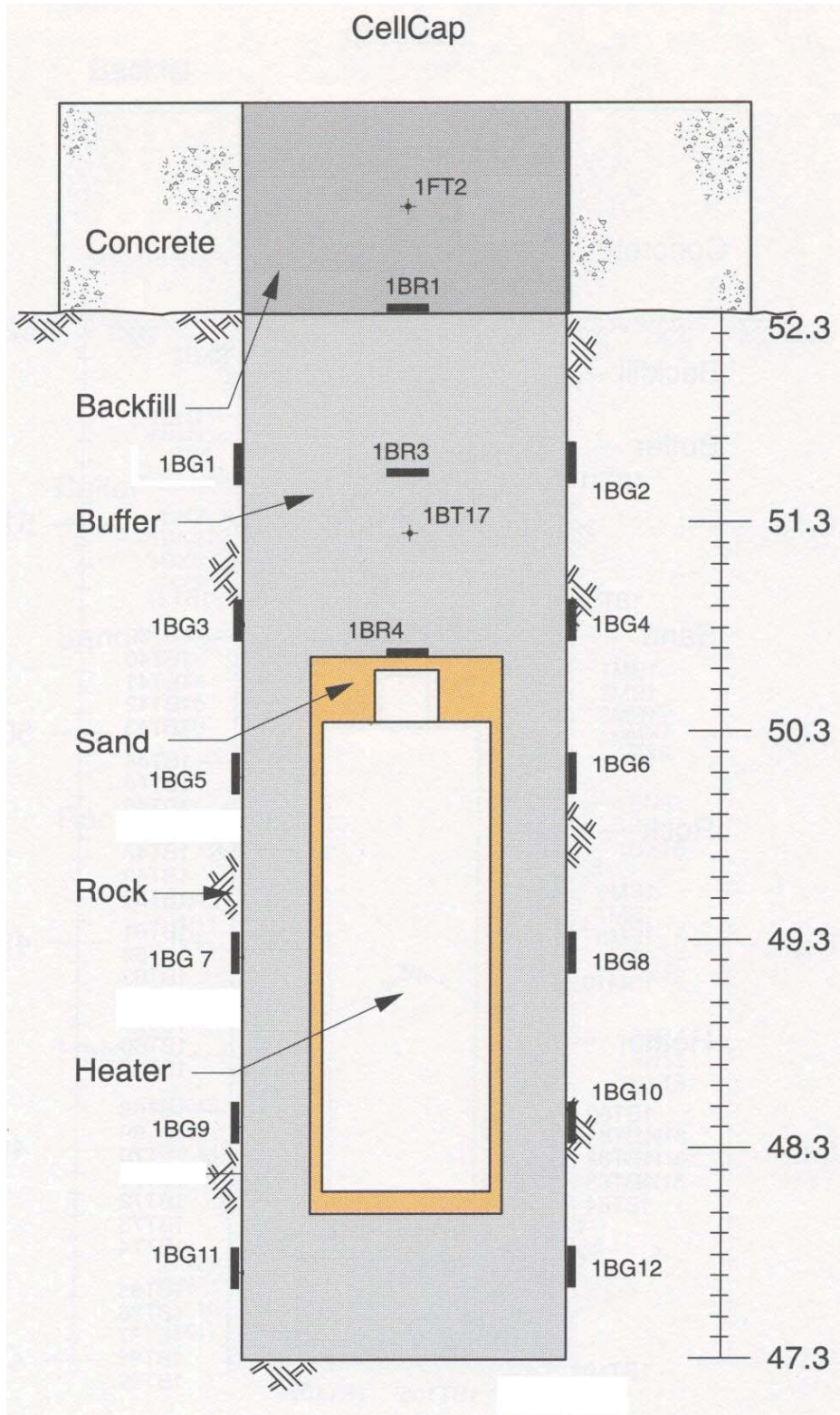


Figure 57: Section BB showing Thermocouples (BT) and Total Pressure Cells (BG, BR)

3.2 MODEL GEOMETRY, BOUNDARY CONDITIONS AND INITIAL CONDITIONS

Coupled thermo-hydro-mechanical (THM) simulations were performed using CODE_BRIGHT. The model was to simulate the 1376-day evolution of thermal, hydraulic and mechanical response of the buffer and the surrounding rock. During the first 310 days (Phase 1), the placement borehole was empty. From Day 310 to Day 480 (Phase 2), the placement borehole was filled with buffer, sand fill and backfill. From Day 480 to Day 1376 (Phase 3 or heating phase), (including 26 days with a total heater power of 1000 W and thereafter a total heater power of 1200 W) the electric heater was on.

3.2.1 Model Geometry

The two-dimensional axisymmetric model of the Buffer/Container Experiment is shown in Figure 58. The overall outside radius of the model is 16 m. The bottom of the model is 10 m from the bottom of the placement borehole and the upper boundary of the model is 10.4 m from the roof of Room 213. Since the experiment was installed in a tunnel, the axisymmetric model was not an accurate representation of the tunnel or the rock near the tunnel floor, but served as a model simplification allowing a 2-D analysis. The model provided a good representation of the experiment borehole and near-field rock as well as the far-field boundary conditions.

3.2.2 Boundary Conditions

3.2.2.1 Thermal Boundary Conditions

There was no heat flow across the top surface, the bottom surface, the radial outside surface and the axial centre line of the model during Phase 1, Phase 2 and Phase 3. The temperature on the surface of Room 213 was fixed at 16°C during all phases. The temperature on the surface of the placement borehole was fixed at 13°C during Phase 1. During heating, a certain heat flow was applied on the inside surface of sand fill to make sure that the total heat flow from the heater to the sand was 1000 W during the first 26 heating days and thereafter 1200 W. The rule of applying heat flow is that the heat flow from the heater to the sand was uniform in terms of area.

3.2.2.2 Hydraulic Boundary Conditions

The local groundwater pressure was about 1500 kPa at the 240 Level near the Buffer/Container Experiment (Chandler et al. 1992). Using this value, the hydraulic pore water pressure at the bottom of the model, the outside boundary and the top of the model was fixed at 1500 kPa during Phase 1, Phase 2 and Phase 3 modelling. There was no fluid flow across the boundary that corresponded to the axial centreline of the axisymmetric model, at the coordinate $X=0$. On the boundary representing the surface of Room 213, the pore pressure was fixed at -360 kPa using the back analyses of the pore pressure change of the rock before buffer placement of the ITT. The surface of the rock below the concrete floor of Room 213 was assumed to be connected to Room 213, therefore, the pore water pressure on the rock surface below the concrete floor of Room 213 was also fixed at -360 kPa. The pore water pressure at the nodes on the surface of the placement borehole were also fixed at -360 kPa before buffer installation (Phase 1).

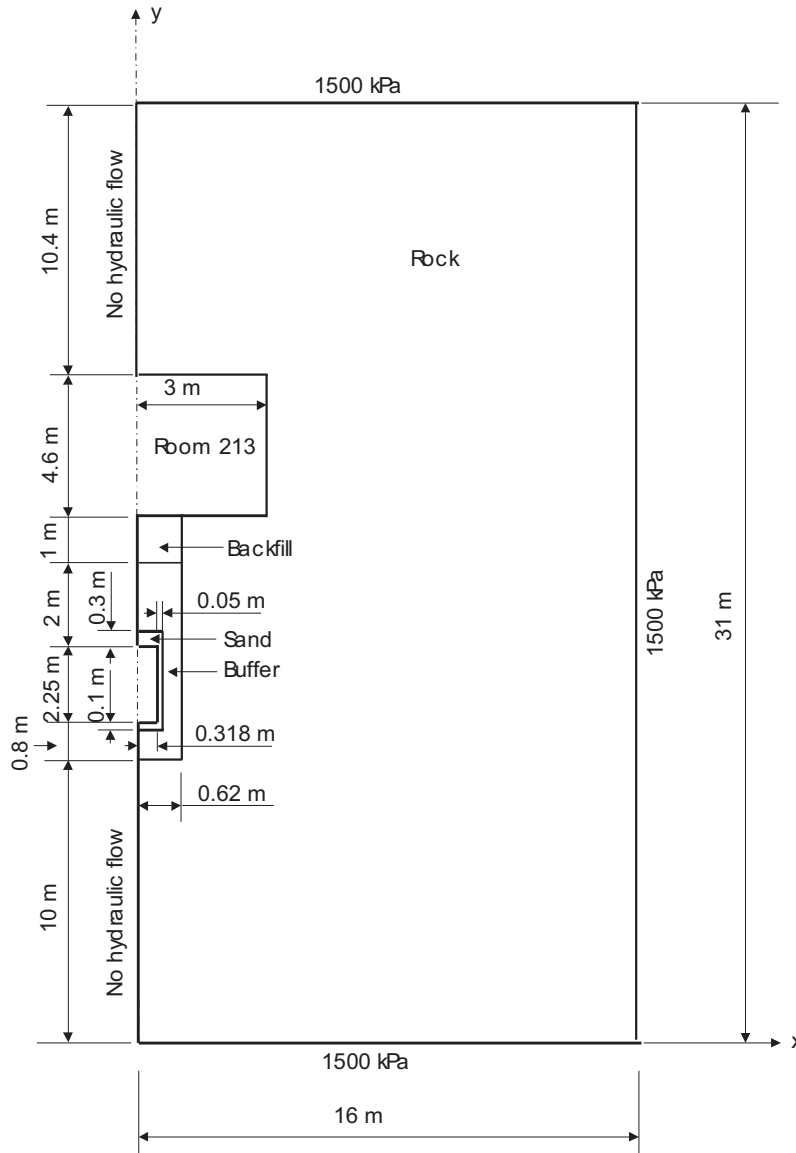


Figure 58: Dimensions of the Model Geometry and Hydraulic Boundary Conditions

3.2.2.3 Mechanical Boundary Conditions

The top boundary and the bottom boundary of the model were fixed in the vertical direction and the outside boundary of the model was fixed in the horizontal direction. The surface of Room 213 was set to have a free boundary condition. The top of the backfill was fixed in the vertical direction during Phase 2 and Phase 3.

3.2.3 Initial Conditions

The purpose of modelling Phase 1 and Phase 2 was to get the initial conditions for the modelling of Phase 3 (heating phase). Therefore, the results from Phase 1 modelling were used as the initial conditions for Phase 2 modelling and the results from Phase 2 modelling were used as the initial conditions for Phase 3 modelling.

Phase 1:

The initial temperature for the nodes of the rock was 11.5°C except for the nodes on the surface of Room 213 and the surface of the placement borehole. The temperature for the nodes on the surface of Room 213 was 16°C and the surface of the placement borehole was 13°C.

The initial pore water pressure in the rock was 1500 kPa.

The initial stresses and displacements in the model were set at 0. Although in reality there was an initial lithostatic stress in the rock, stresses calculated in the model were considered to be additive to those stresses that existed after the borehole was drilled and before the start of the experiment.

Phase 2:

The thermal results from Phase 1 modelling were used as the initial thermal conditions for Phase 2 modelling.

The pore pressure and the derived stresses from Phase 1 modelling were used as the initial hydraulic and mechanical conditions in the rock for the modelling after buffer installation. The initial pore water potential in the “as-placed” sand/clay buffer was set at -4.0 MPa. The initial pore water potential in the “as-placed” backfill was set at -4.7 MPa.

Phase 3:

The simulated thermal, hydraulic and mechanical response in the rock, buffer, backfill and the sand fill from Phase 2 was used as the initial conditions for Phase 3 modelling.

3.2.4 Discretization Of The Model

Figure 59 shows the discretization of the 2-D axisymmetric model. There were 1174 nodes and 1080 four-noded elements. The elements near the heater were set smaller than those elements farther from the heater.

3.3 MATERIAL PARAMETERS

The modelled domain consisted of four different materials: the 50:50 bentonite-sand buffer, the granite, the sand near the heater and the backfill. For the simulations described in this report, the rock and the sand near the heater were assumed to be linear poroelastic materials. The

buffer and the backfill, either unsaturated or saturated, was assumed to be a poroelastoplastic material. The concrete floor of Room 213 was taken as part of the rock.

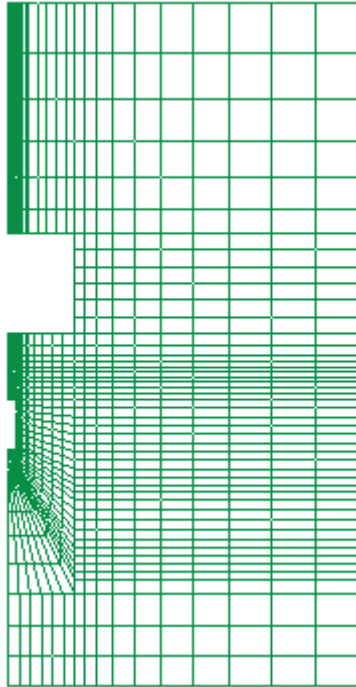


Figure 59: 2-D Axisymmetric Four-noded Finite Element Mesh

3.3.1 Bentonite-Sand Buffer Material Parameters

3.3.1.1 Thermal and Hydraulic Parameters

The hydraulic parameters are shown in Table 2.

The thermal conductivity of the buffer was a function of its saturation. In this modelling, the equation suggested by the CODE_BRIGHT manual was adopted, as follows:

$$\lambda = \lambda_{sat}^{s_r} \lambda_{dry}^{(1-s_r)} \quad (8)$$

where λ is the thermal conductivity at a certain saturation, W/(m°C);
 λ_{sat} is the thermal conductivity of the buffer when it is saturated; and
 λ_{dry} is the thermal conductivity of the buffer when it is completely dry.

The corresponding buffer properties are $\lambda_{sat} = 2.0$ W/(m°C) and $\lambda_{dry} = 0.7$ W/(m°C).

The linear thermal expansion coefficient for the solid component of the buffer was $1 \times 10^{-5} \text{ }^\circ\text{C}^{-1}$.

3.3.1.2 Mechanical Parameters

The mechanical parameters are discussed in Section 2.3.2.1 and are shown in Table 3.

3.3.2 Granite Material Parameters

3.3.2.1 Thermal and Hydraulic Parameters

The hydraulic parameters are discussed in Section 2.3.2.2 and are shown in Table 2.

The thermal conductivity of the granite is $3.0 \text{ W/(m}^\circ\text{C)}$. The linear thermal expansion coefficient for the granite is $3.8 \times 10^{-6} \text{ }^\circ\text{C}^{-1}$ (Graham et al. 1997).

3.3.2.2 Mechanical Parameters

The granite rock was assumed to be linear elastic. The Young's modulus was set as 60 GPa and the Poisson's ratio was set at 0.22 (Graham et al. 1997) (Table 3).

3.3.3 Backfill Parameters

In the Buffer/Container Experiment, the backfill had an initial dry density of 2.13 Mg/m^3 and an initial gravimetric water content of 7.2% (Graham et al. 1997). Therefore, the initial porosity of the backfill was 0.21.

A retention curve was produced based on the porosity of the backfill and the measured data for the relationship between moisture content and suction for the unsaturated buffer material by Wan et al. (1995). The suction-saturation relationship can be fitted to equation (3) suggested by the CODE_BRIGHT manual. For the backfill, the regression parameter $P_0 = 58$ and the regression parameter $\beta_1 = 0.51$. The assumed water retention curve is shown in Figure 60.

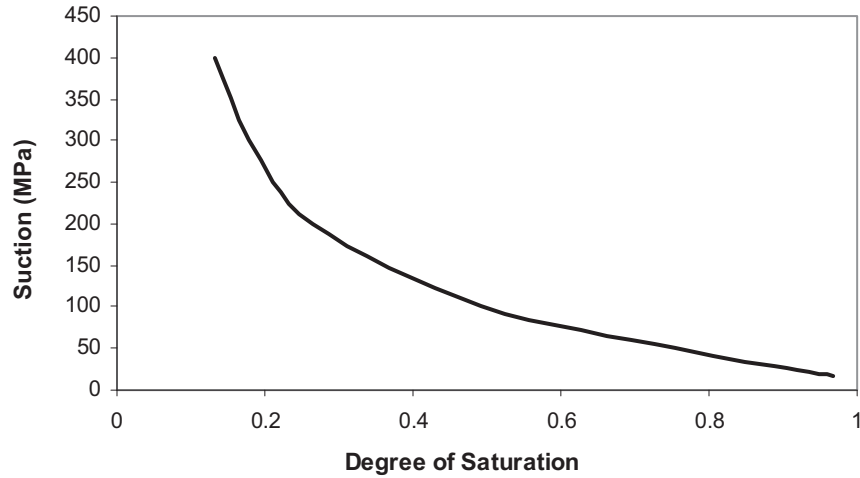


Figure 60: Water Retention Curve for the Backfill used in AECL's Buffer/Container Experiment

The unsaturated hydraulic conductivity of the backfill was also determined using the approach proposed by Green and Corey (1971) (Equation 4). β for the backfill was taken to be 0.345 and its saturated hydraulic conductivity k_0 was taken to be 1×10^{-10} m/s (Graham et al. 1997). The assumed hydraulic conductivity as a function of saturation is shown in Figure 61.

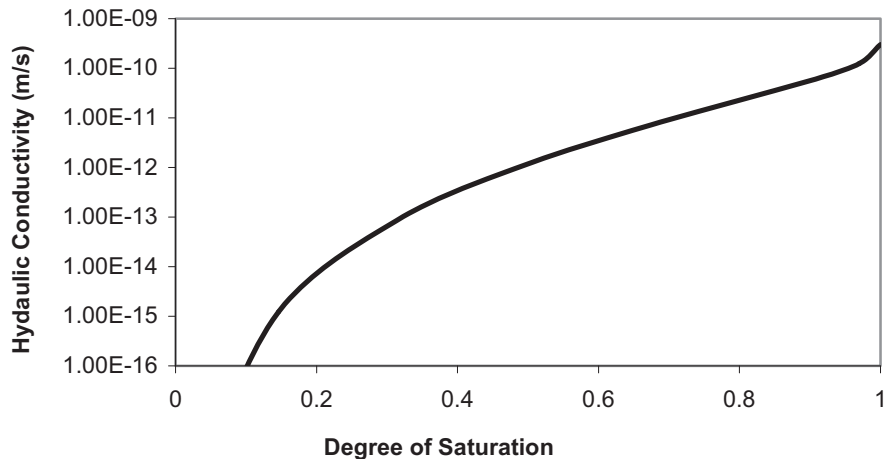


Figure 61: Relationship between the Backfill Hydraulic Conductivity and its Saturation

As there was no information available as to the mechanical behaviour of the backfill material, the mechanical material parameters used for the buffer were adopted in the analysis of the backfill (Table 3).

3.3.4 Sand Material Parameters

A 100-mm layer of dry sand was placed at the bottom of the heater. A 50-mm-thick sand annulus was placed around the heater to fill the gap left between the buffer and the heater. A 300-mm layer of sand was placed above the heater. The sand provided heat conduction to the surrounding buffer and also reduced buffer expansion due to hydration. An as-placed dry density of 1.85 Mg/m^3 was achieved by pouring dry sand into the annulus gap. The porosity of the sand was 0.302.

The thermal conductivity of the sand is a function of its saturation. The relationship of its thermal conductivity and its saturation is developed using Equation 8, suggested by the CODE_BRIGHT manual. For sand, $\lambda_{sat} = 0.8 \text{ W/(m}^\circ\text{C)}$ and $\lambda_{dry} = 0.256 \text{ W/(m}^\circ\text{C)}$.

The linear thermal expansion coefficient for sand grains is $1 \times 10^{-5} \text{ }^\circ\text{C}^{-1}$.

As there is no information about water retention curve of the sand used in the Buffer/Container Experiment, the retention curve of Garside Grade medium sand (Ewen and Thomas 1989) was used in these analyses. The suction-saturation relationship of Garside Grade medium sand was fitted to Equation 3, suggested in the CODE_BRIGHT manual.

From a regression analysis, the air entry for the sand was determined to be $P_0 = 0.003$; and β_1 was determined to be 0.85. The plot of suction versus saturation is shown in Figure 62.

The saturated hydraulic conductivity of the sand is $6.25 \times 10^{-5} \text{ m/s}$.

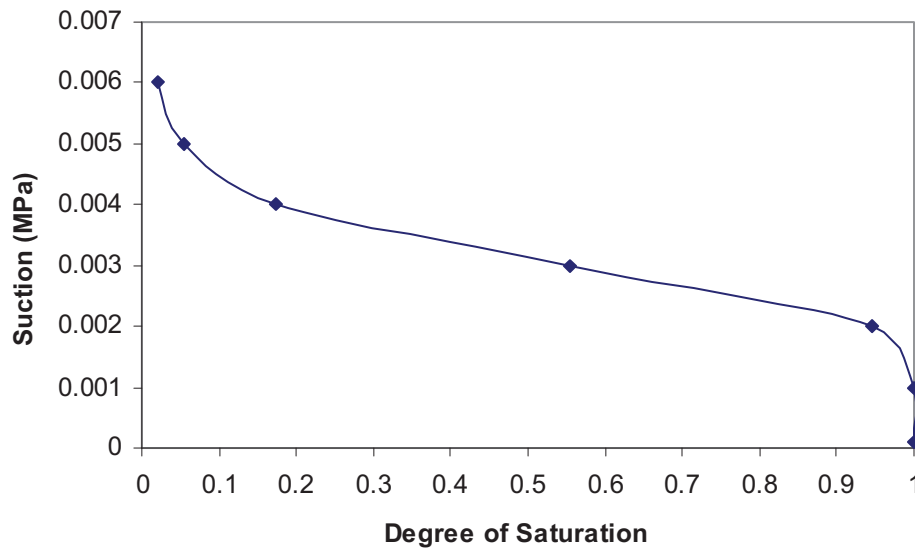


Figure 62: Retention Curve between Suction and Degree of Saturation of Sand Used in this Modelling

The mechanical behaviour of sand was assumed to be linear elastic. Its Young's modulus was set as 100 MPa and its Poisson's ratio was set as 0.22.

3.4 MODELLING RESULTS AND COMPARISON WITH MEASUREMENTS

3.4.1 Thermal Response

3.4.1.1 Temperature Changes on the Surface of the Heater

Figure 63 shows the comparison of simulated temperatures on the surface of heater and the measured data. The simulated temperatures matched the measured data very well. After one year of heating, the near-steady simulated temperature was 82.2°C, as compared with a measured temperature of 83.5°C.

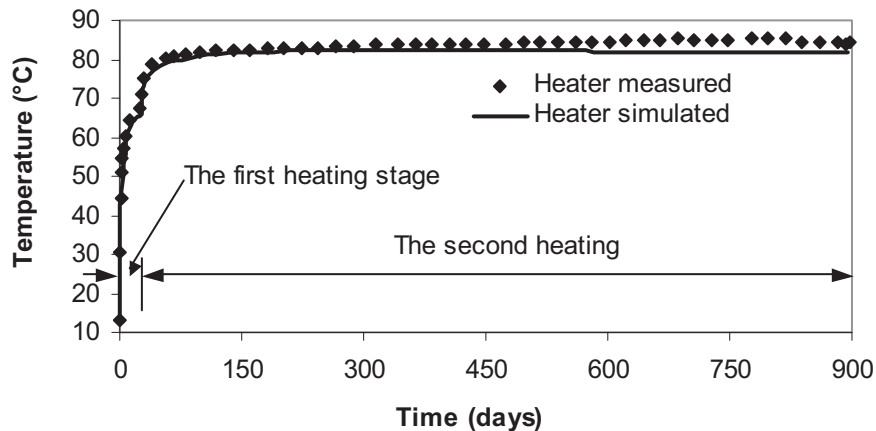


Figure 63: Simulated and Measured Temperatures of the Heater

3.4.1.2 Thermal Response in the Buffer and the Rock

Figure 64 shows the comparison of simulated and measured temperatures in the buffer at locations of instruments 1BT53, 1BT116, 1BT90 and 1BT17 (the depth from the top of the concrete collar of the placement borehole and radial distance from the axis of the placement borehole for 1BT53, 1BT116, 1BT90 and 1BT17 are (0.5 m, 4.13 m), (0.305 m, 5.35 m), (0.61 m, 5.28 m) and (0 m, 2.08 m), respectively). For locations 1BT53, 1BT116 and 1BT90, the simulated temperatures matched the measured data very well during the first 65 heating days; thereafter the simulated temperatures were 1.5°C higher than the measured data. For 1BT17, the simulated temperatures matched the measured data very well during the whole heating period.

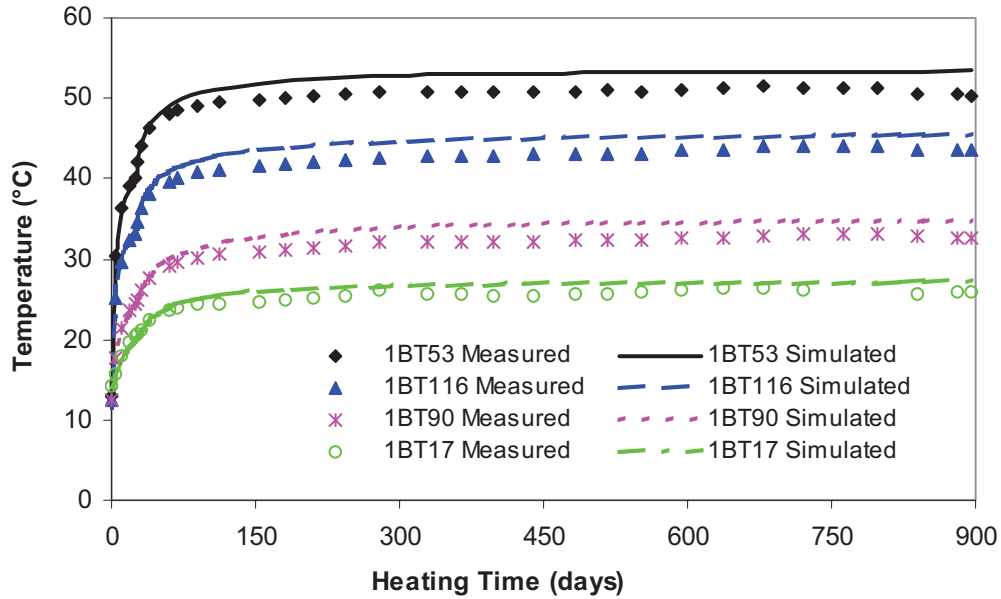


Figure 64: Comparison of Simulated and Measured Temperatures in the Buffer at Locations of Instruments 1BT53, 1BT116, 1BT90 and 1BT17

Figure 65 compares the simulated and measured temperatures in the rock at five locations T7, T8, T9, T10 and T11 along a horizontal line through the mid-height of the buffer (refer to Figures 52 and 54 for locations). For all of the above locations, the simulated temperatures matched the measured data reasonably well. It should be noted that the measured temperature at T11, 12 m from the centre of the heater, showed that almost no increase in temperature throughout the experiment. This indicated that the model radius of 16 m was large enough for the thermal simulation.

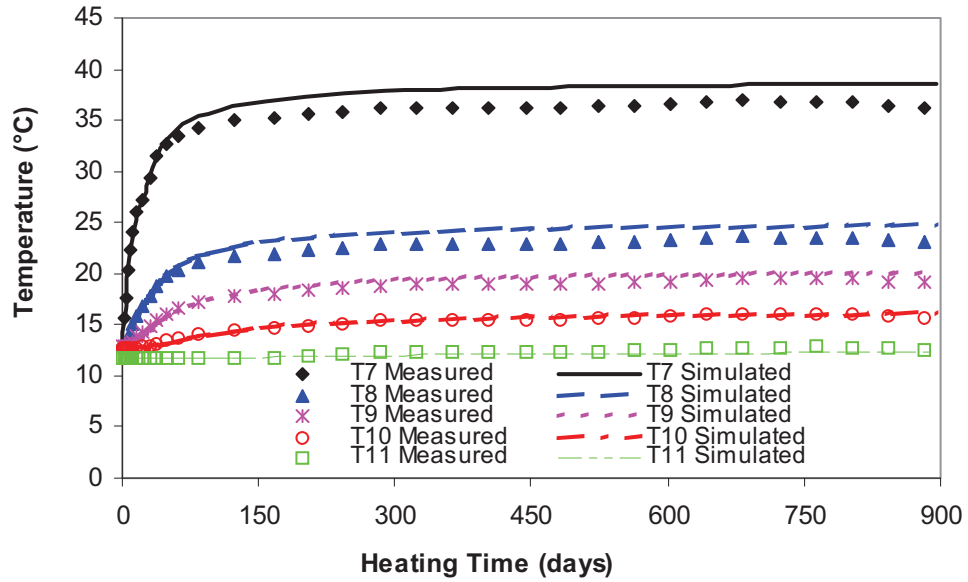


Figure 65: Comparison of Simulated and Measured Temperatures in the Rock at Four Locations along the Mid-height of the Buffer

Figure 66 compares the simulated temperatures along the mid-height of the heater at different times. For different times, the simulated temperatures matched the measured data very well except at locations near the heater.

Figure 67 shows the transient temperature profiles along the axis of the placement borehole. The temperatures through the heater itself corresponded to the skin temperature of the heater. The numerically modelled temperatures in the buffer matched the measured temperature reasonably well. At the mid-height on the surface of the heater, the simulated temperature was about 2°C lower than the measured data.

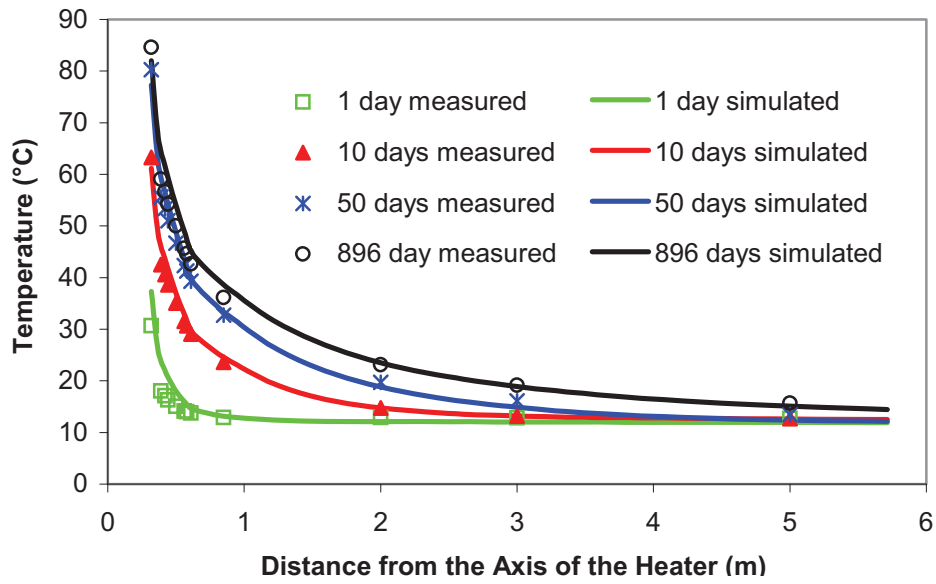


Figure 66: Simulated and Measured Transient Temperature Profiles along the Mid-Height of the Heater

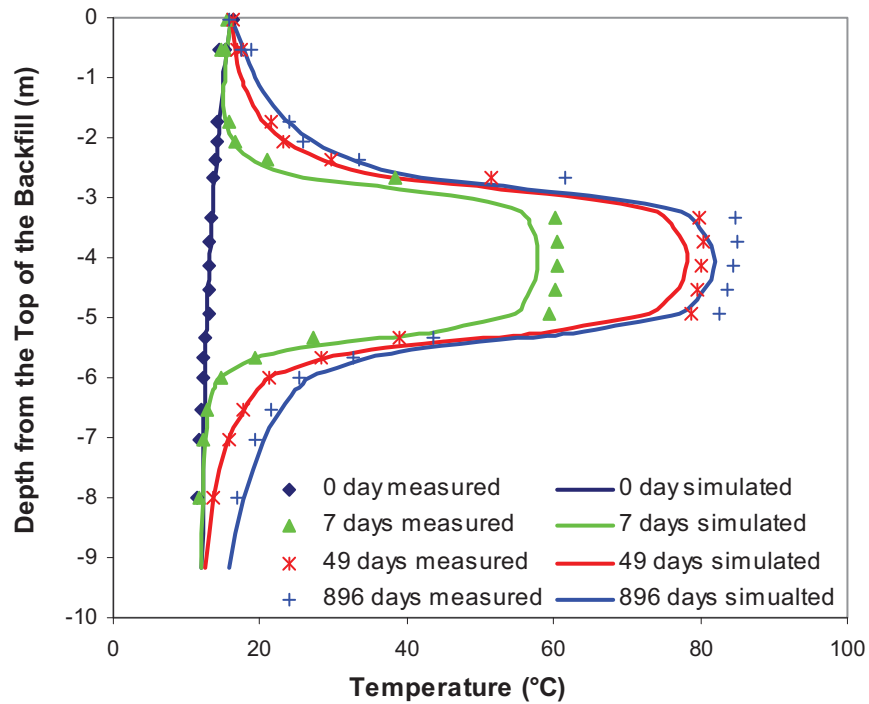


Figure 67: Simulated and Measured Temperatures through the Placement Borehole Centre

Figures 68 and 69 show the temperature development at different thermistor locations along boreholes T7 and T8, respectively (refer to Figures 52 and 54 for locations). In borehole T7, the simulated temperatures for locations with different depths matched the measured data reasonably well. For 1RM52, which was installed in borehole T7 with a depth of 4.86 m from the borehole collar, the simulated results did not match the measured data very well, with the measured temperatures lower than the predicted temperatures by as much as 1.7°C. In the numerical model the temperature on the surface of Room 213 was fixed. Actually, the temperature of Room 213 varied by about 4°C on an annual cycle. This variation was not considered in this model. In borehole T8, the simulated temperatures for different locations matched the measured data reasonably well.

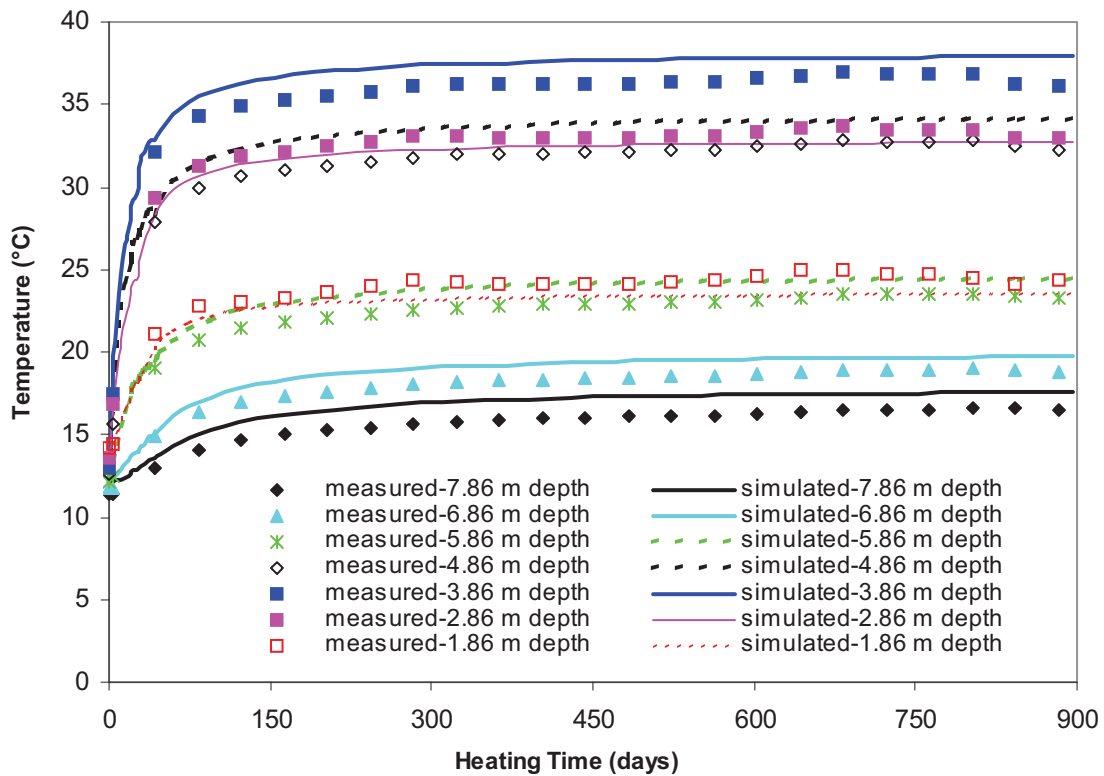


Figure 68: Temperatures at Different Depths from the Top of the Concrete Collar of Borehole T7

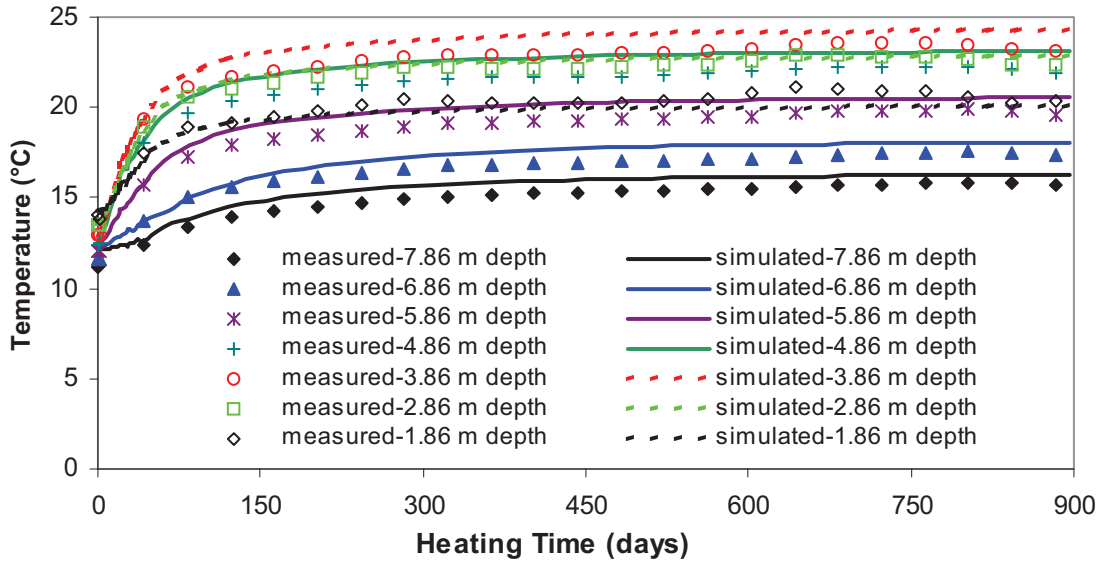


Figure 69: Temperatures at Different Depths from the Top of the Concrete Collar of Borehole T8

The simulated temperatures are compared with the measured results at four different times along boreholes T7 and T8 as shown in Figures 70 and 71, respectively. For Day 0, Day 7 and Day 49, the simulated temperatures matched the measured data very well. For Day 896, at the middle and lower part, the simulated temperatures were about 1.4°C warmer than the measured data.

The simulated contours of the temperatures in the sand and the buffer at four different times are presented in Figure 72. The temperature was highest, about 90°C, in the sand at the top of the heater. Figure 73 shows the simulated contour of the temperatures in the rock. The highest temperature of 43°C occurred at the interior surface of the placement borehole at the mid-height of the heater.

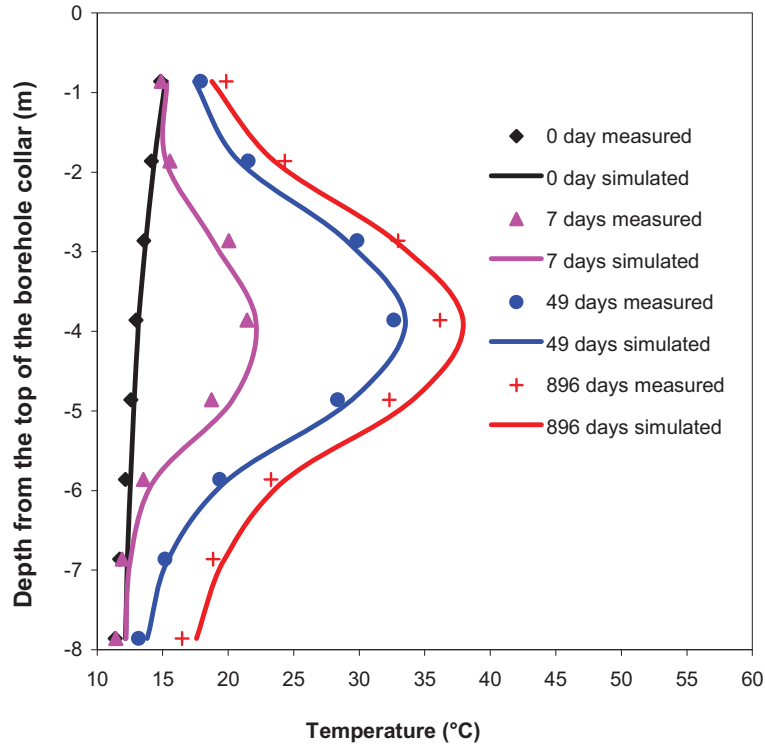


Figure 70: Temperature Distributions along Borehole T7 at Four Different Times

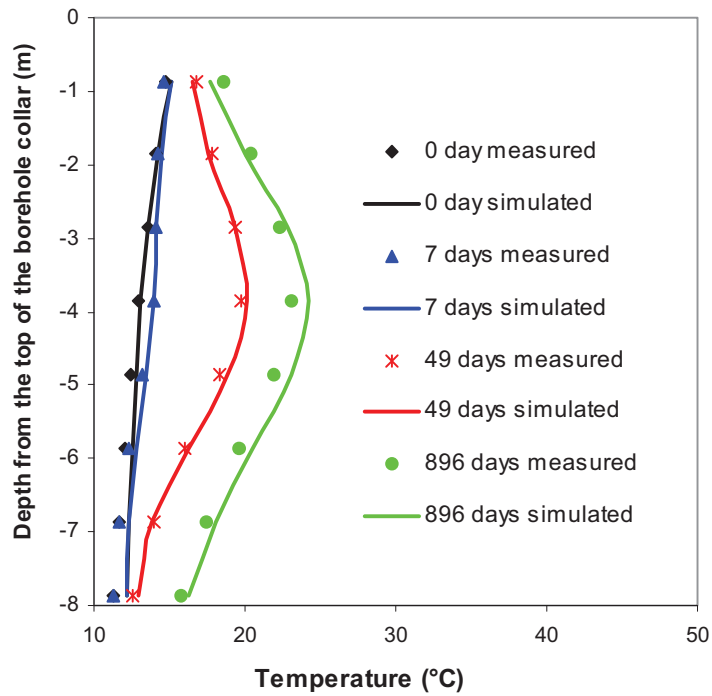
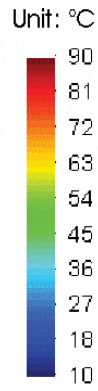
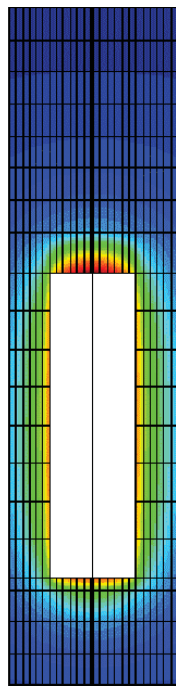
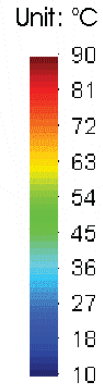
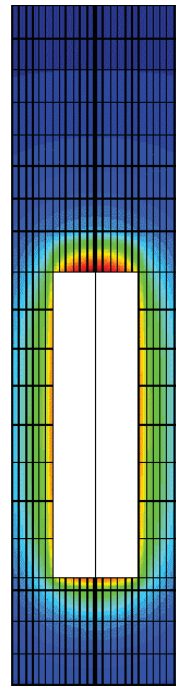


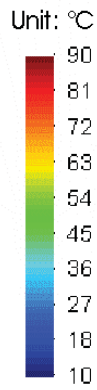
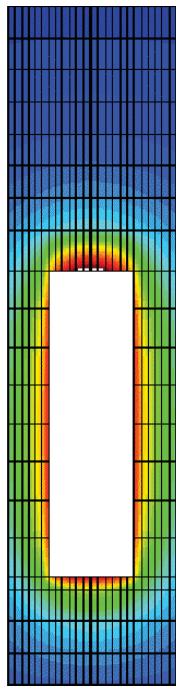
Figure 71: Temperature Distributions along Borehole T8 at Four Different Times



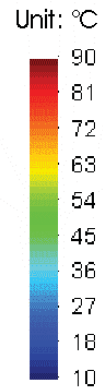
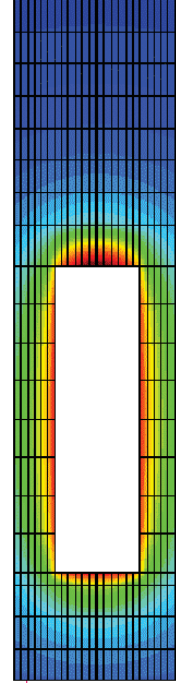
(a) 30 days after start of heating



(b) 150 days after start of heating



(c) 400 days after start of heating



(d) 896 days after start of heating

Figure 72: Temperature Contours at Four Different Times of Heating in the Buffer

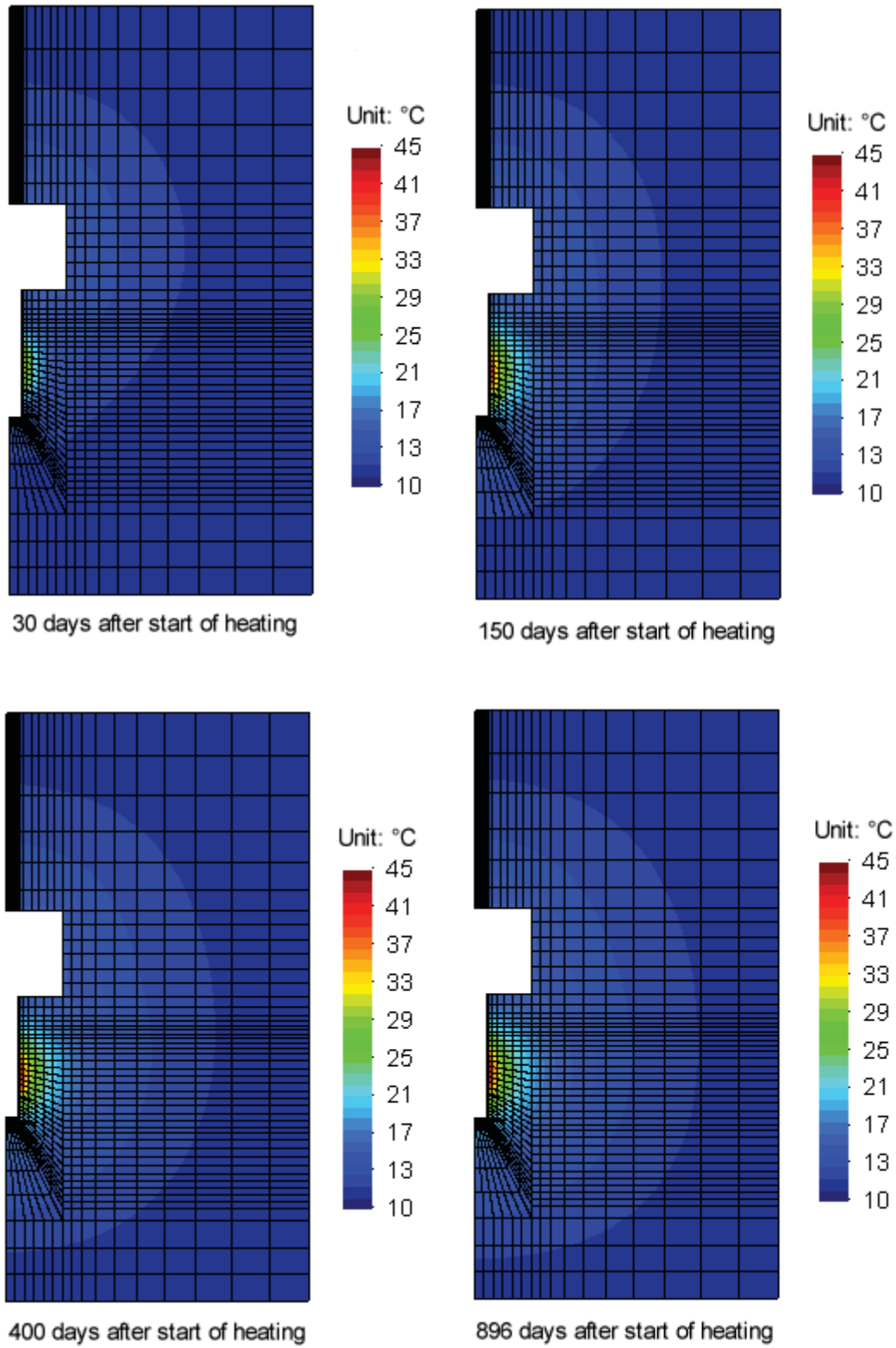


Figure 73: Temperature Contours at Four Different Times of Heating in the Rock

3.4.2 Hydraulic Response

3.4.2.1 Water Inflow into the Placement Borehole

Comparison of simulated inflows using FLAC and CODE_BRIGHT with measured inflows (see locations in Figure 48) is shown in Table 5. The numerical solution was calculated from the calculated hydraulic gradient in the rock adjacent to the borehole wall. The inflow rate was calculated by multiplying the average hydraulic gradient by the hydraulic conductivity and the area of the borehole wall covered by each layer. For Layers SR2, SR3, SR4 and SR5, the calculated inflows from using FLAC and using CODE_BRIGHT matched the measured data reasonably well. However, the measured inflow rate at Layer SR1 was about two to three orders of magnitude higher than the simulated data. Chandler et al. (1992) considered that the greater measured inflow for Layer SR1 was attributed to flow from nearby pond water along the concrete/rock interface and into the borehole. This means that the flow rate measured from Layer SR1 included two parts, the flow from the concrete/rock interface and the flow from the upper 0.25-m of borehole wall below the concrete collar. In FLAC model and CODE_BRIGHT model, the calculated flow rate for Layer SR1 only included the flow from the 0.25-m placement borehole wall. The flow from the concrete/rock interface was not considered in the numerical model.

Table 5: Measured and Simulated Water Inflow before Experiment Installation

Interval	Measured inflow m ³ /s	Calculated results using FLAC (Chandler et al. 1992)		Calculated results using CODE_BRIGHT	
		Inflow rate m ³ /s	Inflow ratio- Measured inflow/ Calculated inflow	Inflow rate m ³ /s	Inflow ratio- Measured inflow/ Calculated inflow
SR1	4.98x10 ⁻⁹	0.6x10 ⁻¹¹	830	0.37x10 ⁻¹¹	1360
SR2	8.05x10 ⁻¹¹	4.7x10 ⁻¹¹	1.7	4.00x10 ⁻¹¹	2.0
SR3	5.18x10 ⁻¹¹	8.7x10 ⁻¹¹	0.6	5.04x10 ⁻¹¹	1.0
SR4	3.48x10 ⁻¹¹	12.1x10 ⁻¹¹	0.3	5.82x10 ⁻¹¹	0.6
ST5	7.00x10 ⁻¹¹	16.6x10 ⁻¹¹	0.4	6.53x10 ⁻¹¹	1.1

3.4.2.2 Hydraulic Response in the Buffer

Figure 74 shows the measured pore water potential (suction) in the buffer at three times during heating. The negative pore water potential (suction) in the buffer near the heater became greater with time. This is because the thermally induced moisture movement from the buffer near the heater to the buffer farther from the heater (i.e., down the temperature gradient) resulted in decreasing water potential (increasing suction in the warmest regions). This phenomenon can be seen in the buffer below the heater and beside the heater. This phenomenon was not recorded in the buffer above the heater because there were no working sensors above the heater to record the change of the moisture. There were no sensors close to the rock.

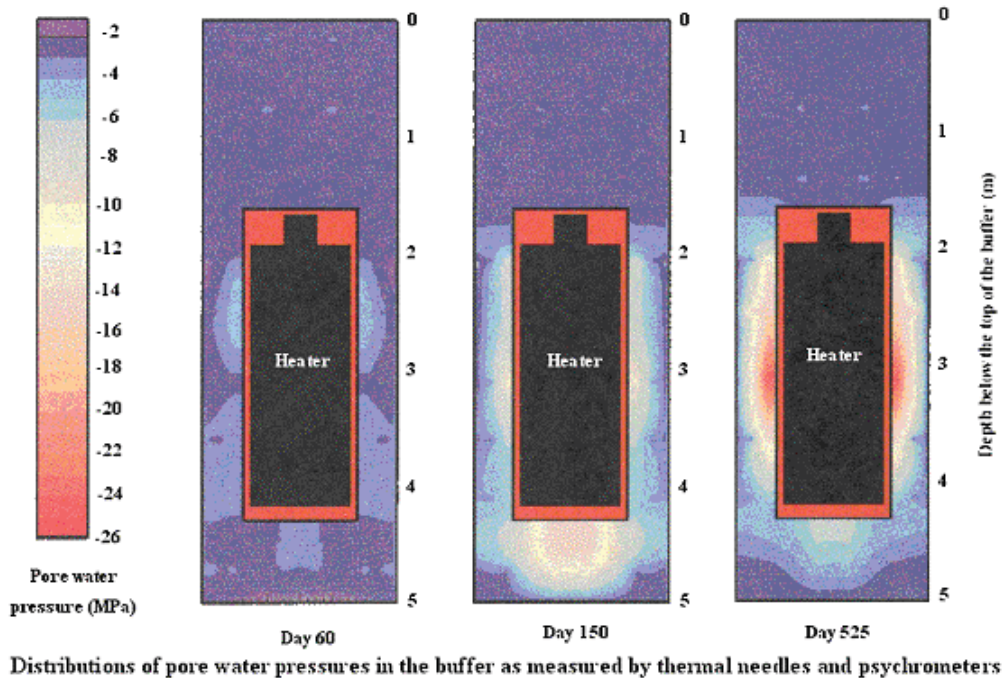


Figure 74: Pore Water Potential in the Buffer Measured by Thermal Needles and Psychrometers (after Graham et al. 1997) (Note: There were no functioning sensors in the buffer and backfill above the heater)

Figure 75 shows measurements of water content at the end of the experiment for the vertical section through the axis of the heater along the axis of Room 213. Compared with Figure 74, it should be noted that the buffer near and above the heater was drier as observed in the buffer below the heater and beside the heater. Also it can be noted that the buffer was saturated near the rock.

The simulated pore water potential in the buffer at three different times during heating is shown in Figure 76. The negative pore water potential (suction) of the buffer near the heater became greater when it was heated, including in the buffer above the heater (where no measured data was obtained during the experiment). Comparing Figure 76 with Figure 75, the phenomenon that the buffer near the borehole surface at the mid-height of the heater was saturated significantly caused by the greater pore water pressure in the rock induced by heating was replicated in this modelling.

Comparisons of simulated and measured suctions in the buffer for IBX01, IBX06, IBX07, IBX12, IBX16 and IBX17 are shown in Figures 77 and 78. The simulated suctions at locations IBX01, IBX06, IBX16 and IBX17 matched the measurements reasonably well. However, the simulated suction at Locations IBX07 and IBX12 did not match the measured data very well. One possible reason may be that they were near the interface of the buffer/rock. The difference may be caused by the data management in GiD at locations like the interface of two kinds of materials.

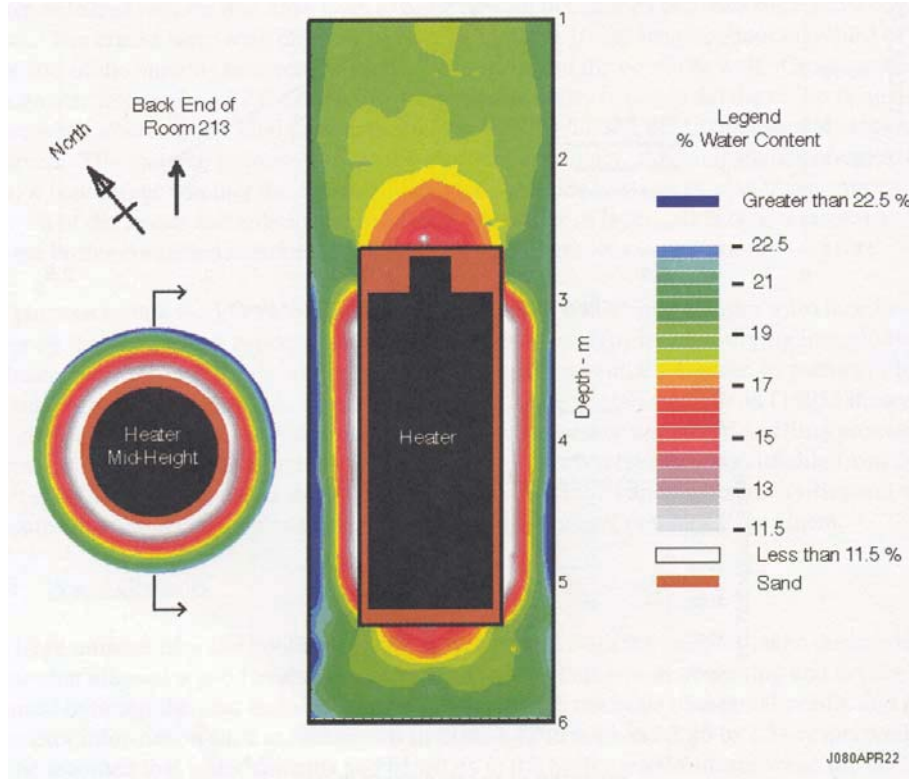


Figure 75: Vertical Section of Water Contents Measured during Decommissioning Aligned with Axis of Room 213 (Graham et al. 1997)

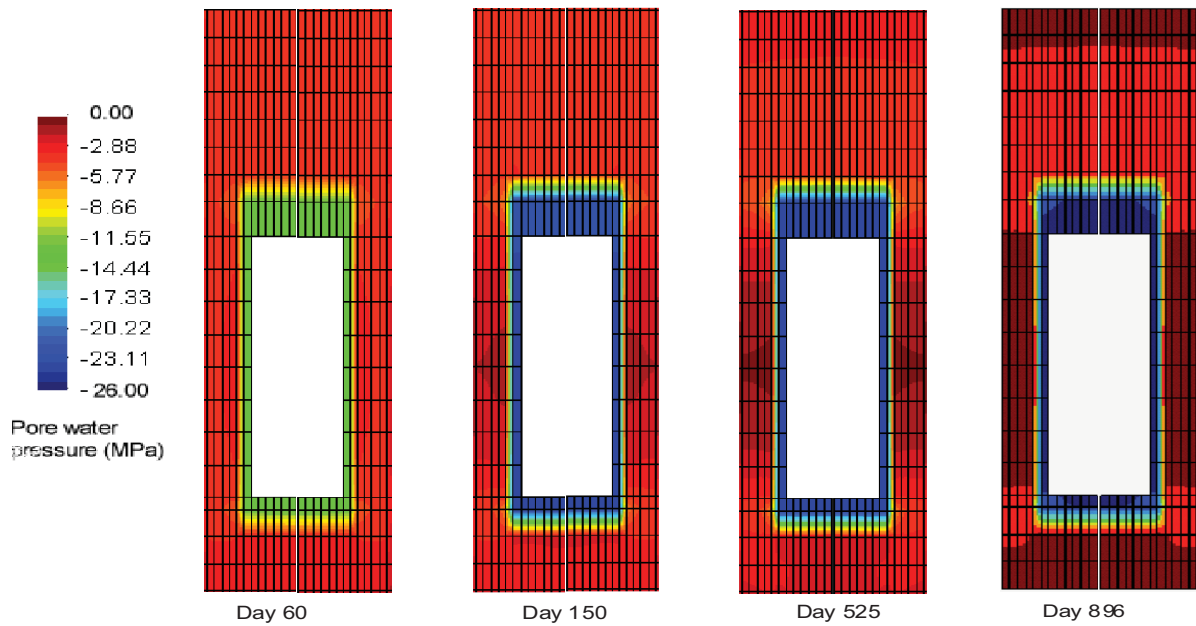


Figure 76: Simulated Transient Pore Water Pressures during Heating in the Buffer

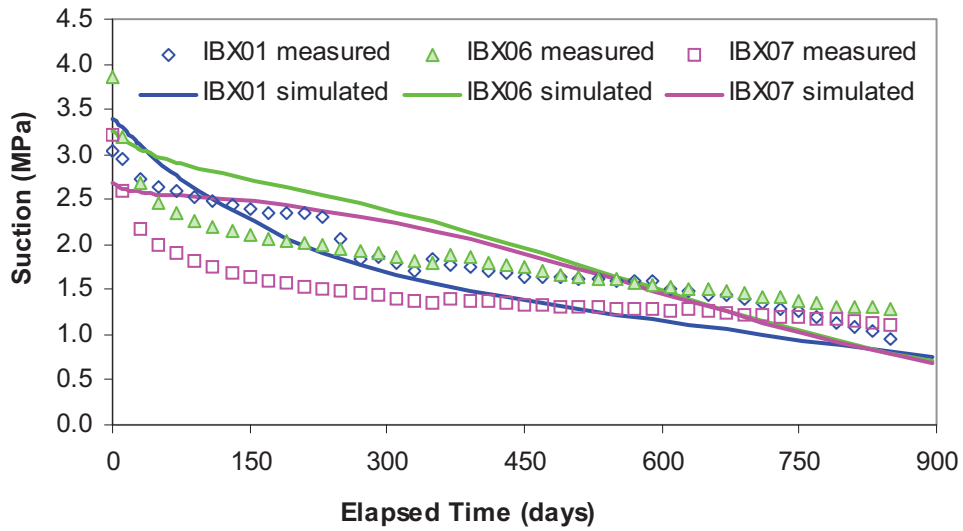


Figure 77: Comparisons of Simulated and Measured Suctions in the Buffer for IBX01, IBX06 and IBX07

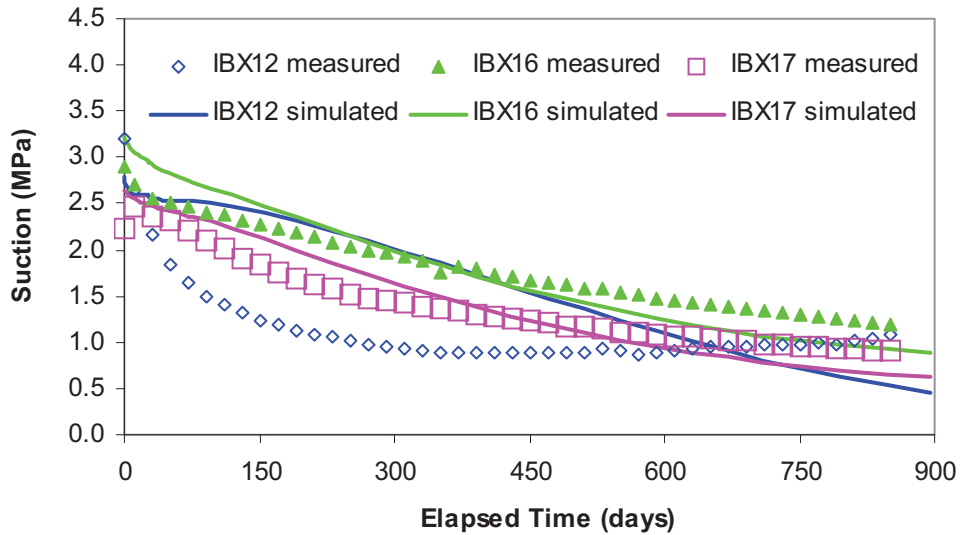


Figure 78: Comparisons of Simulated and Measured Suctions in the Buffer for IBX12, IBX16 and IBX17

3.4.2.3 Hydraulic Response in the Rock

Figure 79 shows contours of the measured pore water pressure in the domain of 4 m x 8 m in the rock around the heater borehole at four different times as measured between packers installed in boreholes HG7, HG8 and HG9 (refer to Figures 52 and 54 for locations). The pore

water pressure in the rock at locations of the third cells of HG8 and HG9 gradually increased as temperature increased to form a high pore water pressure area. With time, the high pore water pressure dissipated.

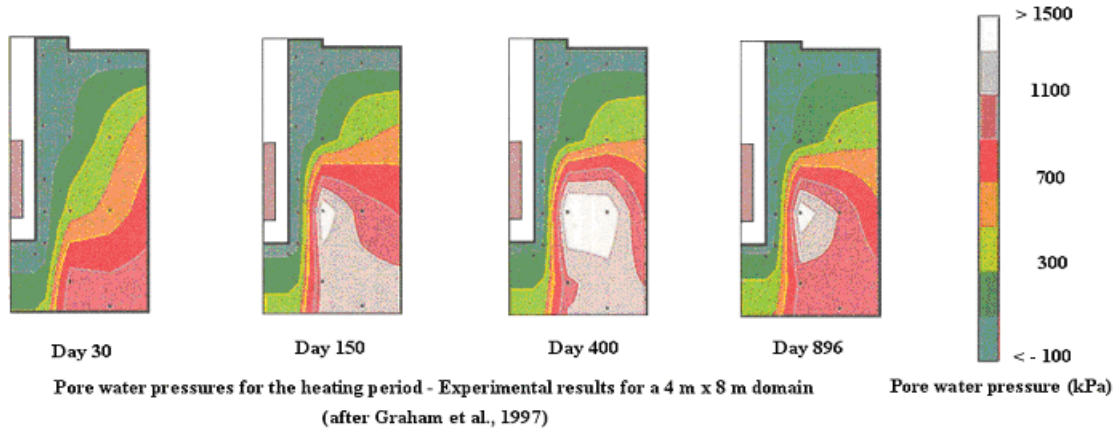


Figure 79: Measured Pore Water Pressures in a Domain of 4 m x 8 m in the Rock at Four Different Times

Figure 80 shows contours of the simulated pore water pressure in the rock at four different times using $5 \times 10^{-20} \text{ m}^2$ as the saturated permeability of the rock, which was the measured saturated permeability of the rock from the transient hydraulic pressure pulse method at the condition of ambient temperature (Chandler et al. 1998). Compared with Figure 79, the simulated results did not capture the characteristic that the thermally induced pore water pressure increased with temperature when using $5 \times 10^{-20} \text{ m}^2$ as the saturated permeability of the rock.

Figure 81 shows the simulated pore water pressure in the rock at four different times using $5 \times 10^{-22} \text{ m}^2$ as the hydraulic permeability of the rock. Comparing Figure 81 to Figure 79, the modelling results using a lower permeability captured the characteristic that the pore water pressure at location of the third cells of HG8 and HG9 increased and thereafter dissipated. On Day 30, the pore water pressure at the location of the second and third cells of HG8 increased to about 1.4 MPa. On Day 150, the position of the region of the highest pore water pressure moved to the location of the fourth cell of HG7 and the somewhere beneath the bottom of the borehole. The highest simulated pore water pressure at 150 days was 1.87 MPa. With time, the magnitudes of the pore water pressure increase dissipated (see Figure 81 on Day 400 and Day 896).

Figure 82 shows the comparison of the simulated and measured pore water pressures at locations in boreholes HG9, HG11, HG8, HG10 and HG7 at a depth of 2.45 m. Figure 83 provides a similar comparison for boreholes at locations HG9, HG11, HG8 and HG7 at a depth of 4.6 m from the floor of Room 213. A saturated permeability of the rock of $5 \times 10^{-22} \text{ m}^2$ was used to determine the simulated pore water pressure in both figures. At a depth of 2.45 m, the simulated pore water pressure for boreholes HG11, HG8, HG10 and HG7 had the same trends as those of the measured data. However, the measured pore pressures at these locations, which had the simulated peak pore pressures, were less than the simulated pore pressures

except for borehole HG11. The simulated pore water pressure dissipated faster than the measured data for all locations.

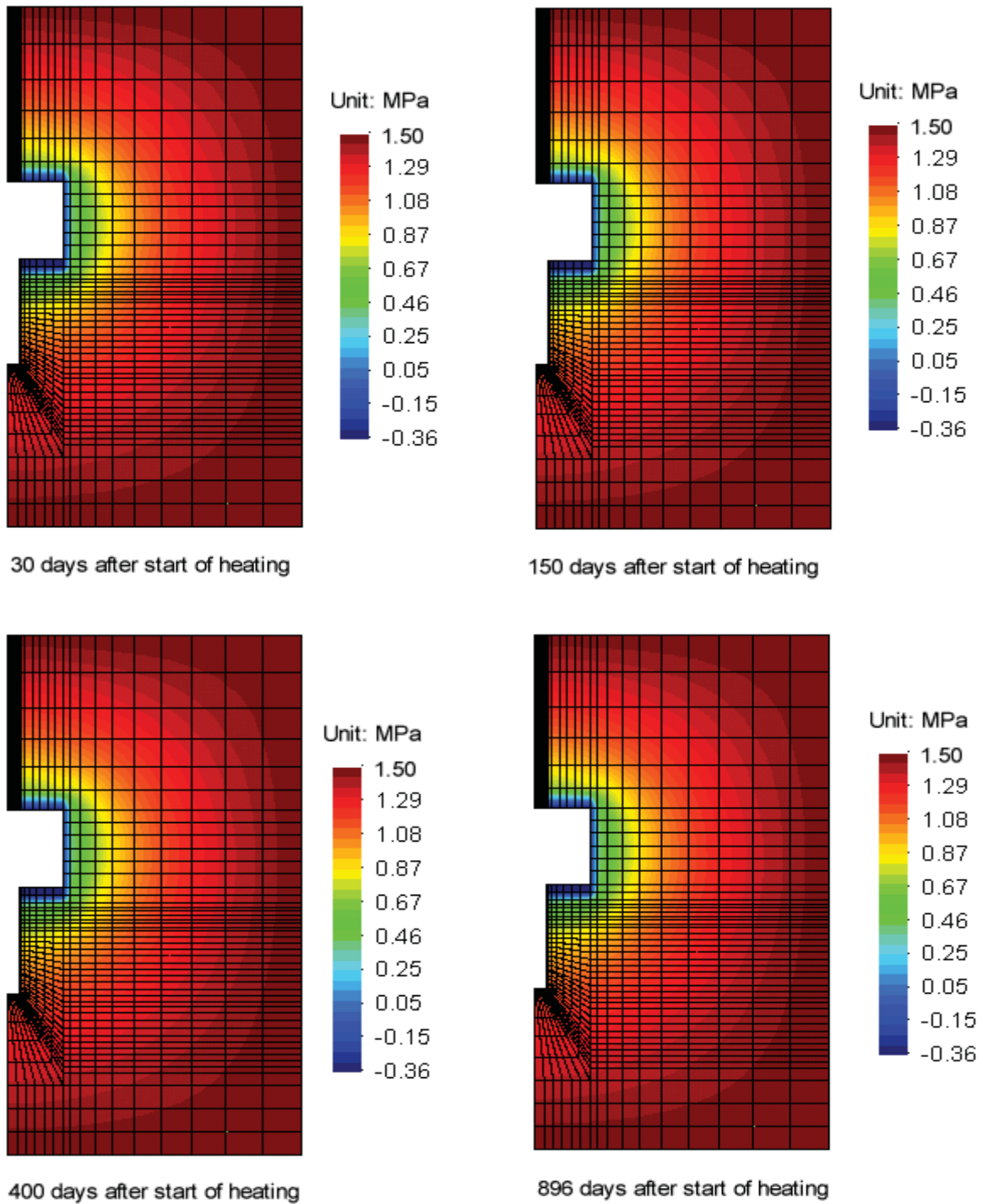


Figure 80: Simulated Pore Water Pressures during Heating at Four Different Times using $5 \times 10^{-20} \text{ m}^2$ as the Saturated Permeability of the Rock

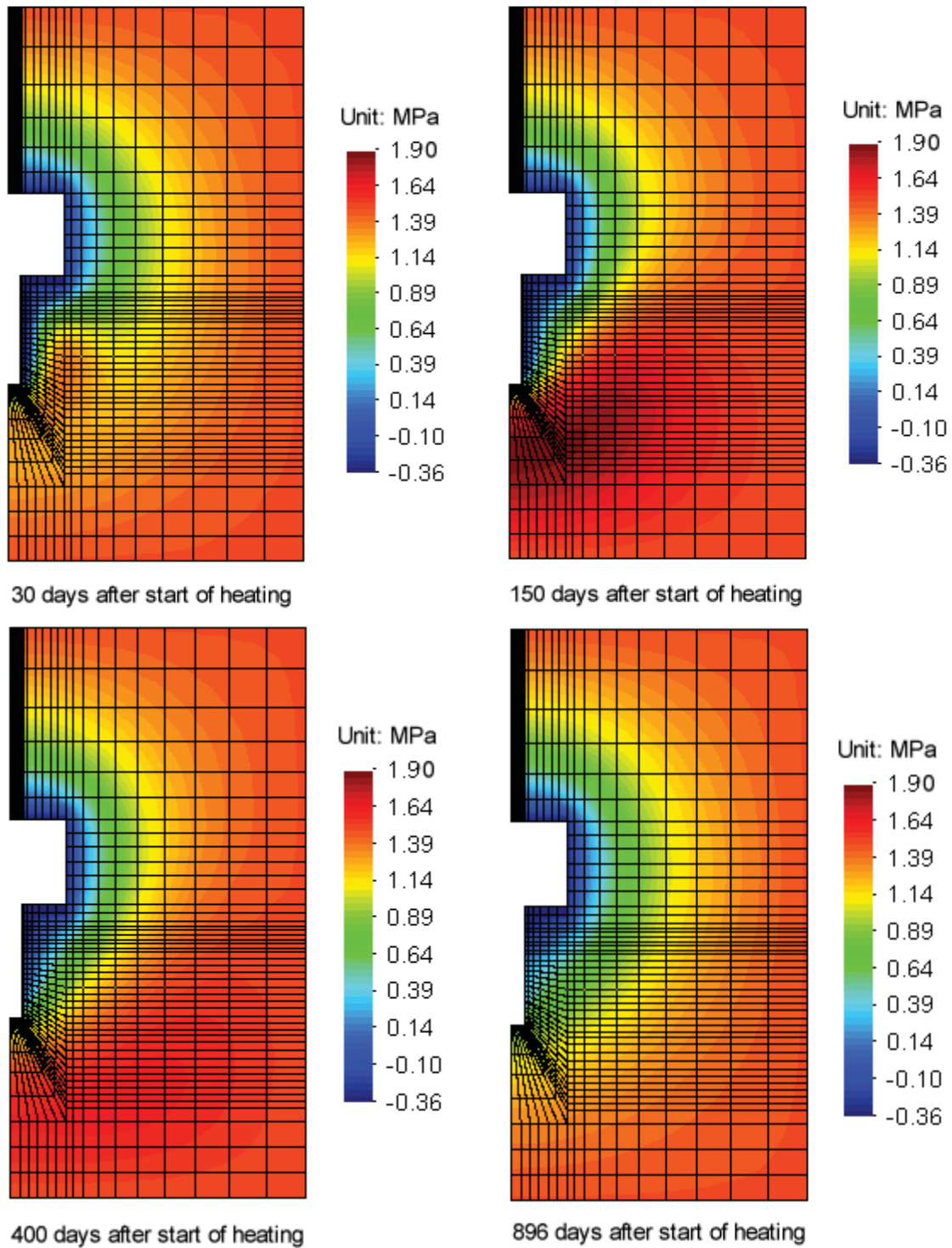


Figure 81: Simulated Pore Water Pressures during Heating at Four Different Times using $5 \times 10^{-22} \text{ m}^2$ as the Saturated Permeability of the Rock

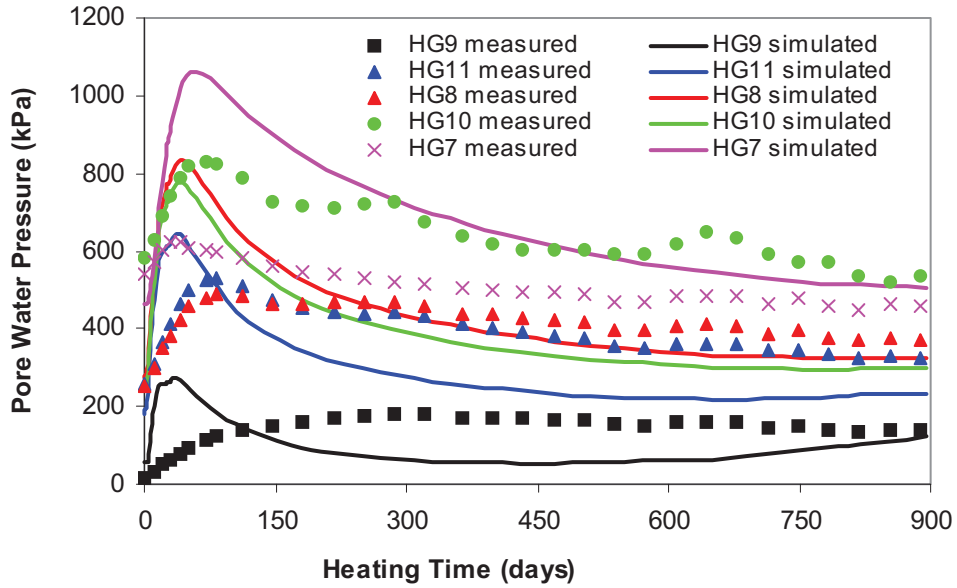


Figure 82: Simulated and Measured Pore Water Pressures at Locations HG9, HG11, HG8, HG10 and HG7 at a Depth of 2.45 m from the Floor of Room 213

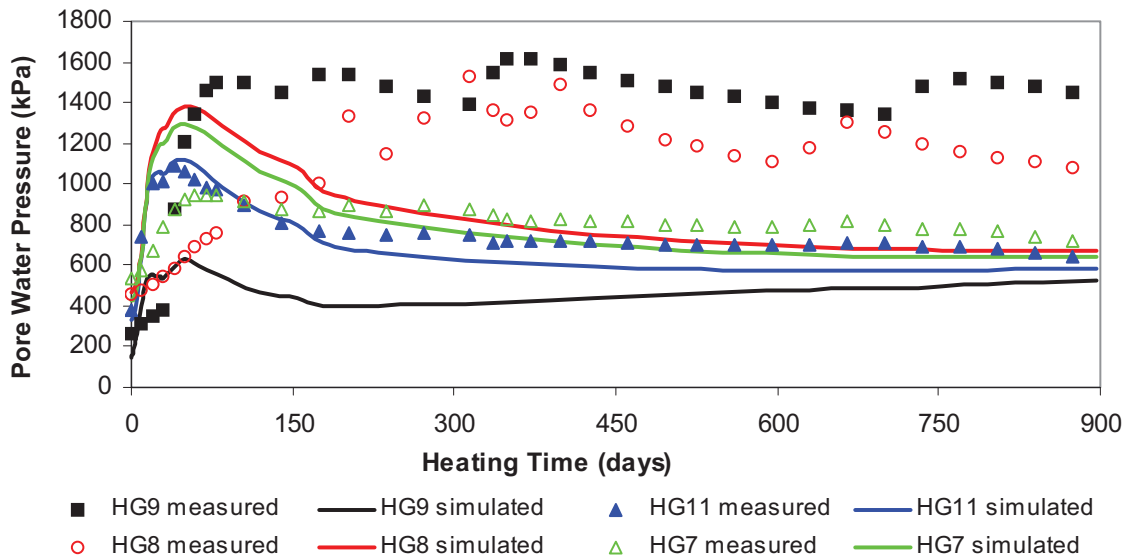


Figure 83: Simulated and Measured Pore Water Pressures at Locations HG9, HG11, HG8 and HG7 at a Depth of 4.6 m from the Floor of Room 213

At a depth of 4.6 m below the floor of Room 213, the highest measured pore water pressure was similar to the highest pore water pressure obtained from numerical modelling. However, the location of the simulated highest pore water pressure in the rock was further from the heater than the location of the highest pore water pressure of the measured results. The rate

of dissipation of the simulated pore water pressure was also higher than that of the measured data.

Figure 84 compares the simulated and measured pore water pressure in the rock at a depth of 1.0 m below the floor of Room 213 using $5 \times 10^{-22} \text{ m}^2$ as the saturated permeability of the rock. The pore water pressure in this packer interval was drained by the concrete rock interface and the measured data were almost zero. The simulated pore water pressure matched the measured data well for location HG9, HG11 and HG8. For location HG7, the simulated pore water pressure was higher than the measured data. The reason is related to the axisymmetry of the model. Borehole HG7 was located 3.5 m away from the borehole centreline along the axis of the tunnel, whereas the modelled room was only 3 m in radius. Thus, HG7 was placed entirely within the solid rock. The numerical pore pressure at a depth of 1 m, therefore, was less affected by the boundary conditions in Room 213 than the other boreholes.

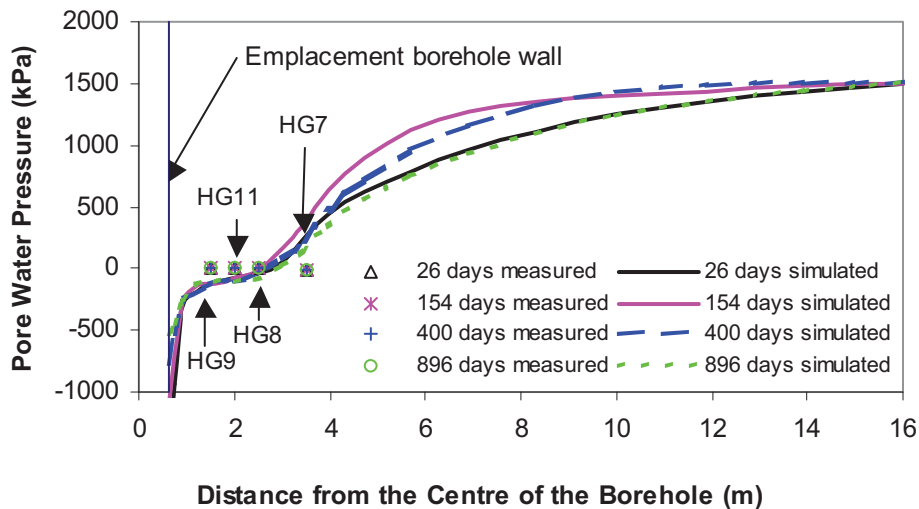


Figure 84: Simulated and Measured Pore Water Pressure Profiles in the Rock at a Depth of 1.0 m from the Floor of Room 213 (Note: the measured pore water pressure in these intervals remained constant and unchanged through the 896 day duration)

Figure 85 compares the simulated and measured pore water pressure in the rock at a depth of 2.45 m below the floor of Room 213 during heating using $5 \times 10^{-22} \text{ m}^2$ as the saturated permeability of the rock. The simulated pore water pressures matched the measured data reasonably well except on Day 26. On Day 26, although the measured pore water pressure at HG11 tended to be high, it was not as high as the simulated data.

Figure 86 shows the simulated pore water pressure in the rock at a depth of 4.6 m below the floor of Room 213 using $5 \times 10^{-22} \text{ m}^2$ as the saturated permeability of the rock and the measured pore water pressures at that depth in boreholes HG7, HG8, HG9 and HG11. At HG9, the simulated pore water pressure on Day 26 was much higher than the measured data.

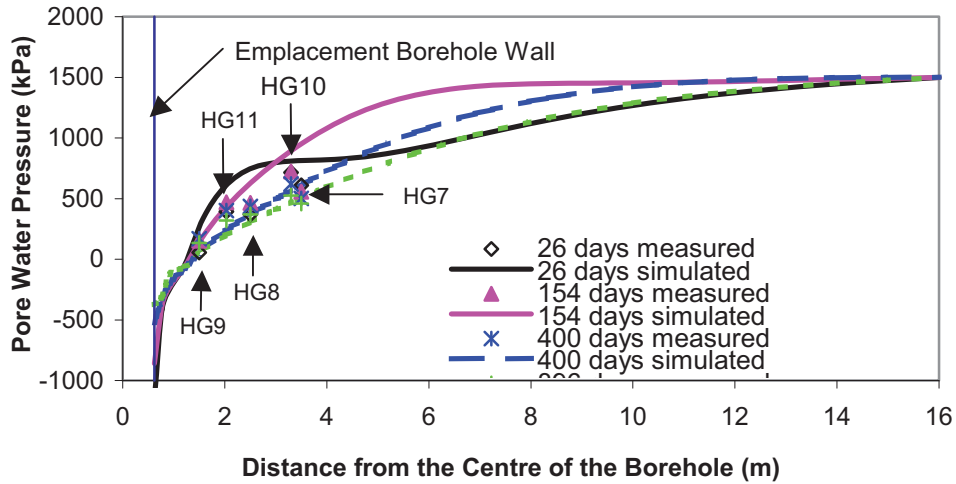


Figure 85: Simulated and Measured Pore Water Pressure Profiles in the Rock at a Depth of 2.45 m from the Floor of Room 213

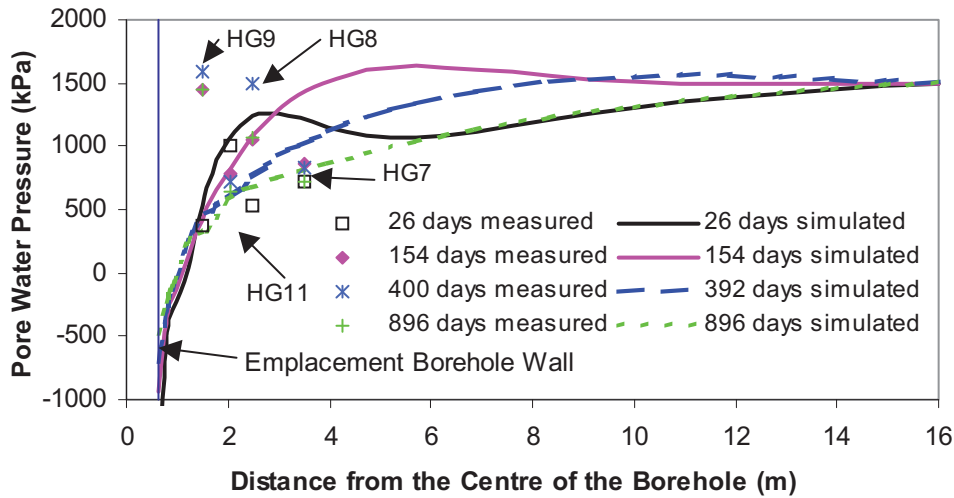


Figure 86: Simulated and Measured Pore Water Pressure Profiles in the Rock at the Depth of 4.6 m from the Floor of Room 213

From Figure 83, at a depth of 4.6 m, the highest simulated pore water pressure in HG9 was 620 kPa on Day 50. Subsequently, the pore water pressure started to decrease. However, the measured data shows a maximum of 1500 kPa that remained until the end of the test. From Figure 86, the distribution of the pore water pressure along a horizontal line shows that the pore water pressure, as measured by the packers, was highest near the borehole, and lower at more distant locations (e.g., borehole HG7). Presumably, the actual pore water pressures would gradually increase to the surrounding pore water pressure in the rock. The curve on Day 26 in Figure 86, more or less, captured these main characteristics. However, the value and location

of the highest pore water pressure from the simulation were different from the measured data. The position of the highest pore water pressure from simulation moved from the location near the borehole to a location further away from the borehole.

Figure 87 shows the pore water pressures measured using hydraulic piezometers at locations 1RH1 –1RH4 (refer to Figure 51 for locations). The hydraulic piezometers 1RH1, 1RH2 and 1RH3 did not show much changes during the whole heating period. Their values kept constant at –25 kPa. The hydraulic piezometer 1RH4 showed significant development of pore water pressure. The greatest change of the pore water pressure for 1RH4 was about 230 kPa.

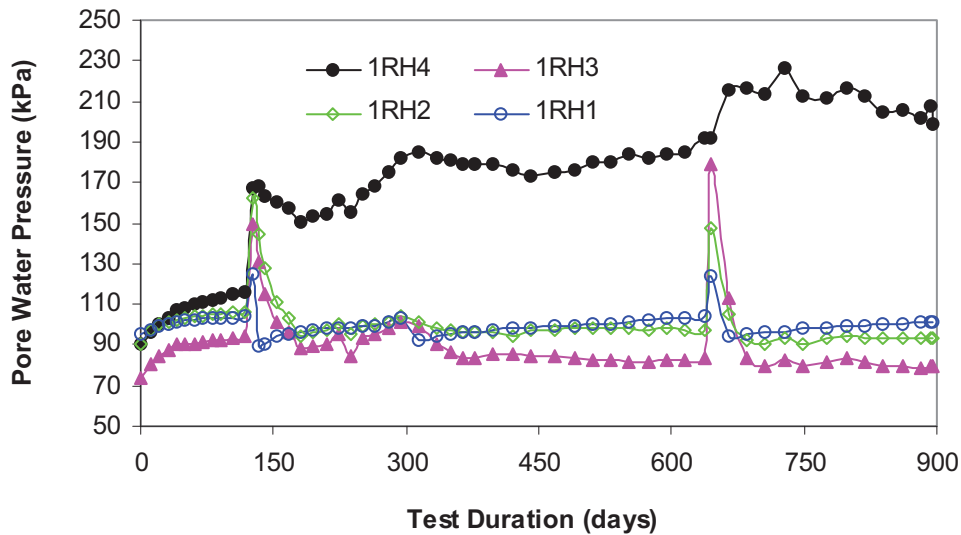


Figure 87: Water Pressures Measured in Hydraulic Piezometers 1RH1 – 1RH4 Close to Wall of Placement Borehole

Figure 88 shows the pore water pressure simulated at locations of hydraulic piezometers 1RH1 – 1RH4 close to the wall of the placement borehole. Figure 88 shows similar trends as that seen in Figure 87. However, the initial value of the simulated pore water pressure was lower than the initial value of the measured data. Although simulated pore water pressures at locations 1RH1, 1RH2 and 1RH3 had some changes, they were very small compared to 1RH4. The greatest change of simulated pore water pressure for 1RH4 was 210 kPa, similar to the measured result.

Considering the good match for Layers SR2, SR3, SR4 and SR5 in comparison to simulated water inflow from the surrounding rock to the placement borehole using $5 \times 10^{-20} \text{ m}^2$ as the permeability of the rock, $5 \times 10^{-20} \text{ m}^2$ is a suitable value for the rock permeability under ambient temperature. The coupling between pore water pressure and temperature change is affected by permeability, Biot coefficient, porosity, water thermal expansivity, solid grain expansivity, and water and solid compressibility. The permeability, in turn, is affected by temperature change. The possible reason a rock permeability of $5 \times 10^{-20} \text{ m}^2$ provides a good match is that the increase of the temperature changed the permeability of the rock. It would be useful to

continue to calibrate the CODE_BRIGHT model to in situ experiments to investigate the factors influencing the thermally induced pore water pressure change.

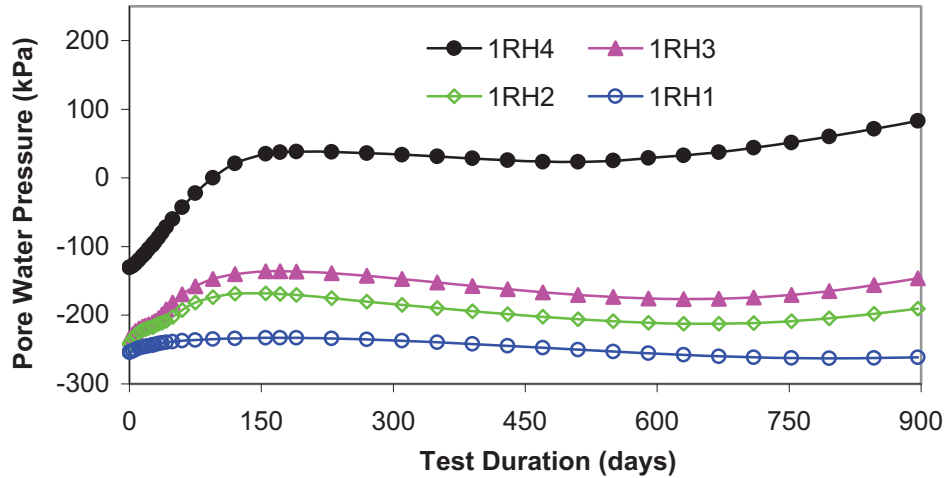


Figure 88: Water Pressures Simulated in Locations of Hydraulic Piezometers 1RH1 – 1RH4 Close to Wall of Placement Borehole

3.4.3 Mechanical Response in the Buffer and the Rock

3.4.3.1 Mechanical Response in the Buffer

Earth Pressures in the Buffer

Simulated vertical stresses in the buffer at locations 1BR1, 1BR3, 1BR4, 1BR5 and 1BG13 are compared with the measurements as shown in Figure 89. The simulated vertical stresses at locations 1BR1 and 1BR4 matched the measured data very well. The simulated vertical stresses at locations 1BR3 and 1BG13 have the same patterns as those of the measured results. The magnitudes of the simulated vertical stresses at Locations of 1BR3 and 1BG13 are different from the measured results. These differences were caused by the initial readings of the Earth Pressure Cells. Although the magnitudes of the simulated vertical stresses at Location 1BR4 were different from measured results, their trends were the same.

Simulated horizontal stresses in the buffer at locations 1BG4, 1BG8, 1BG10 and 1BG12 matched the measured results reasonably well (Figure 90). The pattern of the simulated horizontal stress in the buffer at location 1BG2 was exactly same as that of the measured results (Figure 90). The difference in magnitude between the simulated and the measured horizontal stresses at location 1BG2 was caused by the initial readings of the earth pressure cell. The simulated horizontal stress at location 1BG6 for the first 200 days matched the measured results very well. After 450 days, the measured results were lower than the simulated results, but their patterns were the same.

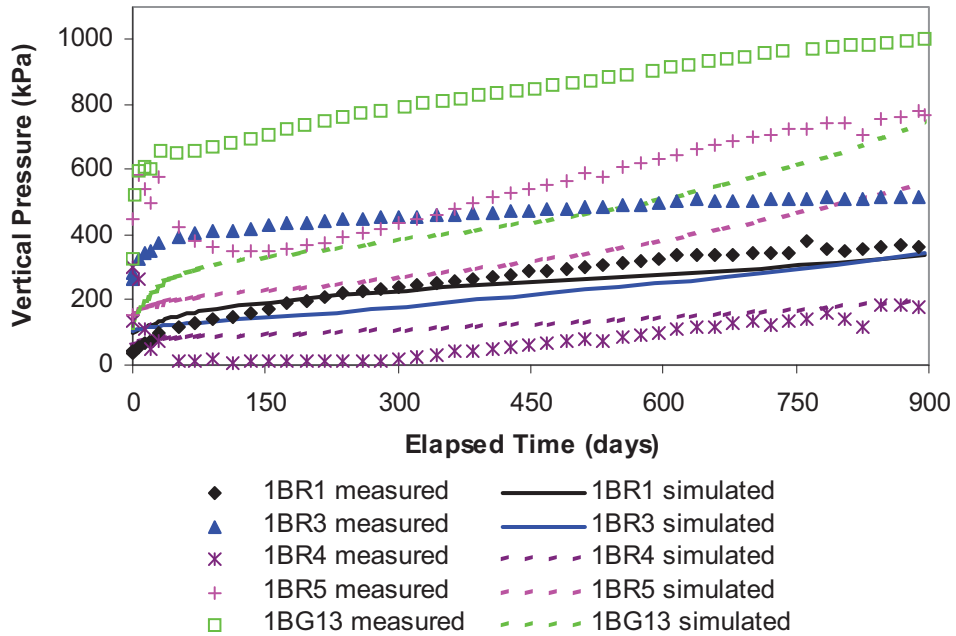


Figure 89: Vertical Stresses in the Buffer at Locations 1BR1, 1BR3, 1BR4, 1BR5 and 1BG13

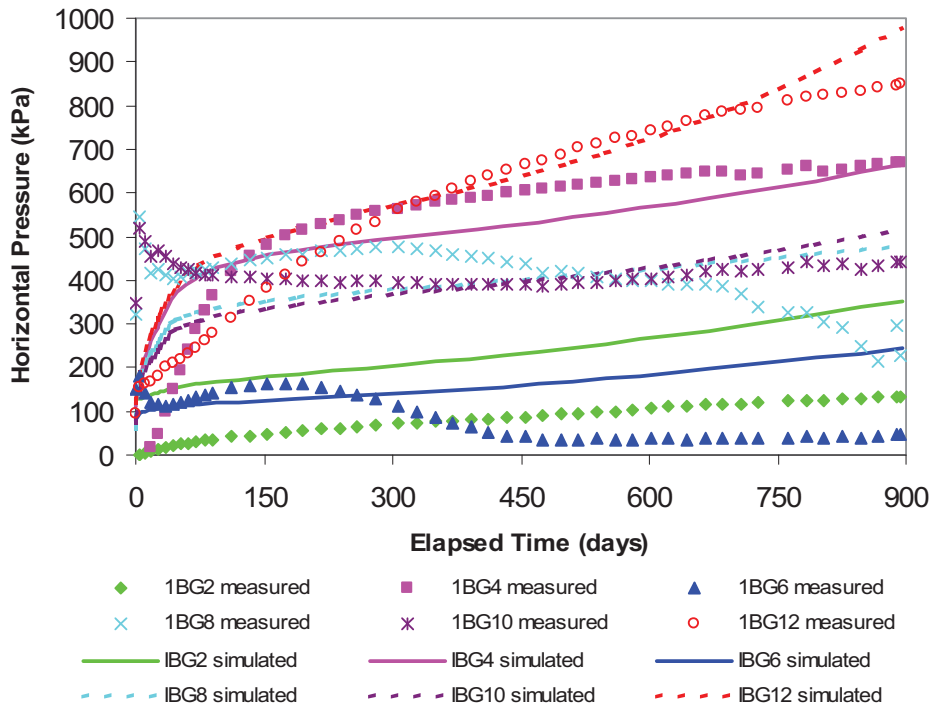


Figure 90: Horizontal Stresses in the Buffer at Locations 1BG2, 1BG4, 1BG6, 1BG8, 1BG10 and 1BG12

Simulated Displacements in the Buffer

In the buffer, there was no instrument to measure the displacements during the experiment. Therefore, only simulated displacements at different locations in the buffer are presented in this section.

Figure 91 shows the simulated vertical displacements along a vertical line through the axis of the heater. The buffer above the heater moved down because of the heating-induced shrinkage. The buffer below the heater expanded due to moisture content increase and moved up because of the restraint of the bottom of placement borehole. Local drying shrinkage was experienced just below the bottom of the heater.

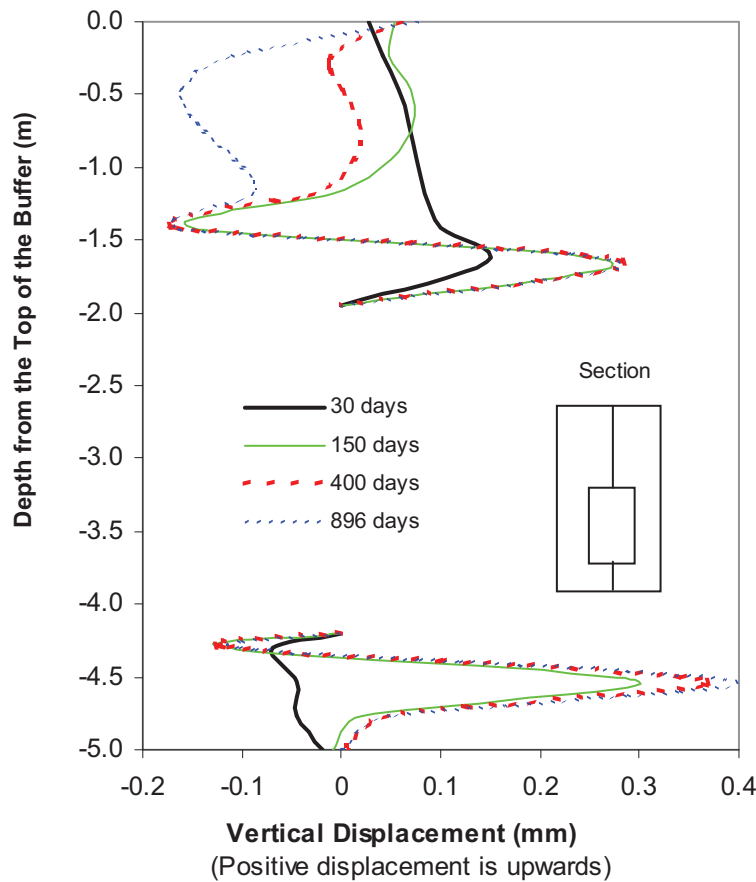


Figure 91: Simulated Vertical Displacements along a Vertical Line through the Axis of the Heater

Figure 92 shows the simulated horizontal displacements along a horizontal line through the mid-height of the heater. At start of heating, the moisture moved outwards. This induced the buffer expansion near borehole wall. After a certain time, when the thermal front in the rock caused the pore water pressure in the rock to increase, creating a high hydraulic gradient towards the

buffer, the buffer near the borehole wall became saturated. The saturation of the buffer near the wall of the borehole induced the buffer to expand towards the heater. Figure 93 shows the simulated vertical displacements along a horizontal line through the mid-height of the heater. The vertical displacements along the mid-height horizontal line were almost zero because of the symmetry of the experiment geometry.

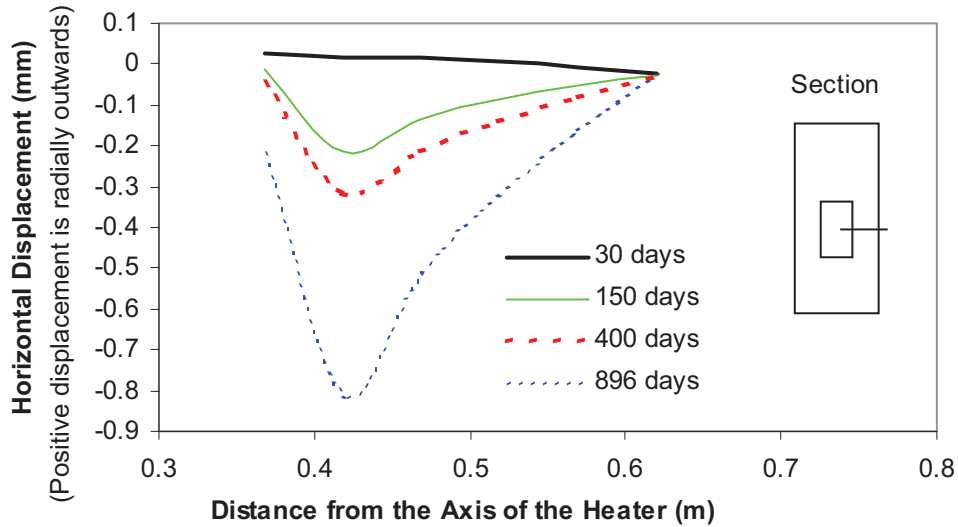


Figure 92: Simulated Horizontal Displacements along a Horizontal Line through the Mid-height of Heater

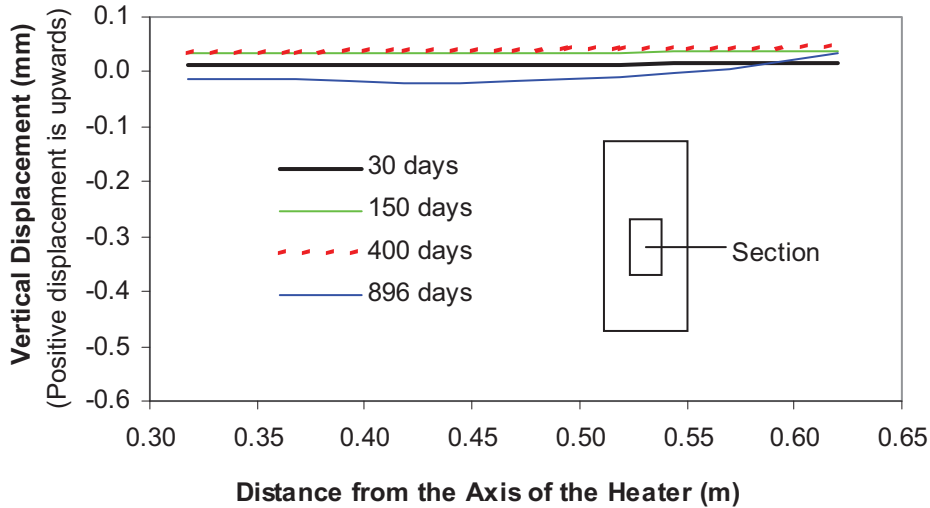


Figure 93: Simulated Vertical Displacements along a Horizontal Line through the Mid-height of the Heater

Figure 94 shows the simulated horizontal displacements along a vertical line 0.368 m from the axis of the heater. In the upper part of the buffer near the backfill and in the lowest part of the buffer near the bottom of the borehole, the buffer moved outwards due to the expansion of the buffer as moisture moved away from the buffer near the heater. The buffer adjacent to the heater moved towards the heater because of the combined effect of shrinkage in the buffer near the heater and the expansion of the buffer near the wall of the borehole.

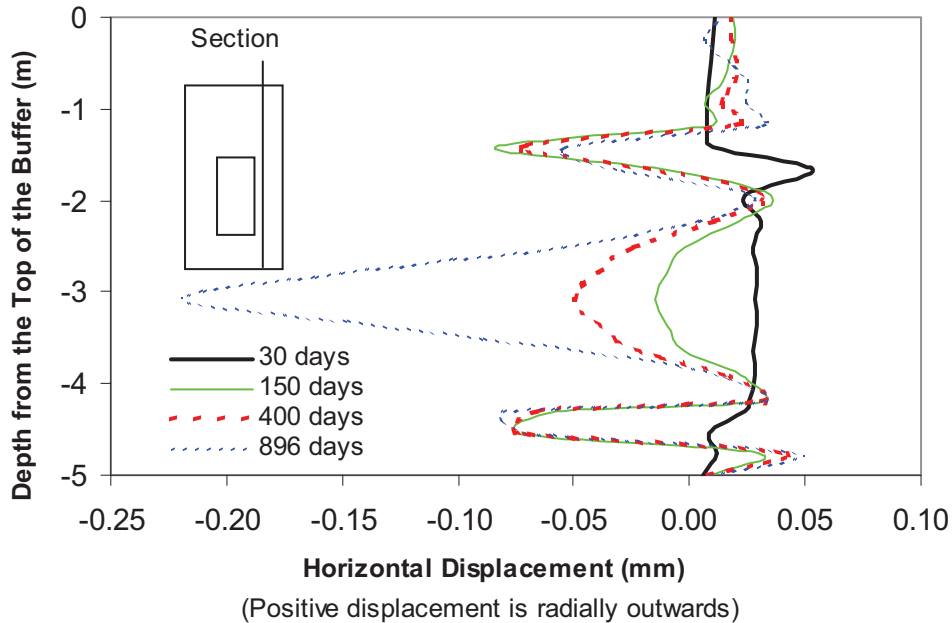


Figure 94: Simulated Horizontal Displacements along a Vertical Line 0.368 m from the Axis of the Heater

Figure 95 shows the simulated vertical displacements along a vertical line 0.368 m from the axis of the heater. On day 30, the buffer below the heater moved down because of the moisture movement-induced swelling. Later on, thermal expansion of the buffer caused the buffer near the heater to move down and the buffer near the bottom of the borehole to move up. At the mid-height of the heater and above, thermal expansion of the buffer resulted, generally, in an upward movement of the buffer.

Figure 96 shows the simulated horizontal displacements along a vertical line 0.57 m from the axis of the heater (0.05 m from the surface of the rock). The buffer moved inwards because of the restraint of the rock wall of the borehole. At a depth near the lower part of the heater, the buffer inward displacement was greatest, not only because of its thermal expansion, but also because of saturation-induced swelling of the material near the rock.

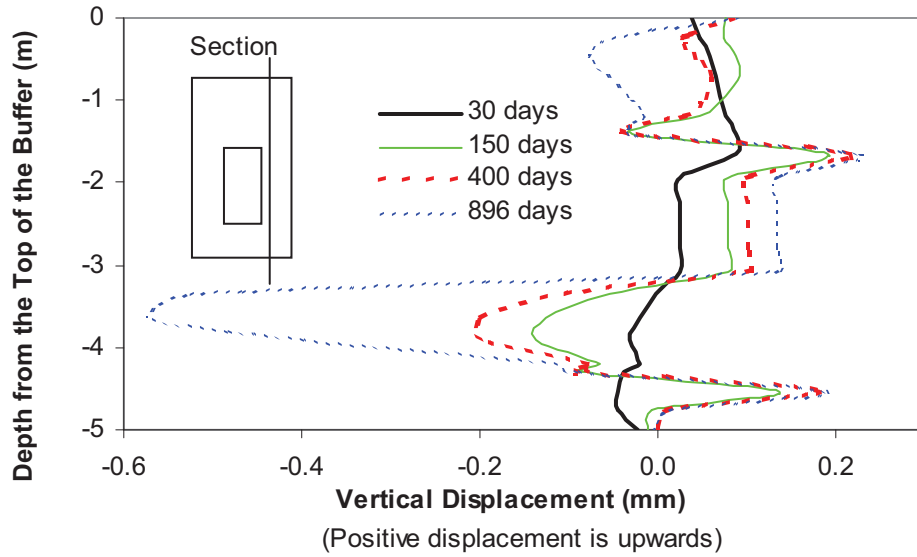


Figure 95: Simulated Vertical Displacements along a Vertical Line 0.368 m from the Axis of the Heater

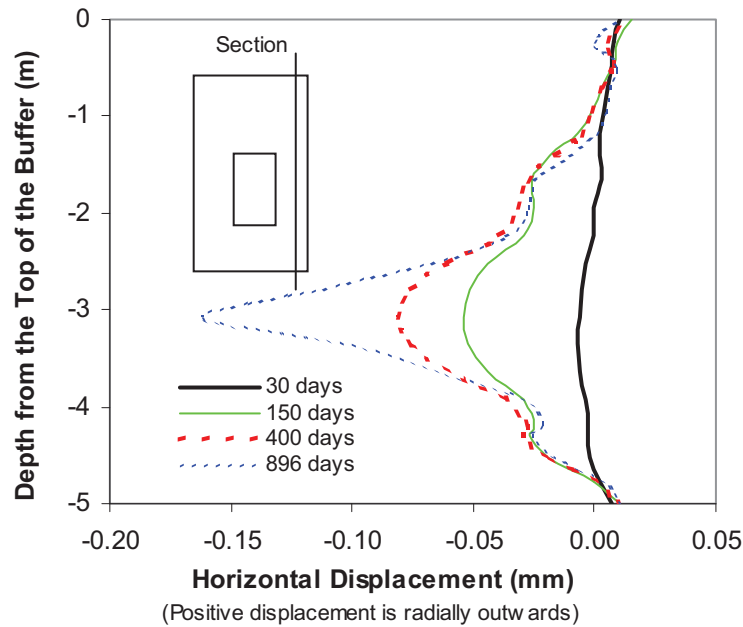


Figure 96: Simulated Horizontal Displacements along a Vertical Line 0.57 m from the Axis of the Heater

Figure 97 shows the simulated vertical displacements along a vertical line 0.57 m from the axis of the heater. The buffer below the mid-height of the heater moved down, while the buffer

above the mid-height of the heater moved upwards because of thermal expansion and experiment symmetry.

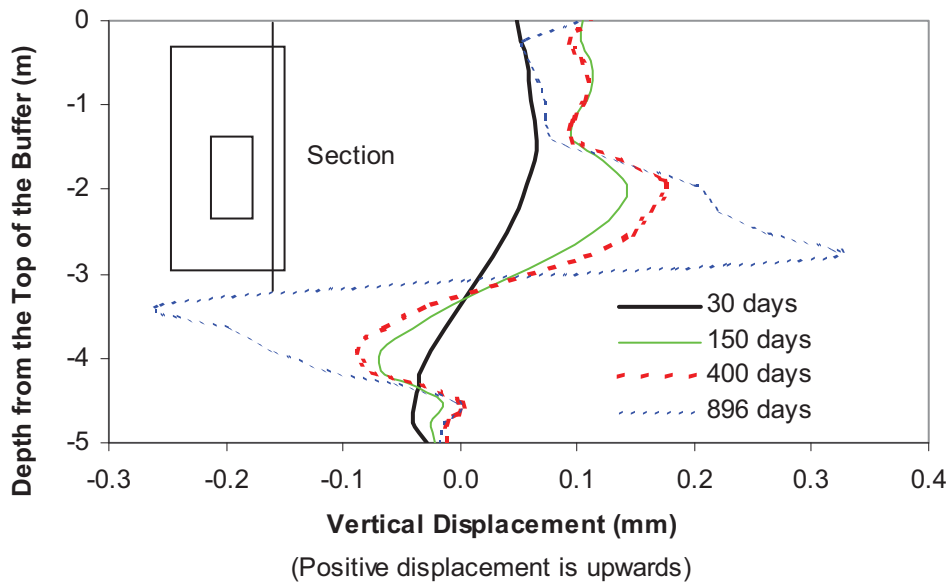


Figure 97: Simulated Vertical Displacements along a Vertical Line 0.57 m from the Axis of the Heater

3.4.3.2 Mechanical Response in the Rock

Simulated Stresses in the Rock

Figure 98 shows the simulated horizontal stress change in the rock induced by desaturation and heating. The greatest compressive horizontal stress change was about 3.2 MPa at the location near the mid-height of the heater.

Figure 99 shows the contours of the vertical stress change in the rock at four times during heating. The greatest compressive vertical stress change was 5.5 MPa at the same location as the greatest increase in temperature.

Comparison of the Simulated and Measured Displacements in the Rock

Using $3.8 \times 10^{-6} \text{ }^\circ\text{C}^{-1}$ (Graham et al. 1997) as the coefficient of linear thermal expansion for the rock, the simulated displacement was in the range of one or two orders of magnitude less than the measured data. Figure 100 shows the comparison between the simulated vertical displacements using $2 \times 10^{-5} \text{ }^\circ\text{C}^{-1}$ as an arbitrarily selected coefficient of linear thermal expansion for the rock and measured data in the rock on Day 110. Although there were some differences in value between the simulated and the measured data, their patterns were the same. This indicates some mechanical parameters of the rock used may need to be refined. If the value of $2 \times 10^{-5} \text{ }^\circ\text{C}^{-1}$ were the true value of the coefficient of linear thermal expansion of the

rock, the thermally induced horizontal stress change would be 16 MPa and the thermally induced vertical stress change would be 27.5 MPa.

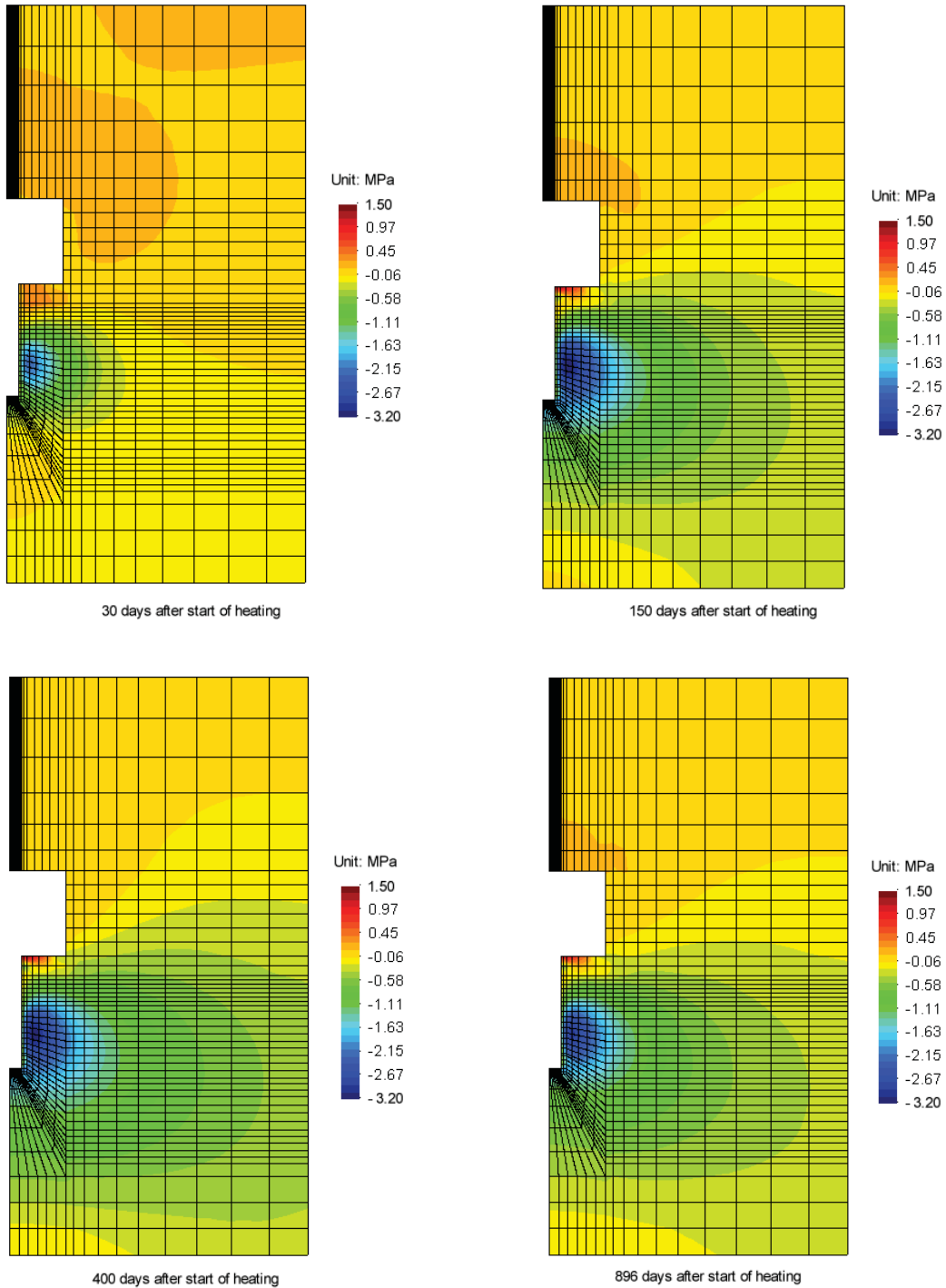


Figure 98: Simulated Horizontal Stress Change Contours in the Rock at Four Different Times (Positive stress indicates tension)

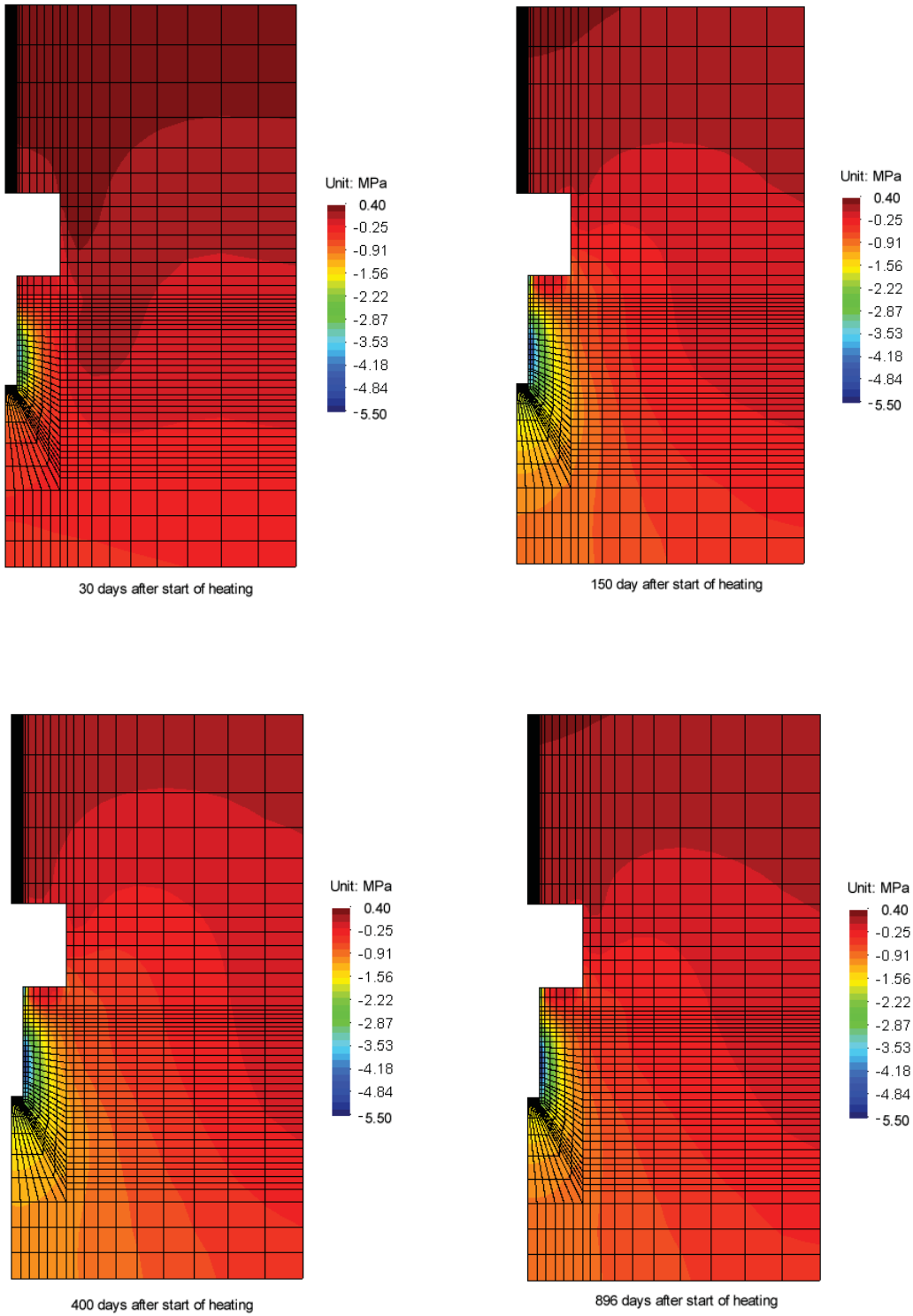


Figure 99: Simulated Vertical Stress Change Contours in the Rock at Four Different Times (Positive stress indicates tension)

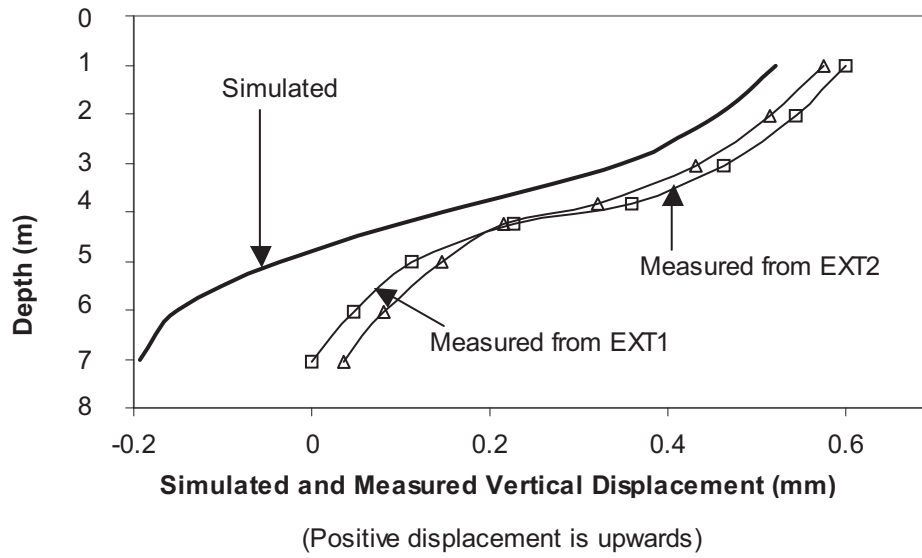


Figure 100: Comparisons of Simulated and Measured Vertical Displacements in the Rock

3.5 SUMMARY - BCE MODELLING

The modelled temperatures on the container skin using CODE_BRIGHT matched measured data very well. The temperatures modelled in the rock and the buffer using CODE_BRIGHT matched the measured data reasonably well at most locations, indicating that in these simulations the choice of the thermal parameters for all of the materials was reasonable and the thermal boundary conditions were suitable.

The pattern of the simulated suctions in different locations in the buffer matched that of the measured suction reasonably well. The thermally induced moisture movement in the buffer, modelled using CODE_BRIGHT, captured the main characteristics of the moisture movement, including the saturation of the buffer near the surface of the placement borehole at the mid-height of the heater.

Comparison of the simulated pore water pressure in the surrounding rock from the CODE_BRIGHT model with the measured data implies that the saturated permeability of the rock in the Buffer/Container Experiment ranged from $5 \times 10^{-20} \text{ m}^2$ for the ambient temperature rock to $5 \times 10^{-22} \text{ m}^2$ for elevated temperature rock. The results of the modelling imply that the permeability of the rock may be a function of temperature and stress. These characteristics should be studied further.

The simulated horizontal and vertical earth pressures in the buffer matched the measurements reasonably well for most locations. The differences between the simulated and measured earth pressures for some locations (for example, IBG13 and IBG2) were caused by the initial readings of earth pressure sensors. Comparison of the simulated rock displacements with measured data shows that the CODE_BRIGHT model successfully captured the main

characteristics of the mechanical response to the heating. However, the parameters used in this modelling may still need to be refined.

4. CONCLUSIONS

A series of simulations for the ITT and the Buffer/Container Experiment has been conducted using the finite element program CODE_BRIGHT. The numerical modelling was done to provide a comparison of the measured data with the simulated response in an attempt to obtain a better understanding of the thermal, hydraulic and mechanical evolution in the buffer and the surrounding rock and interactions between the unsaturated buffer and the host rock. The following conclusions are obtained:

Thermal Response:

- The temperatures modelled in the rock and the buffer in the Buffer/Container Experiment using CODE_BRIGHT matched the measured data reasonably well at most locations, indicating that in these simulations the choice of the thermal parameters for all of the materials was reasonable.

Hydraulic Response:

- A series of analyses for the stage prior to placement of the buffer in the ITT was carried out to understand the influence of boundary conditions and the excavation-induced damage zone on the hydraulic evolution of the rock. Back analyses of the pore water pressure in the rock indicate that there was desaturation in the rock around the borehole and Room 205.
- The total water uptake by the buffer in the ITT was modelled. The greatest difference between the predicted pore water pressure and the measured data at the end of the test was at the bottom most layer of the buffer. CODE_BRIGHT underestimated the moisture flow from the rock through the base of the borehole for both the case of an empty borehole and the borehole filled with buffer.
- The water seepage into the borehole could be calculated without considering the desaturation influence on the hydraulic conductivity of the rock when the rock surface was not sealed by sand-bentonite buffer. After buffer was placed into the borehole, the simulation should incorporate the desaturation influence on the hydraulic conductivity of the rock. The large difference between the measured and calculated inflow from the rock to the borehole for the top layer of the seepage collection system in the Buffer/Container Experiment may be caused by the flow of water along the concrete floor /rock interface.
- The simulation of thermally induced moisture movement in the buffer in the Buffer/Container Experiment captured the main characteristics of the moisture movement, including the saturation of the buffer near the surface of the placement borehole at the mid-height of the heater.
- Comparison of the simulated pore water pressure in the rock with the measured data implies that the saturated permeability of the rock in the Buffer/Container Experiment ranged from $5 \times 10^{-20} \text{ m}^2$ for the ambient temperature rock to $5 \times 10^{-22} \text{ m}^2$ for elevated temperature rock. The results of the modelling imply that the permeability of the rock

may be a function of temperature and stress. These characteristics should be studied further.

Mechanical Response:

- Comparison of the hydraulic pore pressure from hydraulic-only modelling to those from coupling mechanical and hydraulic components for the ITT showed negligible difference because the mechanical response had little effect on water uptake by the buffer or flow through the rock.
- The numerical simulation captured the characteristics of the main mechanical behaviour of the buffer. The prediction of expansion in the upper and lower portions of the buffer and compression in the central region in the ITT was consistent with the density distribution after it was decommissioned. The simulated earth pressures in the buffer of the Buffer/Container Experiment matched the measurements reasonably well. However, there were some differences between the simulated earth pressures and the measurements for the ITT.
- Comparison of the simulated rock displacements with measured data in the Buffer/Container Experiment shows that the CODE_BRIGHT model successfully captured the main characteristic of the mechanical response to the heating. However, the parameters used in this modelling may still need to be refined.

The results for the Buffer/Container Experiment and the ITT simulations improved the level of confidence in the use of CODE_BRIGHT to assess field behaviour of a heated system of unsaturated buffer and rock and to predict the evolution of an engineered barrier system.

ACKNOWLEDGEMENTS

The numerical simulation work is funded by Nuclear Waste Management Organization. The author would like to acknowledge AECL staff involved in the Buffer/Container Experiment and the Isothermal Test.

REFERENCES

- AECL. 1994. Environmental Impact Statement on the concept for disposal of Canada's nuclear fuel waste. Atomic Energy of Canada Limited Report, AECL-10711, COG-93-1.*
- Alonso E.E., A. Gens and A. Josa. 1990. A constitutive model for partially saturated soils. *Geotechnique* 40, No. 3, pp. 405-430.
- Blatz, J.A. and J. Graham. 2003. Elasto-plastic modelling of unsaturated soil using results from a new triaxial test with controlled suction. *Geotechnique* 53, No. 1, pp. 113-122.
- Chandler, N.A. 2000. Water inflow calculation for the Isothermal Buffer-Rock-Concrete Plug Interaction Test. Ontario Power Generation, Nuclear Waste Management Division Report No. 06819-REP-01200-10046-R00.
- Chandler, N.A., B.H. Kjartanson, E.T. Kozak, C.D. Martin and P.M. Thompson. 1992. Monitoring the geomechanical and hydrogeological response in granite for AECL Research's Buffer/Container Experiment. *In Proc. of 33rd U.S. Rock Mechanics Symposium*, pp. 161-170.
- Chandler, N.A., A.W.L. Wan and P.J. Roach. 1998. The Buffer/Container Experiment design and construction report. Atomic Energy of Canada Limited Report AECL-11792, COG-97-186-1.*
- Detournay, E. and I. Berchenko. 1994. Thermoporoelastic analysis of the URL heater tests: A preliminary study. Unpublished research report to AECL, October 1994.
- Dixon, D.A. and N.A. Chandler. 2000. Physical properties of materials recovered from the Isothermal Buffer-Rock-Concrete Plug Interaction Test conducted at the URL. Ontario Power Generation, Nuclear Waste Management Division Report No. 06819-REP-01300-10003-R00.
- Dixon, D.A., N.A. Chandler, S. Stroes-Gascoyne and E. Kozak. 2001. The Isothermal Buffer-Rock-Concrete Plug Interaction Test: final report. Ontario Power Generation, Nuclear Waste Management Division Report No. 06819-REP-01200-10056-R00.
- Ewen, J. and H.R. Thomas. 1989. Heating unsaturated medium sand. *Geotechnique*, 39(3), pp. 455-470.
- Gens, A., A.J. Garcia-Molina, S. Olivella, E.E. Alonso and F. Huertas. 1998. Analysis of a full scale in situ test simulating repository conditions. *International Journal for Numerical and Analytical Methods in Geomechanics*, Vol. 22, pp. 515-548.
- Graham, J., N.A. Chandler, D.A. Dixon, P.J. Roach, T. To and A.W.L. Wan. 1997. The Buffer/Container Experiment: Results, synthesis, issues. Atomic Energy of Canada Limited Report, AECL-11746, COG-97-46-1.*

- Green, R.E. and J.C. Corey. 1971. Calculation of hydraulic conductivity: a further evaluation of some predictive methods. In Proc. of the Soil Society of America, Vol. 35, pp. 3-8.
- Guo, R. and D. Dixon. 2005. Coupled hydromechanical modelling of AECL's Isothermal Test and comparison with measured data. Ontario Power Generation, Nuclear Waste Management Division Report No. 06819-REP-01200-10153-R00.
- Guo, R. 2006. Coupled thermohydromechanical modelling Of AECL's Buffer/Container Experiment and comparison with measured data. Ontario Power Generation, Nuclear Waste Management Division Report No. 06819-REP-01200-10161-R00.
- Kjartanson, B.H. and M.N. Gray. 1987. Buffer/Container Experiment in the Underground Research Laboratory. In Proc. of the 40th Canadian Geotechnical Society Conference, Regina, SK, October 1987.
- Lingnau, B.E., J. Graham and N. Tanaka. 1995. Isothermal modelling of sand-bentonite mixtures at elevated temperatures. Canadian Geotechnical Journal 32: 78-88.
- Maak, P. and G.R. Simmons. 2005. Deep geologic repository concepts for isolation of used fuel in Canada. In Proc. of Waste Management, Decommissioning, and Environmental Restoration for Canada's Nuclear Activities – Current Practices and Future Needs. Ottawa, Canada, May 8-11.
- NRCan (Natural Resources Canada). 2007. Canada's Nuclear Future: Clean, safe Responsible. Natural Resources Canada news release 2007/50, June 14, 2007. (Available at www.nrcan-rncan.gc.ca/media/newsrelease/2007/200750.e.htm).
- NWMO (Nuclear Waste Management Organization). 2005. Choosing a way forward. The future management of Canada's used nuclear fuel. Nuclear Waste Management Organization. (Available at www.nwmo.ca).
- Olivella, S., A. Gens, J. Carrera and E.E. Alonso. 1996. Numerical modelling for a simulator (CODE_BRIGHT) for the coupled analysis of saline media. In Engineering Computations, Vol. 13, No. 7, pp. 87-112.
- Olsen, H.W. 1960. Hydraulic flow through saturated clay. In Proceedings of the Ninth National Conference on Clays and Clay Minerals, Vol. 40, pp. 219-241.
- Onofrei, C., A.M. Crawford, N. Jayawardene and K.C. Lau. 1995. Modelling of the earth pressure response – URL Buffer/Container Experiment. International Workshop on Hydro-Thermo-Mechanics of Engineering Clay Barriers and Geological Barriers. McGill University, Montreal, PQ, July 1995.
- Radhakrishna, H.S., A.M. Crawford, B. Kjartanson and K.C. Lau. 1992. Numerical modelling of heat and moisture transport through bentonite-sand buffer. Canadian Geotechnical Journal 29: pp. 1044-1059.
- Thomas, H.R., P.J. Cleall and H.P. Mitchell. 2002. Comparison of physical measurements and a finite element numerical simulation of water uptake and distribution in the Isothermal Test. Ontario Power Generation, Nuclear Waste Management Division Report No. 06819-REP-01300-10042-R00.

Thomas, H.R., P.J. Cleall and H.P. Mitchell. 2003a. Coupled thermal-hydraulic-mechanical simulation of the Buffer/Container Experiment. Ontario Power Generation, Nuclear Waste Management Division, Technical Report 06819-REP-01200-10111-R00.

Wan, A.W.L. 1996. The use of thermocouple psychrometers to measure in situ suctions and water contents in compacted clays. Doctoral Thesis, Dept. Civil and Geological Engineering, University of Manitoba, Winnipeg, Manitoba, Canada.

Wan, A.W.L., M.N. Gray and J. Graham. 1995. On the relations of suction, moisture content, and soil structure in compacted clays. In Proc. of the 1st International Conference on Unsaturated Soils, Paris, France, June 6-8, 1995, 215-222.

* Available from SDDO, Atomic Energy of Canada Limited, Chalk River Laboratories, Chalk River, Ontario K0J 1J0.